Abstract

OH, SANG JEONG. Spectroscopic Investigation of Hf-Si Oxynitride Alloys and Low Temperature Cobalt Metal ALD. (Under the direction of Dr. Gregory N. Parsons.)

Hf-Si oxynitride alloys were deposited by a remote plasma-enhanced chemical vapor deposition (RPECVD) system using the combination of the process conditions for Si oxynitride and Hf silicate alloys. The N-KLL, O-KLL, and Hf-NVV intensities measured by on-line AES (Auger Electron Spectroscopy) spectra were used to calculate the composition of alloys. The composition of Hf-Si oxynitride alloys can be tuned by controlling the N_2 / (N_2 + N_2O) ratio, Hf source flow rate, and the amount of He dilution.

FTIR (Fourier Transform Infrared Spectroscopy) and XPS (X-ray Photoelectron Spectroscopy) measurements were performed off-line and the results were used to investigate changes in film internal structure with (i) composition, and (ii) post-deposition annealing temperature. As deposited alloys show single feature in FTIR spectra, and there is no evidence of metallic Hf-Si, Hf-N, Hf-Hf, or Si-Si bonding in XPS core-level spectra.

The $(HfO_2)_X(SiO_2)_{1-X}$ alloys and $(Si_3N_4)_x(SiO_2)_{0.5\cdot(1-x)}(HfO_2)_{0.5\cdot(1-x)}$ alloys with low Si_3N_4 concentration (x = 0.07 and 0.17) show changes in FTIR absorption spectra after anneal at 900 ~ 1100℃ 60s, in Ar. However, $(Si_3N_4)_x(SiO_2)_{0.5\cdot(1-x)}(HfO_2)_{0.5\cdot(1-x)}$ alloys with high Si_3N_4 concentration (x = 0.33 and 0.49) show no change in FTIR spectra even after 1100℃ anneal. The results of XPS O1s spectra of the pseudo-binary $(HfO_2)_X(SiO_2)_{1-X}$ alloys and the pseudo-ternary $(Si_3N_4)_x(SiO_2)_{0.5\cdot(1-x)}(HfO_2)_{0.5\cdot(1-x)}$ alloys correspond to the results of FTIR spectra.

The chemical phase separation in Hf-Si oxynitride alloys was suppressed when the amount of Si_3N_4 phase is above 33%.

Micro/nanotubes with precisely defined nanoscale walls have attracted considerable attention with a variety of different processes and materials. Since ALD provides excellent step coverage on aggressive topographic structures, ALD has expanded rapidly its application fields. In some cases, ALD can be conducted at the generally lower temperature (~100℃ or less). This makes ALD attractive for coating on temperature-sensitive materials. We explored the low temperature metal ALD process for the fabrication of nanostructures.

In this work, Cobalt thin film deposition using atomic layer deposition process sequencing was studied between 30 and 130°C using $Co_2(CO)_8$ and H_2 gases using on-line quadrupole mass spectrometry and Auger electron spectroscopy. Similar experiments using cobalt cyclopentadienyl dicarbonyl and H_2 reactants were also performed between 140 and 350°C. For the dicobalt octacarbonyl precursor, mass spectroscopy and growth rate analysis showed precursor dissociation with non-self-limiting adsorption leading to continuous film growth at temperatures as low as 60°C, whereas the cyclopentadienyl dicarbonyl precursor showed evidence for CO cleavage and volatile Co(cyclopentadienyl) resulting in no film growth until ~300°C. The continuous film growth with the $Co_2(CO)_8$ is related to the zero-valent metal center, where no reduction step is required to produce a reactive surface for adsorption. Evidence for Fisher-Tropsch catalytic production of CH_4 is observed by mass spectroscopy during the initial cycles of Co film growth.

Spectroscopic Investigation of Hf-Si Oxynitride Alloys and Low Temperature Cobalt Metal ALD

by

Sang Jeong Oh

A dissertation submitted to the Graduate Faculty of
North Carolina State University
in partial fulfillment of the
requirements for the Degree of
Doctor of Philosophy

Materials Science and Engineering

Raleigh, North Carolina
2008

APPROVED BY :

Dr. Gregory N. Parsons **Co-chair of Advisory Committee**	**Dr. Jon Paul Maria** **Co-chair of Advisory Committee**
Dr. Mehmet C. Ozturk	**Dr. Nadia Elmasry**

BIOGRAPHY

The author was born in Pusan, South Korea. He received his B.S. degrees in Chemical Engineering in 1993 from Pohang University of Science and Technology. He worked for Samsung Electronics Research and Development Center of Semiconductor Division as a research engineer from December 1995 to August 2001. He completed the requirements for the Doctor of Philosophy degree in Materials Science and Engineering at North Carolina State University in the Fall of 2007.

ACKNOWLEDGEMENTS

I gratefully acknowledge and sincerely thank Dr. Gregory Parsons for the many opportunities he provided me, as well as his guidance and confidence in me. I also thank Dr. Jon-Paul Maria, Dr. Nadia Elmasry, Dr. Mehmet Ozturk, and Dr. Daniel J. Lichtenwalner for their helpful comments and serving on my advisory committee.

I would also like to thank Jeong-Suk Na, Michael Stewart, Dr. Kevin Hyde, Dr. Hojo Daisuke, Dr. Giovanna Scarel, Joe Spagnola, Qing Peng, Matt Glicksmann, Jaehoon Park and Hyung-Tag Seo for their thoughtful discussions and collaborations. It has truly been an honor and privilege for me to work with them.

I gratefully acknowledge the administrative and support staffs of the Materials Science and Engineering Department and would like to especially thank Edna Deas for her kindness, support and assistance.

Finally, I would like to thank my family. My parents and parents-in-law deserve special thanks for their continued support, encouragement, and prayer. Especially my wife, Inae, and son, Changyoon, are the best reason to complete this degree and move forward.

TABLE OF CONTENTS

LIST OF FIGURES…….....viii

LIST OF TABLES…….....xiv

1. Introduction : High Dielectric Constant Materials……1

1.1. The Need for High Dielectric Constant Materials……...1

1.2. The Dielectric Constant and Bond Ionicity……..2

1.3. The properties of dielectric materials : Electronegativity and Bond Ionicity…...5

1.4. Partial Charge……7

1.5. References……9

2. Deposition Techniques for HfO_2 and Hf silicate……19

2.1. MOCVD of HfO_2…….……..20

2.2. ALD of HfO_2……..22

2.3. MOCVD of Hf-Silicate……...……..24

2.3.1. Single Source Process……24

2.3.2. Dual Source Process……....25

2.4. ALD of Hf-Silicate…….....27

2.5. References……..29

3. Hf-Si Oxynitride Film Deposition……..…..41

3.1. Remote Plasma Enhanced Chemical Vapor Deposition, RPECVD……41

3.2. Metal Organic Source Delivery…….……..42

3.3 Auger Electron Spectroscopy……..…..43

3.4 XPS and FTIR……....43

3.5 Film Composition by AES……...……..44

3.5.1 Silicon oxynitride……..45

3.5.2 Hf silicate……...46

3.5.3. Hf-Si oxynitride……..……..47

3.6. References……..49

4. Spectroscopic Investigation of Chemical phase separation in Hf silicate and Hf-Si oxynitride alloys using FTIR and XPS……..……..……..60

4.1. Introduction…….……..60

4.2. FTIR Analysis……..……61

4.2.1. Experiments……...…..62

4.2.2. Results : FTIR Analysis…….....62

4.3. XPS Anaysis……...64

4.3.1. Experiments……64

4.3.2. Results : XPS Analysis……65

4.4. Discussion……..66

4.4.1. The Pseudo-binary (or ternary) alloys……..66

4.4.2. XPS Chemical Shifts: Charge-Potential Model……...67

4.4.3. Chemical Phase Separation……70

4.5. References……..72

5. Low Temperature Metal Atomic Layer Deposition……..87

5.1. Brief History of ALD……87

5.2. Characteristics of ALD……87

5.3. The needs of metal ALD……...89

5.4. Applications of ALD Metals……90

5.4.1. Interconnection Technology……..90

5.4.2. Gate Electrodes……...91

5.4.3. Magnetic nanostructure……92

5.4.4. Catalysis……...92

5.4.5. Nanotubes……93

5.5. Low temperature metal ALD……...93

5.6. References……..95

6. In-situ analysis of low temperature cobalt film formation using $Co_2(CO)_8$ and $Co(C_5H_5)(CO)_2$ in atomic layer deposition process sequencing……..……102

6.1. Abstract……..…….…102

6.2. Introduction……103

6.3. Experiments……104

6.4. Results and Discussion……106

6.5. Summary and Conclusions……112

6.6. References……113

LIST OF FIGURES

Chapter 1.

Figure 1.1. Frequency dependence of the several contributions to the polarizability……...13

Figure 1.2. Electronegativity relationship between Pauling's scale and Sanderson's scale……...14

Figure 1.3. Average bond ionicity, I_b, as a function of average electronegativity difference, ΔX.15

Figure 1.4. Oxygen atom coordination as function of average bond ionicity, I_b……...16

Figure 1.5. (a) Thermal data as function of average bond ionicity, I_b, (b) Band gap data as function of average bond ionicity, I_b……..17

Figure 1.6. Calculated partial charge for Hf, Si, and O in $(HfO_2)_X(SiO_2)_{1-X}$ alloys as a function of x from Eqn.1.12……..……18

Chapter 2.

Figure 2.1. Hafnium metalorganic precursors and their structures…….....40

Chapter 3.

Figure 3.1. Schematic of Remote Plasma Enhanced MOCVD Reactor…….52

Figure 3.2. Schematic of the Hf source gas delivery system. He carrier gas at 15 sccm is flowed through the bubbler and the flow is controlled by using feedback from a pressure transducer…53

Figure 3.3. On-line AES derivative spectra from Si oxynitride films with varying N_2O flow rate, the (N_2 + N_2O) flow rate was fixed at 200 sccm and He 50 sccm,

(a) Si-LVV, N-KLL, and O-KLL features.

(b) nitride and oxide characteristics of Si-LVV with respect to the N_2O flow rate……...54

Figure 3.4. Composition of oxynitride films as a function of N_2O in N_2 flow and He dilution…55

Figure 3.5. The effect of He dilution gas

(a) On-line AES derivative spectra from silicon oxynitride films with varying N_2O/He flow ratio.

(b) the composition of silicon oxynitride alloys with varying N_2O/He flow ratio……56

Figure 3.6. On-line AES derivative spectra for the $(HfO_2)_X(SiO_2)_{1-X}$ alloys with the range of from HfO_2 to SiO_2……..57

Figure 3.7. RBS-AES calibration for $(HfO_2)_x(SiO_2)_{1-x}$ composition…….57

Figure 3.8. (a) On-line AES derivative spectra for Hf-Si oxynitride alloys. (b) Ternary composition diagram of Hf-Si oxynitride alloys. The composition was calculated from N-KLL, O-KLL, and Hf-NVV intensities measured by on-line AES spectra…….58

Figure 3.9. Ternary composition diagrams of Hf-Si oxynitride alloys with the amount of He dilution (a) He 50 sccm. (b) He 100 sccm. (c) He 200 sccm……..59

Chapter 4.

Figure 4.1. IR transmission through a film/substrate system. The transmitted intensity, I, is approximated by Beer's law, $I = I_o\exp[\ -(A_f + A_s)\ ]$, where I_o is the incident beam intensity. A_f and A_s are the absorbance's of the film and substrate, respectively…….77

Figure 4.2. FTIR spectra of plasma deposited SiO_2 film, (a) sample and Si substrate (b) SiO_2 film only……77

Figure 4.3. FTIR spectra of as deposited alloys

(a) Si_3N_4, SiO_2, and SiON. (b) Hf silicate. (c) Hf-Si oxynitride…….78

Figure 4.4. FTIR spectra of Hf silicate $(HfO_2)_X(SiO_2)_{1-X}$ with respect to anneal temperatures

(a) X = 0.1. (b) X = 0.2. (c) X = 0.3. (d) X = 0.3 in detail……79

Figure 4.5. FTIR spectra of $(Si_3N_4)_X(SiO_2)_{0.5\cdot(1-X)}(HfO_2)_{0.5\cdot(1-X)}$ alloys with respect to anneal temperatures. (a) x = 0.07. (b) x = 0.17. (c) x = 0.33. (d) x = 0.49……...……80

Figure 4.6. XPS core-level Si 2p spectra with respect to anneal temperature of $(HfO_2)_X(SiO_2)_{1-X}$ (a) X=0.2. (b) X=0.4. $(Si_3N_4)_X(SiO_2)_{0.5\cdot(1-X)}(HfO_2)_{0.5\cdot(1-X)}$. (c) X = 0.13. (d) X = 0.33. (e) X = 0.50……81

Figure 4.7. XPS core-level Hf 4f spectra with respect to anneal temperature of $(HfO_2)_X(SiO_2)_{1-X}$. (a) X=0.2. (b) X=0.4. $(Si_3N_4)_X(SiO_2)_{0.5\cdot(1-X)}(HfO2)_{0.5\cdot(1-X)}$. (c) X = 0.13. (d) X = 0.33. (e) X = 0.50……82

Figure 4.8. XPS core-level N 1s spectra with respect to anneal temperature of $(Si_3N_4)_X(SiO_2)_{0.5\cdot(1-X)}(HfO2)_{0.5\cdot(1-X)}$. (a) X = 0.13. (b) X = 0.33. (c) X = 0.50……83

Figure 4.9. XPS core-level O 1s spectra and its corresponding first derivative spectra with respect to anneal temperature of $(HfO_2)_X(SiO_2)_{1-X}$. (a) X=0.2, (b) X=0.4……....84

Figure 4.10. XPS core-level O 1s spectra and its corresponding first derivative spectra with respect to anneal temperature of $(Si_3N_4)_X(SiO_2)_{0.5\cdot(1-X)}(HfO2)_{0.5\cdot(1-X)}$. (a) X = 0.13. (b) X = 0.33. (c) X = 0.50……85

Figure 4.11. Schematic representation of local bonding arrangement of Hf-Si oxynitride alloys with the composition of 33~40% of Si_3N_4, 30~33% of SiO_2 and HfO_2……86

Chapter 5.

Figure 5.1. Typical trends of growth rate as a function of growth temperature for the ALD process……100

Figure 5.2. Growth rate as a function of the amount of precursor exposure with surface saturation……101

Chapter 6.

Figure 6.1. AES spectra of substrates used in film deposition studies, including H-terminated silicon (Si-H) and chemically oxidized silicon. Adventitious carbon and some oxidation of the Si-H surface are observed due to ambient exposure after surface preparation. ……..116

Figure 6.2. Growth thickness per deposition cycle of the cobalt films on silicon deposited using $Co_2(CO)_8$ and H_2. (a) The film thickness increases linearly with the number of precursor/reactant exposure cycles at several deposition temperatures. (b) The growth thickness obtained with 3 seconds precursor exposure per cycle is plotted at various deposition temperatures. The lines are linear fits to the data points shown. (c) The growth per cycle is observed to increase continuously with increasing $Co_2(CO)_8$ precursor exposure time. The point at 30°C was estimated from Auger electron spectroscopy results……...117

Figure 6.3. Quadrupole mass spectroscopy signals obtained during deposition using $Co_2(CO)_8$ and H_2 at 100^{o}C with a pressure of 100 mTorr. Spectra are shown on a logarithmic scale (left) and a normalized linear scale (right). Signals are shown for Ar (40 amu), H_2 (2 amu), CO (28 amu), H_2O (18 amu), CH_4 (16 amu) and C_2H_6 (30 amu). The approximate times for the gas flow switching are indicated on the linear plot. Some delay in the QMS signal relative to the gas switching is observed due to gas residence time effects……..118

Figure 6.4. QMS signal obtained from CO (m/z = 28) during cobalt deposition using $Co_2(CO)_8$ precursor using: (a) different precursor exposure times at 100^{o}C with a pressure of 100 mTorr;

and (b) different deposition temperatures at 20 s precursor exposure time with a pressure of 500 mTorr. The signal at 30°C is ascribed to electron impact dissociation of the precursor in the mass spectrometer. Under all conditions studied, the CO mass signal increased with increasing exposure time……..….119

Figure 6.5. AES spectra of deposited film using $Co_2(CO)_8$ precursor at various deposition temperatures on Si-H substrates. The AES analysis was performed by direct sample transfer to the high vacuum chamber without ambient exposure. The data was collected after 100 - 300 deposition cycles using 3 s of precursor exposure per cycle, except for the sample deposited at 30°C. For the 30°C sample, the precursor exposure time was 20 seconds per cycle, and data was collected after 100 deposition cycles. The AES results indicate that films deposited at 100-130°C contain 25 ~ 30% carbon, and 5 ~ 10% oxygen……...120

Figure 6.6. Resistivity of deposited films versus deposition temperature using $Co_2(CO)_8$ precursor. The error bars represent one standard deviation from a set of 5 measurements on each sample……..……121

Figure 6.7. Quadrupole mass spectroscopy signals obtained during deposition using $Co(C_5H_5)(CO)_2$ and H_2 at 140°C with a pressure of 100 mTorr. Spectra are shown on a logarithmic scale (left) and a normalized linear scale (right). Signals are shown for Ar (40 amu), H_2 (2 amu), CO (28 amu), H_2O (18 amu), CH_4 (16 amu) and C_3H_3 (39 amu)…….....122

Figure 6.8. QMS signal obtained from CO (m/z = 28) during cobalt deposition using $Co(C_5H_5)(CO)_2$ precursor with different deposition temperatures with a pressure of 100 mTorr. The exposure times for the $Co(C_5H_5)(CO)_2$, Ar, H_2, and Ar deposition sequence were 5, 15, 15, and 15s respectively……....123

Figure 6.9. AES spectra of Co film using $Co(C_5H_5)(CO)_2$ precursor with respect to deposition temperature on SiO_2 surface : Data was collected after 300 cycles using 5 s of precursor exposure per cycle. The Co LMM AES signal is observed at deposition temperatures of 300 and 350°C……...124

LIST OF TABLES

Chapter 1.

Table 1.1. High-k dielectric material classification based on bond ionicity……12

Chapter 2.

Table 2.1. Precursor comparison for HfO_2 MOCVD…….36

Table 2.2. Precursor comparison for Hf silicate MOCVD……....37

Table 2.3. Precursor comparison for HfO_2 ALD……...38

Table 2.4. Precursor comparison for Hf silicate ALD……...39

Chapter 1. Introduction : High dielectric constant materials.

1.1. The Need for High Dielectric Constant Materials.

SiO_2 gate oxide has played a critical role in microelectronic device performance.[1-4] Until the recent era, the scaling of the gate dielectric has been accomplished by shrinking physical dimensions. As the physical thickness of SiO_2-based gate oxides approaches 1~2 nm, a number of fundamental problems arise. In this thickness regime, some key properties of gate dielectrics degrade: gate leakage current, oxide breakdown, boron penetration from the polysilicon gate electrode, and channel mobility.[2, 3] Each of these parameters is indispensable for device operation. This scaling down requires the replacement of conventional SiO_2 gate oxides with a material having higher permittivity. The primary motivation for this replacement is that physically thicker films with the same or thinner equivalent electrical oxide thickness (EOT) can reduce tunneling leakage current, as reported by several research groups.[5-8]

For the ideal alternative dielectric materials we need to consider more than just the high dielectric constant. Some necessary considerations include the (i) band gap and the subsequent conduction band offset with both silicon and the gate electrode,[9] (ii) thermal stability with silicon and against crystallization,[10] and (iii) ability to form a good interface with silicon substrates.[11, 12]

There are several candidates for high-k dielectric materials such as transition metal / rare earth (TM/RE) oxides (ZrO_2, HfO_2, Y_2O_3, La_2O_3), TM/RE silicates [$(ZrO_2)_X(SiO_2)_{1-X}$], [$(HfO_2)_X(SiO_2)_{1-X}$] and TM/RE aluminates [$(HfO_2)_X(Al_2O_3)_{1-X}$, $(La_2O_3)_X(Al_2O_3)_{1-X}$].[13-15] Recently, TM silicates were identified as attractive candidates since they have high dielectric constants to reduce the leakage current and are thermodynamically stable in contact with Si

substrate. Although the dielectric constants of TM/RE silicate films are smaller than those of metal oxides, silicate films are thermally more stable on the Si substrate.

However, chemical phase separation and crystallization often occurred when Hf and Zr silicates were annealed above 900°C.[16, 17] These problems caused not only the leakage current increase through the grain boundary and roughness of the film surface, but also further degradation of high-k characteristics.[18]

It has recently been reported that the N incorporation into the Hf-silicate also suppress crystallization.[19, 20] The incorporation of N is also useful to prevent interfacial reaction between dielectric films and the Si substrate and boron penetration from the boron doped polysilicon gate electrodes layer.[21]

1.2. The Dielectric Constant and Bond Ionicity

The electric susceptibility χ of a dielectric material is a measure of how easily it polarizes in response to an applied electric field. Generally, χ is a tensor, but it can be considered as a scalar for an isomorphic medium. If it is assumed that the response of a dielectric is linear to an applied electric field, and the applied electric field is not too strong, then the relationship between the polarization which is defined as the dipole moment per unit volume, P, and electric field, E, can be expressed with the constant of proportionality,

$$P = \chi E \qquad \text{(eqn.1.1)}$$

The electric displacement field D is related to P by

$$D = E + 4\pi P = (1 + 4\pi\chi)E \qquad \text{(eqn.1.2)}$$

therefore,

$$k(\omega) = 1 + 4\pi\chi(\omega) \qquad \text{(eqn.1.3)}$$

is the frequency dependent dielectric function. If the bonding configuration of a solid remains geometrically unchanged, an increase in bond ionicity will result in an increase in the dipole moment per unit volume when an electric field is applied. According to Eqn.s' 1.1 and 1.3, an increase in magnitude of the dipole moment per unit volume means an increase in the magnitude of k. A quantitative relationship between k and bond ionicity is now developed.

The polarization of a crystal may be expressed approximately as the product of the polarizabilities of the atoms times the local electric field:

$$P = \sum_j N_j \alpha_j E_{loc}(j) \qquad \text{(eqn.1.4)}$$

where Nj is the concentration and α_j the polarizability of atoms j, and $E_{loc}(j)$ is the local field at atom sites j. And from the Lorentz relation:

$$P = (\sum_j N_j \alpha_j)(E + \frac{4\pi}{3} P) \qquad \text{(eqn.1.5)}$$

And solve for P to find susceptibility, χ from Eqn.s' 1.1 and 1.5,

$$\chi = \frac{P}{E} = \frac{\sum N_j \alpha_j}{1 - \frac{4\pi}{3} \sum N_j \alpha_j} \qquad \text{(eqn.1.6)}$$

Eqn.s' 1.3 and 1.6 show that the larger polarizability of atoms results the higher dielectric constant k.

The total polarizability is composed of three parts with frequency dependence : electronic, ionic, and dipolar, as in Figure 1.1.[22] The contribution of electronic polarizability of the atom arises from the displacement of the electron shell relative to a nucleus in the region of optical frequencies. The ionic contribution comes from the displacement of a charged ion with respect to

other ions, which is due to lattice vibration in the region of infrared frequencies. The dipolar contribution arises from molecules with a permanent electric dipole moment that can change orientation in an applied electric field in the low frequencies (UHF to microwaves).

Assuming that the distinction between the total macroscopic field and the locally applied field is negligible, the well known oscillator (Drude) model was established as an analytical model for the complex dielectric function,[23]

$$k(\omega) = 1 + \Delta k_{ele} + \sum_{i=1}^{N} \frac{4\pi n_i q_i^2}{m_i(\omega_i^2 - \omega^2 - i\gamma\omega)} \qquad \text{(eqn.1.7)}$$

where N is the normal mode of vibration associated with ionic cores, n_i is the number of oscillators per unit volume, ω_i is the resonant frequency, γ_i is the damping coefficient, m_i is a reduced mass and q_i is the transverse infrared effective charge of the i-th oscillator. Δk_{ele} represents the electronic oscillators with a similar sum of ionic oscillators. At low frequencies (where $\omega_i >> \omega$), eqn.1.7 becomes

$$k(\omega) = 1 + \Delta k_{ele} + \sum_{i=1}^{N} \frac{4\pi n_i q_i^2}{m_i \omega_i^2} \qquad \text{(eqn.1.8)}$$

Therefore, in the low frequency limit k is approximately constant and is referred to as the static dielectric constant,

$$k \cong 1 + \Delta k_{ele} + \Delta k_{vib} \qquad \text{(eqn.1.9)}$$

where

$$\Delta k_{vib} = \sum_{i=1}^{N} \frac{4\pi n_i q_i^2}{m_i \omega_i^2} \qquad \text{(eqn.1.10)}$$

The transverse infrared effective charge for normal mode motions, q_i, is defined as the ratio between the change in the dipole moment per unit volume, ΔP_i, and a normal coordinate displacement, $\Delta\eta_i$, as follows:

Therefore, an increase in static k is due to (i) larger transverse infrared effective charges, qi, and (ii) smaller resonant frequencies, ω_i.

1.3. The properties of dielectric materials : Electronegativity and Bond Ionicity

Several different methods have been applied to approach electronegativity of the chemical elements. All methods show consistent trends which increase across each row in the periodic table from alkali metal to halogen.[24] There is a close relationship between electronegativity, *X*, and electronic structure, so that *X* can be a useful tool for defining a bond ionicity which is correlated to the electronic structure of the constituent atoms.[25] There is a conspicuous difference in electronegatvity scale between the Pauling scale and Sanderson scale. But since the Sanderson scale values are linear with the square root of the Pauling values (Figure 1.2.),[24] the use of each scale values with different definitions of bond ionicity does not modify any of the qualitative aspects of evaluating the partial charge in compounds.

Pauling made an empirical definition of bond ionicity, I_b, determined from atomic electronegativity differences as follows:

$$I_b = 1 - \exp(-0.25(\Delta X)^2) \qquad \text{(eqn.1.11)}$$

G. Lucovsky suggested the high-k dielectric materials classification scheme based on bond ionicity which is directly correlated with the electronic energy states of the constituent atoms through the atomic electronegativity in table 1.[26] The range of ΔX values from 1.5 to 2.4

corresponds to a bond ionicity range from 45% to 76%. Within this range, I_b is a linear function of ΔX as shown in figure 1.3., i.e. ΔX and I_b are equivalent scaling variables. Figure 1.4 demonstrates the correlation of the average bond ionicity to the oxygen atom coordination.[26] Since Ib is a linear function of ΔX in the range mentioned above, the average oxygen atom coordination also has a linear relationship with ΔX.

An increase in average bond ionicity tends to correspond to a decrease in crystallization temperatures; i.e. SiO_2 which is a continuous random network structure, $I_b = 0.45$, cannot be crystallized below its melting temperature, 1600°C, Al_2O_3 which is a modified continuous random network structure, $I_b = 0.57$, crystallizes at 900°C for a 30 second anneal in Ar ambient, and Ta_2O_5, $I_b = 0.61$, crystallizes at 800°C for the same anneal condition.[27] Both ZrO_2, $I_b = 0.71$, and HfO_2, $I_b = 0.68$, crystallize below 500°C.[28] The melting temperatures increase with the increase of average bond ionicity, but the crystallization temperatures show the opposite trend. (Figure 1.5 (a))

The band gap is also related to the local electronic states associated with the composing members of the material. The valence and conduction band edges are closely related to the atomic valence states for a material. From molecular orbital theory, the valence band is comprised of bonding orbitals and the conduction band of anti-bonding orbitals. The band offset data in table 1 are from J. Robertson's work and he used an internal photoemission method to predict a dielectric's conduction band offset with silicon.[29] Also, band gap data shows linear scaling with average bond ionicity (Figure 1.5 (b)).

1.4. Partial Charge

Sanderson developed an empirical method of evaluating bond ionicity by calculating partial charge on the basis of electronegativity equalization, which states when two or more atoms initially different in electronegativity combine chemically, they become adjusted toward an equal intermediate electronegativity in the compound.[24] This adjustment in electronegativities of the two atoms will stop at the point where equalization is reached by sharing the bonding electrons unevenly. The intermediate value of electronegativity is chosen by Sanderson to be the geometric mean of the constituent electronegativities, each appropriately weighted by their relative composition. This calculation is applied in an average way and does not take into account bonding characters or bonding coordinations of the same atom.

Sanderson, in Ref.24, makes two assumptions. One is that electronegativity changes linearly with partial atomic charges acquisition. A specific ionicity of 75% in NaF is assumed to establish the relative scale of partial charge. Based on these two assumptions, partial charge can be calculated with the following formula,

$$\delta_A = \frac{(S_A^x S_B^y S_C^z)^{1/(x+y+z)} - S_A}{2.08\sqrt{S_A}} \qquad \text{(eqn.1.12)}$$

where δ_A is the partial atomic charge of A atom in $A_xB_yC_z$ alloy, S_A, S_B, and S_C are the electronegativities of the constituent atoms, and $(S^x_A S^y_B S^z_C)^{1/(x+y+z)}$ is the compositionally averaged electronegativity of the alloy. The factor 2.08 was determined by the selection of 75% for the ionicity of NaF in above assumption. In this model, charge transfers occur among A, B, and C atoms until all atoms have the same electronegativity values. Based on Sanderson's model,

partial charges of Hf, Si, and O in pseudo-binary oxide $(HfO_2)_X(SiO_2)_{1-X}$ were calculated and presented in Figure 1.6. The necessary data for performing these calculations were taken from Ref.24. The electronegativity value 1.67 of Hf was calculated from the relationship between the Pauling scale and Sanderson scale (Figure 1.2.). The changes of the partial charge of each atoms show linear relationship with respect to composition x. With increasing x, the partial charges of Hf and Si decrease and that of O increases.

1.5. References

1. Lucovsky, G., *Ibm Journal of Research and Development* **1999,** 43, 301-326.

2. Buchanan, D. A., *Ibm Journal of Research and Development* **1999,** 43, 245-264.

3. Green, M. L.; Gusev, E. P.; Degraeve, R.; Garfunkel, E. L., *Journal of Applied Physics* **2001,** 90, 2057-2121.

4. Hori, T., *Gate dielectrics and MOS ULSIs : principles, technologies, and applications* Springer: New York 1997.

5. Houssa, M.; Ed., *High-k Gate Dielectrics*. Institute of Physics: Philadelphia, 2004.

6. Huff, H. R.; Gilmer, D. C.; Eds., *High dielectric constant materials : VLSI MOSFET applications*. Springer: New York 2005.

7. Demkov, A. A.; Navrotsky, A.; Eds., *Materials fundamentals of gate dielectrics*. Springer: Dordrecht 2005.

8. Wilk, G. D.; Wallace, R. M.; Anthony, J. M., *Journal of Applied Physics* **2001,** 89, 5243-5275.

9. Peacock, P. W.; Robertson, J., *Physical Review Letters* **2004,** 92, -.

10. Lucovsky, G.; Rayner, G. B.; Kang, D.; Hinkle, C. L.; Hong, J. G., *Applied Surface Science* **2004,** 234, 429-433.

11. Fischetti, M. V.; Neumayer, D. A.; Cartier, E. A., *Journal of Applied Physics* **2001,** 90, 4587-4608.

12. Gusev, E. P.; Narayanan, V.; Frank, M. M., *Ibm Journal of Research and Development* **2006,** 50, 387-410.

13. Callegari, A.; Cartier, E.; Gribelyuk, M.; Okorn-Schmidt, H. F.; Zabel, T., *Journal of Applied Physics* **2001,** 90, 6466-6475.

14. Gilmer, D. C.; Hegde, R.; Cotton, R.; Smith, J.; Dip, L.; Garcia, R.; Dhandapani, V.; Triyoso, D.; Roan, D.; Franke, A.; Rai, R.; Prabhu, L.; Hobbs, C.; Grant, J. M.; La, L.; Samavedam, S.; Taylor, B.; Tseng, H.; Tobin, P., *Microelectronic Engineering* **2003,** 69, 138-144.

15. Zhu, W. J.; Tamagawa, T.; Gibson, M.; Furukawa, T.; Ma, T. P., *Ieee Electron Device Letters* **2002,** 23, 649-651.

16. Rayner, G. B.; Kang, D.; Hinkle, C. L.; Hong, J. G.; Lucovsky, G., *Microelectronic Engineering* **2004,** 72, 304-309.

17. Maria, J. P.; Wickaksana, D.; Parrette, J.; Kingon, A. I., *Journal of Materials Research* **2002,** 17, 1571-1579.

18. Neumayer, D. A.; Cartier, E., *Journal of Applied Physics* **2001,** 90, 1801-1808.

19. Visokay, M. R.; Chambers, J. J.; Rotondaro, A. L. P.; Shanware, A.; Colombo, L., *Applied Physics Letters* **2002,** 80, 3183-3185.

20. Bastos, K. P.; Driemeier, C.; Pezzi, R. P.; Soares, G. V.; Miotti, L.; Morais, J.; Baumvol, I. J. R.; Wallace, R. M., *Materials Science and Engineering B-Solid State Materials for Advanced Technology* **2004,** 112, 134-138.

21. Quevedo-Lopez, M. A.; El-Bouanani, M.; Kim, M. J.; Gnade, B. E.; Wallace, R. M.; Visokay, M. R.; LiFatou, A.; Chambers, J. J.; Colombo, L., *Applied Physics Letters* **2003,** 82, 4669-4671.

22. Kittel, C., *Introduction to Solid State Physics*. 7 ed.; John Wiley and Sons: New York, 1996.

23. Jackson, J. D., *Classical Electrodynamics*. 2 ed.; John Wiley and Sons: New York, 1975.

24. Sanderson, R. T., *Chemical bonds and bond energy* 2ed.; Academic Press Inc.: New York, 1971.

25. Pauling, L., *The Nature of the Chemical Bond* 3ed.; Cornell University Press Ithaca, 1960.

26. Lucovsky, G., *Journal of Vacuum Science & Technology A* **2001,** 19, 1553-1561.

27. Johnson, R. S.; Hong, J. G.; Lucovsky, G., *Journal of Vacuum Science & Technology B* **2001,** 19, 1606-1610.

28. Ushakov, S. V.; Navrotsky, A.; Yang, Y.; Stemmer, S.; Kukli, K.; Ritala, M.; Leskela, M. A.; Fejes, P.; Demkov, A.; Wang, C.; Nguyen, B. Y.; Triyoso, D.; Tobin, P., *Physica Status Solidi B-Basic Research* **2004,** 241, 2268-2278.

29. Robertson, J., *European Physical Journal-Applied Physics* **2004,** 28, 265-291.

Table 1.1. High-k dielectric material classification based on bond ionicity.

Dielectrics	ΔX	I_b	Coordination		Band gap	CB Offset	VB Offset	$k\varepsilon_0$	melting point	crystallization temperature	refractive index
			Metal / Silicon	Oxygen							
Continuous Random Networks											
SiO_2	1.54	0.45	4	2.0	8.9	3.5	4.4	3.9	1610		1.46
CRNs with network Modifiers											
Al_2O_3	1.84	0.57	4 - 6	3.0	8.8	2.8	4.9	9	2072	900	1.65
Ta_2O_5	1.94	0.61	6 - 8	2.8	4.4	0.3	3.0	26	1872	800	2.09
TiO_2	1.90	0.59	6	3.0	3.05			80	1850		2.40
$(ZrO_2)_{0.1}(SiO_2)_{0.9}$	1.61	0.48	8 - 4	2.2	6.9	1.4	4.4	6	2670	900	
$(ZrO_2)_{0.23}(SiO_2)_{0.77}$	1.70	0.51	8 - 4	2.46	6.7	1.4	4.2	~ 12	2600		
$(ZrO_2)_{0.5}(SiO_2)_{0.5}$	1.88	0.59	8 - 4	3.0	6.3	1.4	3.8	~ 13	2400	970	
$(TiO_2)_{0.5}(SiO_2)_{0.5}$	1.72	0.52	6 - 4	2.5							
$(Y_2O_3)_1(SiO_2)_2$	1.88	0.59	6 - 4	2.86					1830		
$(Y_2O_3)_2(SiO_2)_3$	1.93	0.61	6 - 4	3.0					1900		
$(Y_2O_3)_1(SiO_2)_1$	1.99	0.63	6 - 4	3.11					1980		
$(Al_2O_3)_4(ZrO_2)_1$	2.02	0.64	4 - 8	3.0					2450	550	
$(Al_2O_3)_3(Y_2O_3)_1$	1.97	0.62	4 - 6	3.0							
Random Close Packed Ions											
HfO_2	2.14	0.68	8	4.0	6.0	1.4	3.3	25	2812	472	2.0
ZrO_2	2.22	0.71	8	4.0	5.8	1.5	3.4	25	2715	426	1.96
$(La_2O_3)_2(SiO_2)_1$	2.18	0.70	6 - 4	3.5					1800		
Y_2O_3	2.22	0.71	6	4.0	5.6	2.3	2.6	15	2410		1.80
La_2O_3	2.34	0.75	6	4.0	5.6	2.3	2.6	30	2315		

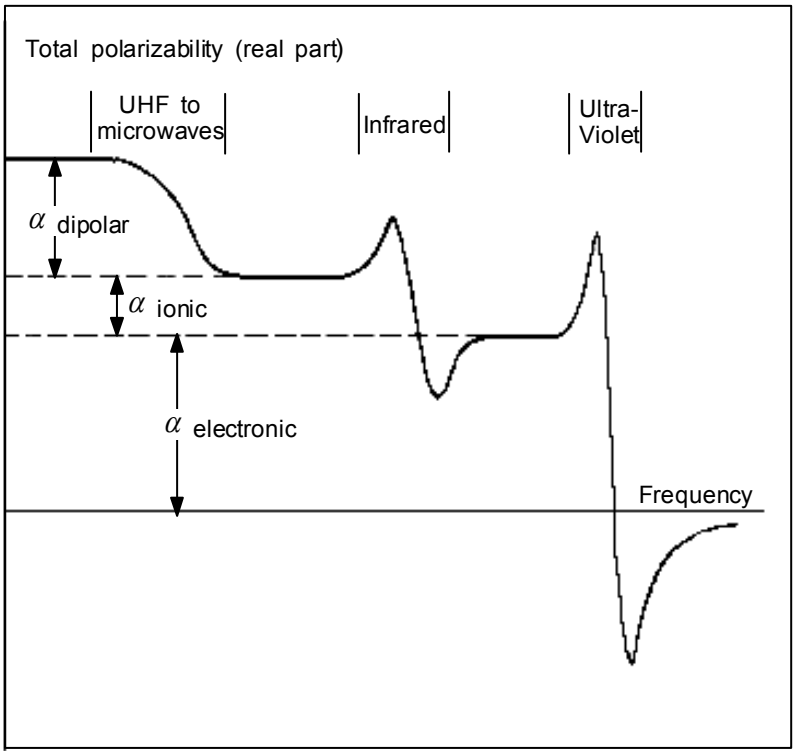

Figure 1.1. Frequency dependence of the several contributions to the polarizability.

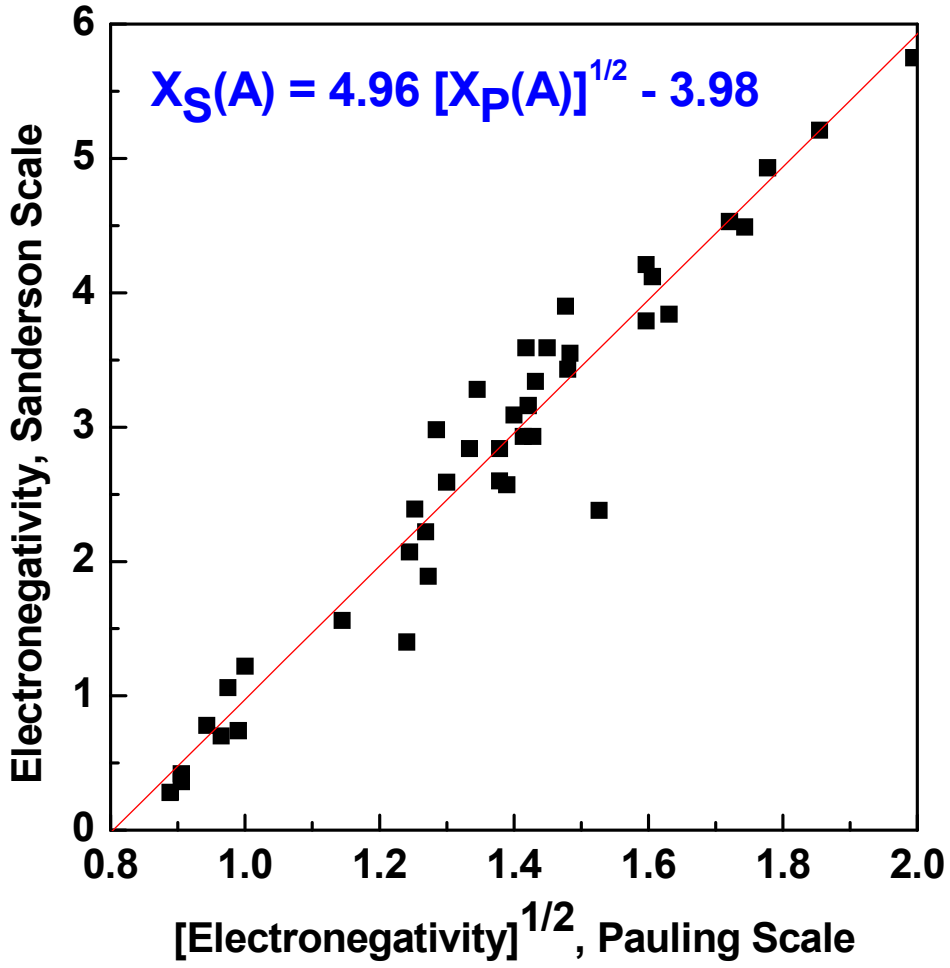

Figure 1.2. Electronegativity relationship between Pauling's scale and Sanderson's scale.

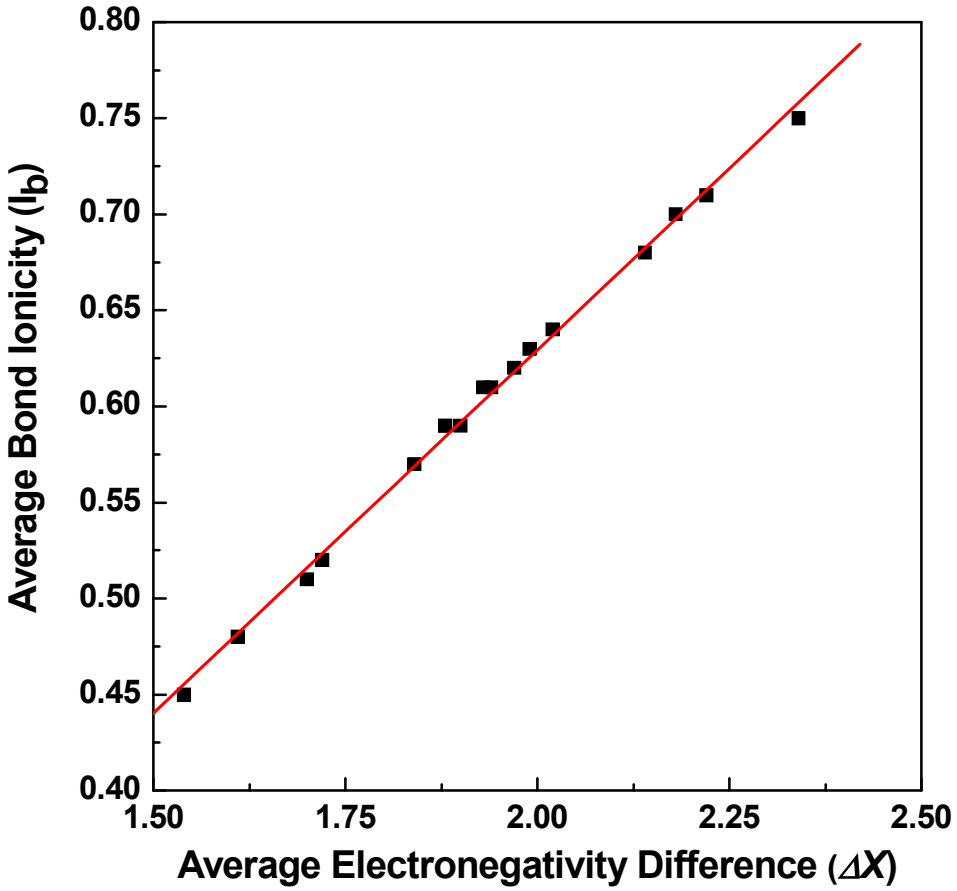

Figure 1.3. Average bond ionicity, I_b, as a function of average electronegativity difference, ΔX.

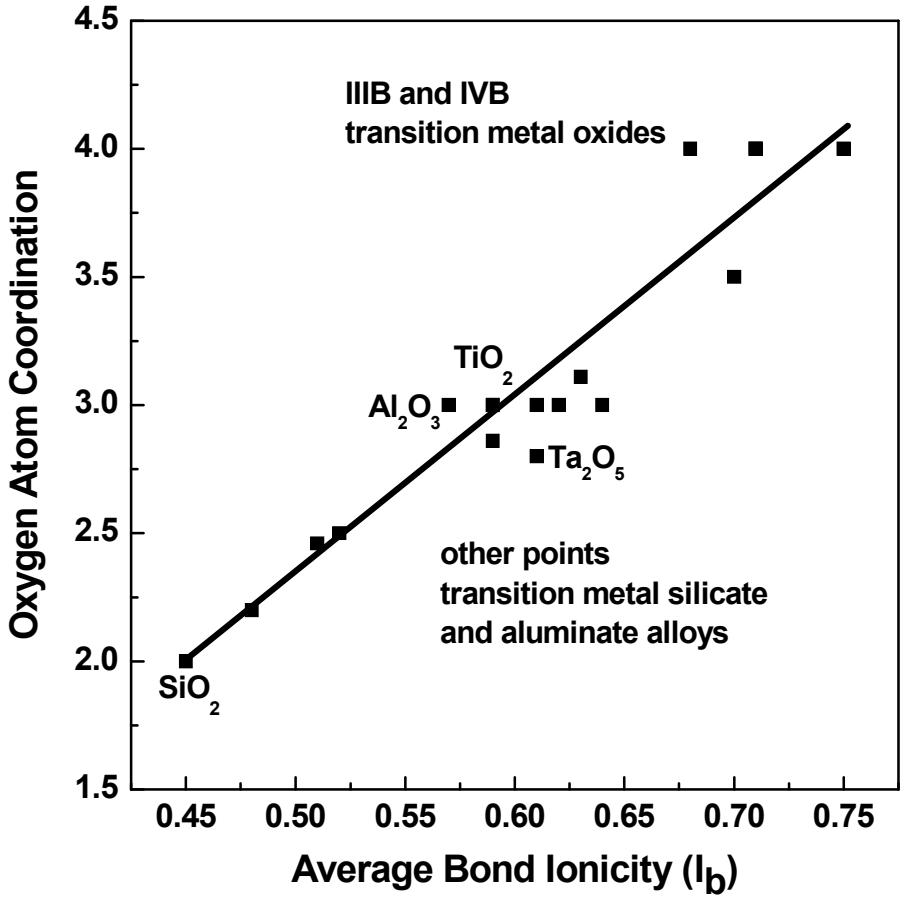

Figure 1.4. Oxygen atom coordination as function of average bond ionicity, I_b.

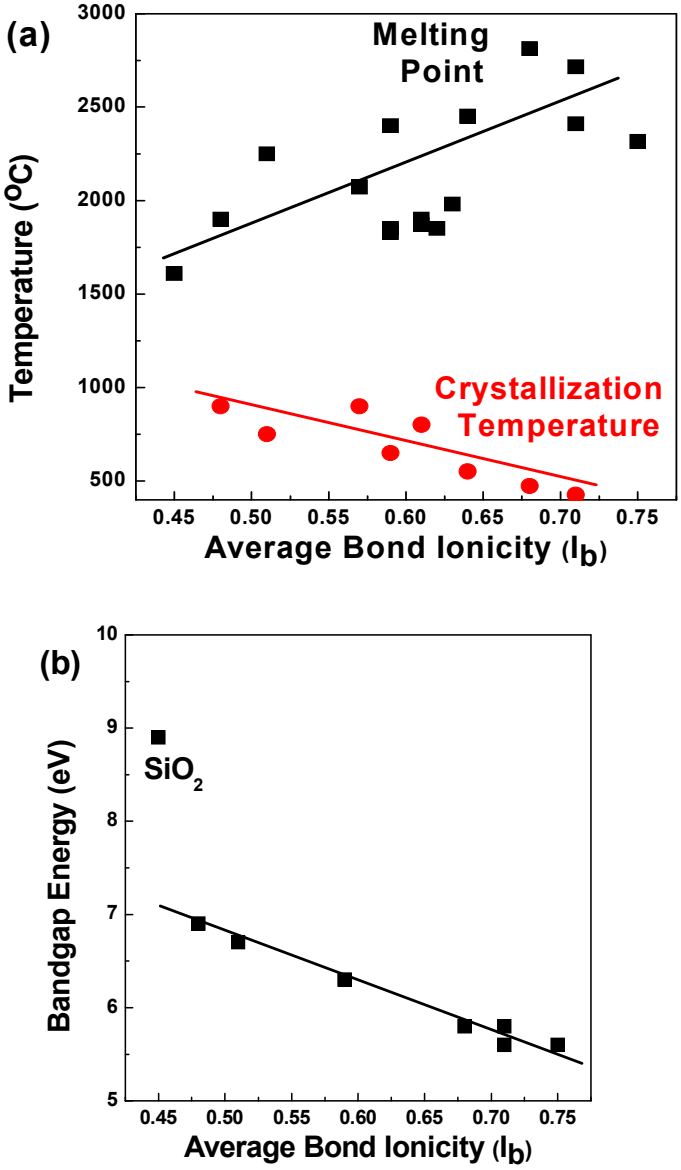

Figure 1.5. (a) Thermal data as function of average bond ionicity, I_b.

(b) Band gap data as function of average bond ionicity, I_b.

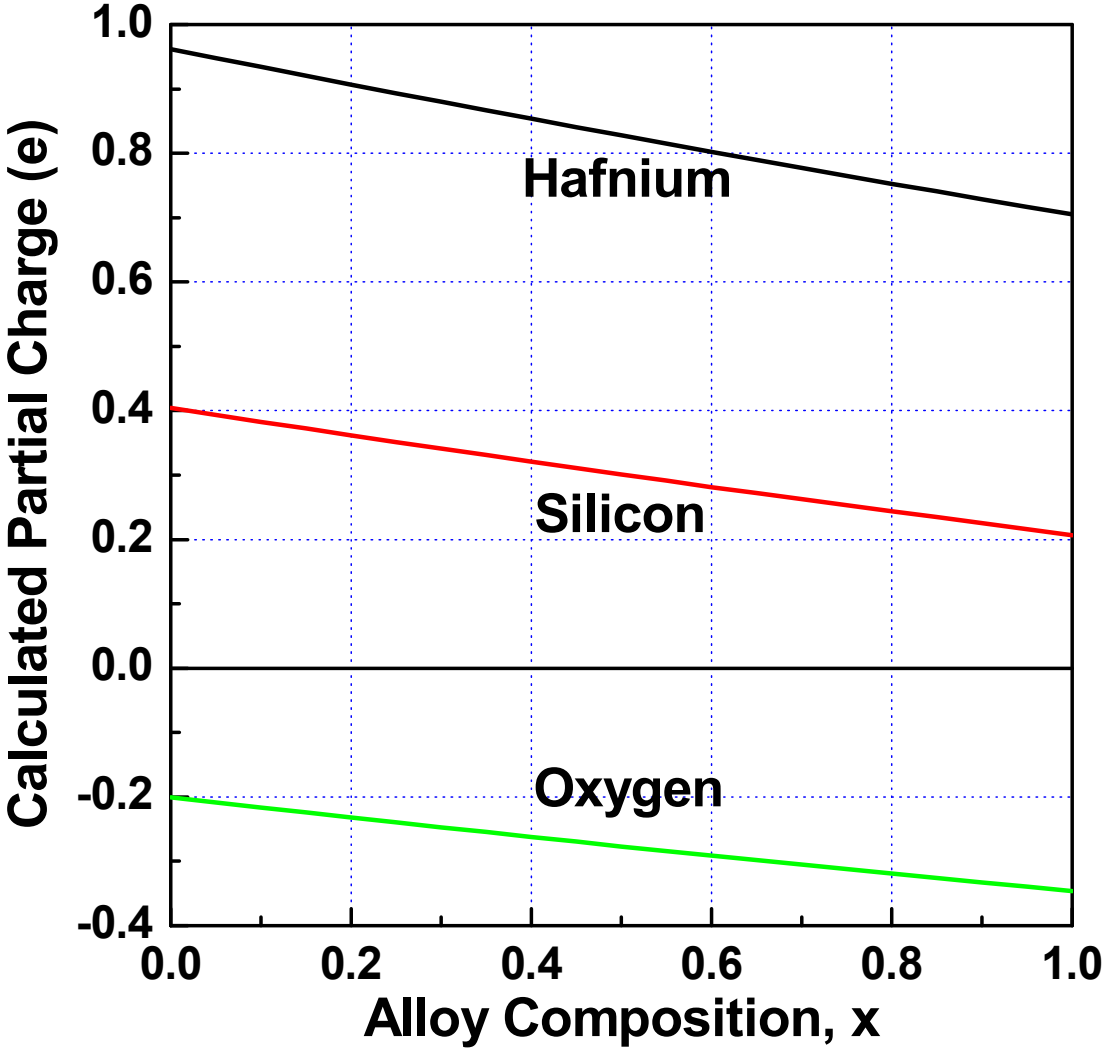

Figure 1.6. Calculated partial charge for Hf, Si, and O in $(HfO_2)_X(SiO_2)_{1-X}$ alloys as a function of x from Eqn.1.12.

Chapter 2. Deposition Techniques for HfO_2 and Hf silicate.

Various techniques have been used and developed for the deposition of dielectric materials (metal oxides metal silicates, and metal aluminates, etc) including physical vapor deposition (RF and DC sputtering, molecular-beam epitaxy, laser ablation), solution deposition (sol-gel, metal organic decomposition), MOCVD, and ALD. Among these techniques, MOCVD and ALD are well suited for microelectronics manufacturing.

MOCVD has the advantages of ease of manufacture, control of deposition rate, high film uniformity, good composition control, and excellent conformality on non-planar device structure. Since MOCVD processes involve the decomposition of a metal-organic precursor, it is very important to use a proper precursor.

ALD is a modification of MOCVD, in which gaseous precursors are sequentially introduced to the substrate surface alternately or simultaneously by purging steps with inert gas or evacuation. It also has the advantages of good large area uniformity, outstanding conformal step coverage, and atomic level control of film composition and thickness. In ALD processes, the reactions are saturative so that film growth automatically stops (or self-limits) at each layer. The film growth rate is therefore independent of the precursor pulse amount.

Since precursors with the appropriate physical properties and decomposition chemistry are essential for successful MOCVD and ALD processes, many studies have been done in the molecular design of high-k material precursors.

2.1. MOCVD of HfO_2

MOCVD precursors have a high vapor pressure at reasonable source temperatures for mass transportation into the deposition chamber. Liquids and gaseous precursors are preferred because the vapor pressure is relatively high and easy to use with conventional delivery methods. Since the evaporation rate of solid precursors is dependent on the source surface area, the mass transfer into the deposition system can be inconsistent.

The deposition temperature is also important. Because of the aggressive device scaling, low temperature processes are required to prevent the reaction between layers and interdiffusion of dopants.

Metal chlorides were among the first compounds used in MOCVD processing. $ZrCl_4$ and $HfCl_4$ are solids which sublime at nearly 300℃, and need substrate temperatures higher than 800℃ for oxide deposition.[1] It may lead to significant oxidation of a silicon substrate and chloride contamination in the films. HfI_4 can decrease the deposition temperature under 700℃, and halogen contamination was reduced compared to the $HfCl_4$ precursor.[1, 2]

The metal nitrates $Zr(NO_3)_4$ and $Hf(NO_3)_4$ have been used for ZrO_2 and HfO_2 films at deposition temperatures as low as 300℃. They are the only single source precursors that are free from halogen, carbon, and hydrogen. The source temperature for zirconium and hafnium nitrate is 80℃. Because the nitrate ligands themselves are strongly oxidizing, no additional oxygen source is required for deposition. However, there is a problem of interfacial layer formation.[3-5]

Metal alkoxides are attractive as precursors due to their high vapor pressures and lower deposition temperatures. However, because Zr and Hf atoms have a tendency to expand their coordination to six, seven or eight, many $Zr(OR)_4$ and $Hf(OR)_4$ complexes make dimers or

polymers easily.[6] The bulky group ligands such as tert-butoxide can prevent metal alkoxide polymerization, and $Hf(OtBu)_4$ have been successfully used for HfO_2 deposition.[7-11] These precursors are highly air- and moisture-sensitive, and must be handled under inert conditions.

In order to prevent the polymerization of metal alkoxides, β-diketonate complexes[12] and mixed ligand (alkoxide + β-diketonate) presursors[13-16] are developed. They are generally more stable against hydrolysis than alkoxides. The vapor pressure of mixed ligand precursors lies between the alkoxides and β-diketonates. In mixed ligand precursors, the source temperature is similar for β-diketonate complexes.[6, 13-16]

The alkylamide complexes $[Hf(NR_2)_4]$ are used for the deposition of metal oxide thin films. $Hf(NEt_2)_4$ was used with conventional MOCVD, because it is a liquid at room temperature and has moderate vapor pressure.[17-19] The interfacial layer formed during the HfO_2 deposition was hafnium silicate, and the Hf / (Hf+Si) ratio of the interfacial layer increased with increasing deposition time.[19] The incorporation of residual carbon and nitrogen was suppressed by increasing oxygen flow rates and increasing substrate temperatures,[17] but like alkoxides, alkylamide precursors are also reactive with air and moisture.[20] $Hf(NMeNMe_2)_4$ and $Hf[^tBuNCH_2CH_2N\text{-}^tBu]_2$ were used as precursors for HfO_2 film deposition.[21] The films grown from $Hf(NMeNMe_2)_4$ produced almost stoichiometric ($HfO_{1.9}$), and residual carbon and nitrogen free films, while $Hf[^tBuNCH_2CH_2N\text{-}^tBu]_2$ produced films with the composition of $HfO_{1.6}C_{0.06}N_{0.2}$.

The hydroxylamide complexes $[Zr(ONR_2)_4]$ and $[Hf(ONR_2)_4]$ are less reactive and easier to handle in liquid injection MOCVD than alkylamide precursors. Williams compared $Hf(NMe_2)_4$ and $Hf(ONEt_2)_4$, and generally the films grown in the $Hf(ONEt_2)_4$ showed lower

carbon impurity level than those in the $Hf(NMe_2)_4$ grown films. The HfO_2 films deposited from $Hf(ONEt_2)_4$ contained lower carbon impurity levels due to the direct Hf-O bonding in precursor. Compared to alkylamide, the film growth window is narrow in substrate temperature range.[22] $Hf(OEtNMe_4)_4$ has higher vapor pressure than $Hf(OtBu)_4$ and $Hf(NEt_4)_4$, and the deposition temperature is lower than any other precursors.[23]

2.2. ALD of HfO_2

The reactions in the ALD process are saturative. This makes the film growth self-limiting. Because the growth rate is independent of source material dose, solid sources are more easy to use in ALD than MOCVD.

The first ALD processes for HfO_2 were based on $HfCl_4$ and water. Halide precursors show high thermal stability, and good self-limiting growth behavior.[24-26] In this process, HfO_2 deposition can start only on the oxidized or hydroxylated surface. A nonuniformly oxidized surface leads to poor nucleation of HfO_2 which makes the film morphology nonuniform. This problem can be avoided by using thin SiO_2 as a buffer (or starting) layer.[25] Residual chlorine left from the precursors can be a problem in regard to electrical performance. As an alternative, HfI_4 has been studied.[2, 27, 28] HfI_4 is similar to the $HfCl_4$, but the Hf-I bond strength is weaker and the size of iodide are larger than chloride. This may result in less amounts of halide residue. Since hafnium halides are high melting point solid sources, there is a risk of particle transport to the substrate and also the purity of precursors is questionable.

The metal alkoxides have high purity but show poor thermal stability. The $Zr(OtBu)_4$ was studied in detail, but the precursor decomposed and failed to give self-limiting growth.[29]

Replacement of the $[O^tBu]_4$ ligand by $[OCMe_2CH_2OMe]_4$[30] or $[(O^tBu)_2(OCMe_2CH_2OMe)_2]$[31] improved thermal stability. The decomposition of both $Hf(mmp)_4$ and $Hf(O^tBu)_2(mmp)_2$ could be reduced by lowering the substrate temperature under 300℃. But none of the complexes showed fully self-limiting growth behavior. $Hf(OCMeEt_2)_4$ precursor was recently studied by Cho et.al[32]. $OCMeEt_2$ is bulkier than the *tert*-butoxide ligand, and therefore it is expected to effectively improve the thermal stability without much loss of volatility and growth rate in the ALD of HfO_2. It also showed self-limiting growth behavior at 250℃.

The metal alkylamides showed fully self-limiting growth.[33-38] Carbon impurity concentrations in the film were lower than alkoxide ($Hf(mmp)_4$) grown film.[33] However, hydrogen was not fully desorbed from the films because of the low deposition temperature. It was found that the deposition temperature could be increased in steps of 50℃ in the order of $M(NMe_2)_4 < M(NEtMe)_4 < M(Net_2)_4$.[34] Compared to halide precursors, this compound shows higher conformality.

Hafnium nitrate $Hf(NO_3)_4$ has also been used as a precursor for ALD.[39] This precursor is free from hydrocarbon or halogen impurities and the nitrogen oxide is easily removable. But nitrate complexes are more attractive to MOCVD than ALD, due to its decomposition at low temperature.

The hydroxylamide complexes are thermally more stable than alkylamide groups.[40] The $Hf(ONR_2)_4$ complex is monomeric and Hf is 8-fold coordinated. The (ONR_2) ligand is bidentate and shields the Hf center more effectively than monodentate alkylamide ligand, so it is less reactive than alkylamide precursors.

2.3. MOCVD of Hf-Silicate

HfO_2 film is not chemically or thermally stable on Si. Lower-*k* interfacial layers are formed parasitically during deposition of the dielectric or post-deposition anneal in oxygen ambient, and reduce the gate dielectric capacitance. HfO_2 film was amorphous when it was deposited, however, it crystallize at temperature below 500℃. Crystallization is, generally, undesirable since it introduces grains into the gate dielectric. As a possible solution to this problem, metal silicates, such as $(ZrO_2)_X(SiO_2)_{1-X}$ or $(HfO_2)_X(SiO_2)_{1-X}$ are introduced. The dielectric constants of these alloys are lower than that of the pure metal oxides, but this is acceptable as a trade-off for the improved interface stability.

There are various precursor combinations for $(HfO_2)_X(SiO_2)_{1-X}$ film deposition. They can be categorized into two approaches. The first uses single-sources in which both Hf and Si atoms exist. This approach can make the process relatively simple, but it is difficult to alter the metal : silicon concentration ratio in the film due to the fixed Hf : Si ratio in the precursors. The second uses two separated precursors, which enables fine-tuning of the film compositions.

2.3.1. Single Source Process

$[Hf(OSi^tBuMe_2)_4(HNEt_2)]$ was used for the liquid injection MOCVD of hafnium silicate thin films, with the range of deposition temperatures 350 ~ 50℃[41]. The amount of silicon incorporation in the films varies within approximately 5 ~ 10 at% and does not depend on substrate temperature. Carbon contamination decreased when temperature and oxygen flow increased.

$[Hf(OSi^tBuMe_2)_2(CH_3COCHCOCH_3)_2]$ were used by M. Lemberger et.al.[42] Deposition was carried out at 550℃. Carbon contamination was 20 at% as-deposited, but after O_2 ambient RTA treatment, no carbon was found within the detection limit of XPS. Silicon incorporation level was around 15% (Si / (Hf+Si)).

Various single sources were synthesized by LG. Pfalzgraf et.al. to deposit hafnium silicate films[43]. $(HfO_2)_X(SiO_2)_{1-X}$ films were deposited at 600-800℃ using $Hf(thd)_2X_2$ derivatives [thd = tetramethylheptanedionato, X = $N(SiMe_3)_2$, $OSiMe_3$ and $OSitBuMe_2$] as precursors. The amounts of Hf with respect to Si was Hf / (Hf+Si) = 0.70 - 0.85. The Si / (Si+Hf) ratio in the films was significantly lower than in the initial precursor without dependence on the deposition temperature. The Si / (Si+Hf) ratio difference between the surface and in the film were found.

2.3.2. Dual Source Process

Many studies in the deposition of hafnium silicate films have involved separate precursors for the hafnium and the silicon, with the oxygen source as a third one.

$Hf(O^tBu)_4$ and SiH_4 combination was used by V. Rangarajan et.al.[44] MOCVD and plasma enhanced CVD were compared. At a fixed flow ratio of two sources, plasma enhanced CVD was favorable for Si incorporation in silicates almost 6 times more than in thermally deposited silicates. The deposition rate of plasma enhanced CVD was 2 times higher than that of thermal MOCVD. Carbon impurities were under XPS detection limit for both deposition methods.

$Hf(O^iPr)_4$ and TEOS combination were used with plasma enhanced MOCVD by H. Kato et.al.[45] The deposited films were found as pseudobinary compounds. No Hf-Si bonds were

detected with XPS work. The amounts of silicon incorporation were successfully controlled in a wide range (0.0 ~ 1.0) with changing the flow ratio of two sources.

The combinations using alkylamide complexes for metal were categorized with respect to silicon source with similar ligands such as $Si(NR_2)_4$ and $SiH(NR_2)_3$[46-50] or different types such as $^tBuMe_2SiOH$ and $Si(O^nBu)_4$.[51, 52]

Precursor solutions were prepared as mixtures of $Hf(NEt_2)_4$ and $Si(NMe_2)_4$ with different ratios by BC. Hendrix et.al.[46] The SiO_2 composition of $(HfO_2)_X(SiO_2)_{1-X}$ films were changed from 33 % to 62 % with increasing silicon source concentration in the mixed precursors and increasing deposition temperature. Carbon and nitrogen levels in the films were under 0.5 at%.

Y. Ohshita et.al. used $Hf(NEt_2)_4$ as a metal precursor, and combined with $SiH(NEt_2)_3$, Si(NCO), and $Si(OEt)_4$ as silicon precursors.[48] When $Si(OEt)_4$ was used as a silicon precursor, the carbon concentration decreased as the substrate temperature increased. On the other hand, when $SiH(NEt_2)_3$ or $Si(NCO)_4$ was used as a Si precursor, carbon impurities in the films decreased and saturated as the substrate temperature decreased. In a similar way, the amount of residual nitrogen in the films deposited using $Si(OEt_2)_4$ decreased as the substrate temperature increased, while it increased with the substrate temperature when $(Et_2N)_3SiH$ or $Si(NCO)_4$ was used.

PR Chalker et.al. reported the characterization of $(HfO_2)_X(SiO_2)_{1-X}$ films using $Hf(NMe_2)_4$ and the alkylsilanol $^tBuMe_2SiOH$ as precursors in a liquid injection MOCVD process.[51] Since $Hf(NMe_2)_4$ and $^tBuMe_2SiOH$ react at room temperature to form a non-volatile $Hf[OSi(O^tBu)_3]_4$ or related species, each source should be injected independently. Nitrogen was

not detected by AES, but carbon was detected at levels 1.9～6.3 at%. SiO_2 composition increased with increasing silicon precursor concentration, but saturated at 40 %.

$Hf(NEt_2)_4$ was used as metal precursor to produce less carbon and halogen free hafnium silicate film. Instead of using a separate oxygen source, J. Kim et.al. used $Si(O^nBu)_4$ to suppress the formation of low-k interfacial layer because the Si-O bonds are strong and short, silicon alkoxides would be less oxidizing toward silicon than water, oxygen or ozone.[52] $(HfO_2)_{0.1}(SiO_2)_{0.9}$ film was deposited with k value of ～8. Carbon concentration was less then 0.1 at%.

2.4. ALD of hafnium silicate

Mixed oxides such as metal silicates are deposited simply by combining binary oxide ALD cycles as mixed or as separated manners.

The combinations of $HfCl_4$ as a metal precursor with $Si(OEt)_4$,[53] $Si(O^nBu)_4$,[54] and $NH_2(Me)_3Si(OEt)_3$[55] as silicon precursors were studied. It is difficult to use silicon halides for silicon precursors, because the reactivity of silicon halides are very low at low temperatures.[56] K. Kukli et.al. deposited films with composition close to $HfSiO_4$ with $Si(OEt)_4$ / H_2O / $HfCl_4$ / H_2O cycles.[53] The amount of residual chlorine was less than 0.5 at%. An interface layer (0.8-1.4 nm) was formed between the films and substrate. In the case of $Si(O^nBu)_4$ as a silicon source, the growth rate and Hf composition fraction decreased with increasing deposition temperatures.[54] Rittersma et.al. used $NH_2(Me)_3Si(OEt)_3$, and controlled Hf / Si ratio with changing the pulse time of each sources.[55] Both SiO_2-rich and HfO_2-rich as-deposited films had roughly 10% excess oxygen, i.e., O / (Hf + Si) ratio is higher than two.

$Hf(OCMe_2CH_2OMe)_2(O^tBu)_2$ and $Si(OCMe_2CH_2OMe)_4$ combination was studied by Van Elshocht et.al.[57] The composition of the films was changed by varying the Hf / Si pulse ratio. It was different from conventional ALD in that the precursors and the oxidant (O_2) were introduced simultaneously not sequentially. Xuan et.al. reported the hafnium silicate deposition at room temperature using both alkoxide type precursors $Hf(O^tBu)_4$ for metal and $Si(OEt)_4$ for silicon.[58] Oxidant H_2O was used as a liquid phase instead of vapor phase.

Various hafnium alkylamide complexes with silicon precursors are studied for hafnium silicate film deposition. Senzaki et.al. deposited homogeneous hafnium silicate films using co-injection of hafnium and silicon precursors with identical $(NEtMe)_4$ ligand.[59] The films were deposited below 400℃ with ozone as an oxidant. Carbon and hydrogen incorporation was below 1 at%, nitrogen levels were below the detection limit. 1.0nm interface layers were formed independent of silicate film thickness. The precursor combinations of $SiH(NMe_2)_3$ and $SiH_2(NMe_2)_2$ with $Hf(NEtMe)_4$ were studied by Kamiyama et.al.[60] The Hf / (Hf + Si) compositions of hafnium silicate films deposited using $SiH_2(NMe_2)_2$ and $SiH(NMe_2)_3$ precursors could be easily controlled. Carbon impurity in the film from $SiH2(NMe_2)_2$ was about an order of magnitude less than that from $SiH(NMe_2)_3$. The combination of hafnium alkylamide and silicon alkoxide was studied by Kim et.al., silicon alkoxide was also used as an oxidant.[61] Under the condition for self-limiting growth, the Hf / (Hf+Si) composition was saturated at approximately 0.37. Carbon contamination was less than 1 at% based on XPS analyses.

$HfCl_2[N(SiMe_3)_2]_2$ single source with water was used for ALD deposition of hafnium silicate films by Rhee's research group.[62, 63] As the deposition temperature increased (150 - 400℃), the growth rate decreased but the composition ratio of Si / (Hf + Si) increased up to 0.3.

2.5. References

1. Smith, R. C.; Ma, T. Z.; Hoilien, N.; Tsung, L. Y.; Bevan, M. J.; Colombo, L.; Roberts, J.; Campbell, S. A.; Gladfelter, W. L., *Advanced Materials for Optics and Electronics* **2000,** 10, 105-114.

2. Forsgren, K.; Harsta, A.; Aarik, J.; Aidla, A.; Westlinder, J.; Olsson, J., *Journal of the Electrochemical Society* **2002,** 149, F139-F144.

3. Park, S. W.; Kim, D. J.; Lee, C. H.; Lee, S. C.; Kwak, N. Y.; Shin, S. W.; Park, J. H.; Suh, M. S.; Kong, Y. T.; Dong, C. D.; Yang, H. S., *Journal of the Electrochemical Society* **2002,** 149, G441-G445.

4. Smith, R. C.; Hoilien, N.; Roberts, J.; Campbell, S. A.; Gladfelter, W. L., *Chemistry of Materials* **2002,** 14, 474-476.

5. Zhong, L. J.; Zhang, Z. H.; Campbell, S. A.; Gladfelter, W. L., *Journal of Materials Chemistry* **2004,** 14, 3203-3209.

6. Williams, P. A.; Roberts, J. L.; Jones, A. C.; Chalker, P. R.; Bickley, J. F.; Steiner, A.; Davies, H. O.; Leedham, T. J., *Journal of Materials Chemistry* **2002,** 12, 165-167.

7. Frank, M. A.; Sayan, S.; Dormann, S.; Emge, T. J.; Wielunski, L. S.; Garfunkel, E.; Chabal, Y. J., *Materials Science and Engineering B-Solid State Materials for Advanced Technology* **2004,** 109, 6-10.

8. Kumagai, A.; Zhang, H.; Ishibashi, K., *Vacuum* **2004,** 74, 461-465.

9. Sayan, S.; Aravamudhan, S.; Busch, B. W.; Schulte, W. H.; Cosandey, F.; Wilk, G. D.; Gustafsson, T.; Garfunkel, E., *Journal of Vacuum Science & Technology a-Vacuum Surfaces and Films* **2002,** 20, 507-512.

10. Triyoso, D. H.; Ramon, M.; Hegde, R. I.; Roan, D.; Garcia, R.; Baker, J.; Wang, X. D.; Fejes, P.; White, B. E.; Tobin, P. J., *Journal of the Electrochemical Society* **2005,** 152, G203-G209.

11. Zhang, Z.; Xia, B.; Gladfelter, W. L.; Campbell, S. A., *Journal of Vacuum Science & Technology A* **2006,** 24, 418-423.

12. Yang, T. S.; An, K. S.; Lee, E. J.; Cho, W.; Jang, H. S.; Park, S. K.; Lee, Y. K.; Chung, T. M.; Kim, C. G.; Kim, S.; Hwang, J. H.; Lee, C.; Lee, N. S.; Kim, Y., *Chemistry of Materials* **2005,** 17, 6713-6718.

13. Loo, Y. F.; O'Kane, R.; Jones, A. C.; Aspinall, H. C.; Potter, R. J.; Chalker, P. R.; Bickley, J. F.; Taylor, S.; Smith, L. M., *Journal of Materials Chemistry* **2005,** 15, 1896-1902.

14. Lu, Y.; Buiu, O.; Hall, S.; Hurley, P. K., *Microelectronics Reliability* **2005,** 45, 965-968.

15. Dubourdieu, C.; Rauwel, E.; Millon, C.; Chaudouet, P.; Ducroquet, F.; Rochat, N.; Rushworth, S.; Cosnier, V., *Chemical Vapor Deposition* **2006,** 12, 187-192.

16. Patil, U.; Thomas, R.; Milanov, A.; Bhakta, R.; Ehrhart, P.; Waser, R.; Becker, R.; Becker, H. W.; Winter, M.; Merz, K.; Fischer, R. A.; Devi, A., *Chemical Vapor Deposition* **2006,** 12, 172-180.

17. Ohshita, Y.; Ogura, A.; Hoshino, A.; Hiiro, S.; Machida, H., *Journal of Crystal Growth* **2001,** 233, 292-297.

18. Takahashi, K.; Nakayama, M.; Yokoyama, S.; Kimura, T.; Tokumitsu, E.; Funakubo, H., *Applied Surface Science* **2003,** 216, 296-301.

19. Van Elshocht, S.; Caymax, M.; De Gendt, S.; Conard, T.; Petry, J.; Date, L.; Pique, D.; Heyns, M. M., *Journal of the Electrochemical Society* **2004,** 151, F77-F80.

20. Milanov, A.; Bhakta, R.; Thomas, R.; Ehrhart, P.; Winter, M.; Waser, R.; Devi, A., *Journal of Materials Chemistry* **2006,** 16, 437-440.

21. Lehn, J. S. M.; Javed, S.; Hoffman, D. M., *Chemical Vapor Deposition* **2006,** 12, 280-284.

22. Williams, P. A.; Jones, A. C.; Tobin, N. L.; Chalker, P. R.; Taylor, S.; Marshall, P. A.; Bickley, J. E.; Smith, L. M.; Davies, H. O.; Critchlow, G. W., *Chemical Vapor Deposition* **2003,** 9, 309-314.

23. Song, M. K.; Kang, S. W.; Rhee, S. W., *Thin Solid Films* **2004,** 450, 272-275.

24. Ritala, M.; Leskela, M.; Niinisto, L.; Prohaska, T.; Friedbacher, G.; Grasserbauer, M., *Thin Solid Films* **1994,** 250, 72-80.

25. Aarik, J.; Aidla, A.; Kiisler, A. A.; Uustare, T.; Sammelselg, V., *Thin Solid Films* **1999,** 340, 110-116.

26. Cho, M. J.; Park, J.; Park, H. B.; Hwang, C. S.; Jeong, J.; Hyun, K. S., *Applied Physics Letters* **2002,** 81, 334-336.

27. Kukli, K.; Ritala, M.; Sundqvist, J.; Aarik, J.; Lu, J.; Sajavaara, T.; Leskela, M.; Harsta, A., *Journal of Applied Physics* **2002,** 92, 5698-5703.

28. Kukli, K.; Ritala, M.; Sajavaara, T.; Keinonen, J.; Leskela, M., *Thin Solid Films* **2002,** 416, 72-79.

29. Kukli, K.; Ritala, M.; Leskela, M., *Chemical Vapor Deposition* **2000,** 6, 297-302.

30. Kukli, K.; Ritala, M.; Leskela, M.; Sajavaara, T.; Keinonen, J.; Jones, A. C.; Roberts, J. L., *Chemistry of Materials* **2003,** 15, 1722-1727.

31. Kukli, K.; Ritala, M.; Leskela, M.; Sajavaara, T.; Keinonen, J.; Jones, A. C.; Roberts, J. L., *Chemical Vapor Deposition* **2003,** 9, 315-320.

32. Cho, W.; An, K. S.; Chung, T. M.; Kim, C. G.; So, B. S.; You, Y. H.; Hwang, J. H.; Jung, D. G.; Kim, Y., *Chemical Vapor Deposition* **2006,** 12, 665-669.

33. Kukli, K.; Ritala, M.; Sajavaara, T.; Keinonen, J.; Leskela, M., *Chemical Vapor Deposition* **2002,** 8, 199-204.

34. Hausmann, D. M.; Kim, E.; Becker, J.; Gordon, R. G., *Chemistry of Materials* **2002,** 14, 4350-4358.

35. Kukli, K.; Ritala, M.; Lu, J.; Harsta, A.; Leskela, M., *Journal of the Electrochemical Society* **2004,** 151, F189-F193.

36. Kukli, K.; Pilvi, T.; Ritala, M.; Sajavaara, T.; Lu, J.; Leskela, M., *Thin Solid Films* **2005,** 491, 328-338.

37. Cho, M.; Park, H. B.; Park, J.; Lee, S. W.; Hwang, C. S.; Jang, G. H.; Jeong, J., *Applied Physics Letters* **2003,** 83, 5503-5505.

38. Yokoyama, Y.; Zhu, S. Y.; Nakajima, A., *Japanese Journal of Applied Physics Part 1-Regular Papers Brief Communications & Review Papers* **2006,** 45, 7091-7093.

39. Conley, J. F.; Ono, Y.; Zhuang, W.; Tweet, D. J.; Gao, W.; Mohammed, S. K.; Solanki, R., *Electrochemical and Solid State Letters* **2002,** 5, C57-C59.

40. Kukli, K.; Ritala, M.; Leskela, M.; Sajavaara, T.; Keinonen, J.; Jones, A. C.; Tobin, N. L., *Chemical Vapor Deposition* **2004,** 10, 91-96.

41. Roberts, J. L.; Marshall, P. A.; Jones, A. C.; Chalker, P. R.; Bickley, J. F.; Williams, P. A.; Taylor, S.; Smith, L. M.; Critchlow, G. W.; Schumacher, M.; Lindner, J., *Journal of Materials Chemistry* **2004,** 14, 391-395.

42. Lemberger, M.; Paskaleva, A.; Zurcher, S.; Bauer, A. J.; Frey, L.; Ryssel, H., *Microelectronics Reliability* **2005,** 45, 819-822.

43. Hubert-Pfalzgraf, L. G.; Touati, N.; Pasko, S. V.; Vaissermann, J.; Abrutis, A., *Polyhedron* **2005,** 24, 3066-3073.

44. Rangarajan, V.; Bhandari, H.; Klein, T. M., *Thin Solid Films* **2002,** 419, 1-4.

45. Kato, H.; Nango, T.; Miyagawa, T.; Katagiri, T.; Seol, K. S.; Ohki, Y., *Journal of Applied Physics* **2002,** 92, 1106-1111.

46. Hendrix, B. C.; Borovik, A. S.; Xu, C.; Roeder, J. F.; Baum, T. H.; Bevan, M. J.; Visokay, M. R.; Chambers, J. J.; Rotondaro, A. L. P.; Bu, H.; Colombo, L., *Applied Physics Letters* **2002,** 80, 2362-2364.

47. Machida, H.; Kada, T.; Ishikawa, M.; Ogura, A.; Ohshita, Y., *Japanese Journal of Applied Physics Part 1-Regular Papers Short Notes & Review Papers* **2004,** 43, 966-967.

48. Ohshita, Y.; Ogura, A.; Ishikawa, M.; Kada, T.; Hoshino, A.; Suzuki, T.; Machida, H.; Soai, K., *Chemical Vapor Deposition* **2006,** 12, 130-135.

49. Consiglio, S.; Papadatos, F.; Naczas, S.; Skordas, S.; Eisenbraun, E. T.; Kaloyeros, A. E., *Journal of the Electrochemical Society* **2006,** 153, F249-F254.

50. Driemeier, C.; Chambers, J. J.; Colombo, L.; Baumvol, I. J. R., *Applied Physics Letters* **2006,** 89, Art. No. 051921.

51. Chalker, P. R.; Marshall, P. A.; Potter, R. J.; Joyce, T. B.; Jones, A. C.; Taylor, S.; Noakes, T. C. Q.; Bailey, P., *Journal of Materials Science-Materials in Electronics* **2004,** 15, 711-714.

52. Kim, J.; Yong, K., *Journal of Crystal Growth* **2004,** 263, 442-446.

53. Kukli, K.; Ritala, M.; Leskela, M.; Sajavaara, T.; Keinonen, J.; Hegde, R. I.; Gilmer, D. C.; Tobin, P. J., *Journal of the Electrochemical Society* **2004,** 151, F98-F104.

54. Kim, W. K.; Rhee, S. W.; Lee, N. I.; Lee, J. H.; Kang, H. K., *Journal of Vacuum Science & Technology A* **2004,** 22, 1285-1289.

55. Rittersma, Z. M.; Roozeboom, F.; Verheijen, M. A.; van Berkum, J. G. M.; Dao, T.; Snijders, J. H. M.; Vainonen-Ahlgren, E.; Tois, E.; Tuominen, M.; Haukka, S., *Journal of the Electrochemical Society* **2004,** 151, C716-C722.

56. George, S. M.; Ott, A. W.; Klaus, J. W., *Journal of Physical Chemistry* **1996,** 100, 13121-13131.

57. Van Elshocht, S.; Weber, U.; Conard, T.; Kaushik, V.; Houssa, M.; Hyun, S.; Seitzinger, B.; Lehnen, P.; Schumacher, M.; Lindner, J.; Caymax, M.; De Gendt, S.; Heyns, M., *Journal of the Electrochemical Society* **2005,** 152, F185-F189.

58. Xuan, Y.; Hojo, D.; Yasuda, T., *Applied Physics Letters* **2004,** 84, 5097-5099.

59. Senzaki, Y.; Park, S.; Chatham, H.; Bartholomew, L.; Nieveen, W., *Journal of Vacuum Science & Technology A* **2004,** 22, 1175-1181.

60. Kamiyama, S.; Miura, T.; Nara, Y.; Arikado, T., *Electrochemical and Solid State Letters* **2005,** 8, G215-G217.

61. Kim, J.; Yong, K., *Journal of the Electrochemical Society* **2005,** 152, F45-F48.

62. Nam, W. H.; Rhee, S. W., *Electrochemical and Solid State Letters* **2004,** 7, C55-C56.

63. Kang, S. W.; Rhee, S. W.; George, S. M., *Journal of Vacuum Science & Technology A* **2004,** 22, 2392-2397.

Table 2.1. Precursor comparison for HfO_2 MOCVD.

	Advantages	Disadvantages
halide		because of low volatility, needs high substrate temperature > 800℃ lead to substrate oxidation
anhydrous nitrate	can be used as a single source no hydrocarbon, no halogen High purity oxide film	nitrate ligands are strongly oxidizing, make easily silicate interfacial layer safety concern
alkoxide	bulky sterical ligands suppress oligomerization, sufficient vapor pressure to allow a reasonable deposition rate with a R.T. bubbler	sensitive to moisture and must be handled under inert atmosphere condition
β-diketonate	more stable against hydrolysis than alkoxides	require source temperature around 200℃ for sufficient vaporization, fluorinated compounds can cause contamination
mixed ligand (alkoxide + β-diketonate)	more stable against hydrolysis than alkoxides, vapor pressure lies between alkoxides and β-diketonate	no improvement on source temperature
alkylamide	moderate vapor pressure low residual contamination	high reactivity with air
hydroxylamide	quasi eight-coordinate monomers i.e. less reactive and easier to handle thermally stable	narrow film growth window compared to alkylamide

Table 2.2. Precursor comparison for Hf silicate MOCVD.

<table>
<tr><td colspan="2">Precursor</td><td>Advantages</td><td colspan="2">Disadvantages</td></tr>
<tr><td colspan="2">Single Source</td><td rowspan="4">better homogeneity and lower temperature of deposition</td><td colspan="2">limited Si incorporation</td></tr>
<tr><td colspan="2">$Hf(OSi^tBuMe_2)_4(HNEt_2)$</td><td rowspan="3">Si /(Si+Hf)</td><td>0.10~0.15</td></tr>
<tr><td colspan="2">$Hf(OSi^tBuMe_2)_2(CH_3COCHCOCH_3)_2$</td><td>0.15</td></tr>
<tr><td colspan="2">$Hf(thd)_2X_2$
X= $N(SiMe_3)_2$, $OSiMe_3$, $OSi\text{-}^tBuMe_3$</td><td>0.15~0.30</td></tr>
<tr><td>hafnium</td><td>silicon</td><td colspan="3"></td></tr>
<tr><td rowspan="2">alkoxide</td><td>SiH_4</td><td rowspan="2"></td><td colspan="2" rowspan="2"></td></tr>
<tr><td>$Si(OEt)_4$</td></tr>
<tr><td rowspan="3">alkylamide</td><td>$Si(NR_2)_4$</td><td>mixture solutions possible due to similar ligand</td><td colspan="2">nitrogen impurity</td></tr>
<tr><td>$^tBuMe_2SiOH$</td><td>no nitrogen detected</td><td colspan="2">Si/(Si+Hf) saturated up to 0.4</td></tr>
<tr><td>$Si(O^nBu)_4$</td><td>Si source can be used as an oxidant and suppress the low-k interfacial layer</td><td colspan="2"></td></tr>
</table>

Table 2.3. Precursor comparison for HfO_2 ALD.

	Advantages	Disadvantages
halide	good self-limiting growth behavior due to high thermal stability	risk of particle transport to substrate limitation of chemical purity halide contamination
alkoxide	high chemical purity	failed to give truly self-limiting growth due to decomposition low growth rate : steric inhibition of the surface exchange reaction interfacial layer (SiOx)
alkylamide	good self-limiting growth behavior relatively lower residual carbon than alkoxide 'O' and 'halogen' free	hydrogen impurities due to the low growth temperatures
anhydrous nitrate	No hydrocarbon, No halogen	silicate interfacial layer
hydroxylamide	higher thermal stability than alkylamide higher growth rate than alkoxide	

Table 2.4. Precursor comparison for Hf silicate ALD.

Precursor		Advantages	Disadvantages
single source : $HfCl_2[N(SiMe_3)_2]_2$		better homogeneity and lower temperature of deposition	limited Si incorporation up to 0.3
hafnium	silicon		
halide	$Si(OEt)_4$		residual halogen impurities
	$Si(^nOBu)_4$		0.8～1.4nm thick interfacial layer
	$NH_2(Me)_3Si(OEt)_3$	easy composition control with change in pulse time	non-stoichiometric film : 10% excess Oxygen
alkoxide	$Si(OCMe2CH2OMe)_4$	oxidant was introduced simultaneously with each Hf and Si source	
	$Si(OEt)_4$	liquid water was used as an oxidant for complete hydrolysis reaction	
alkylamide	$Si(NEtMe)_4$	co-injection possible due to identical ligand	1.0 nm thick interfacial layer
	$SiH(NMe_2)_3$ $SiH2(NMe_2)_2$	both have high vapor pressure	$SiH(NMe_2)_3$: high "C" impurity
	$Si(O^nBu)_4$	Si source can be used as an oxidant	composition is fixed within self-limiting growth condition

Precursors	Examples and Molecular Structure	
Metal Halides	$HfCl_4$ HfI_4	
Metal Alkoxides	$Hf[OC(CH_3)_3]_4$	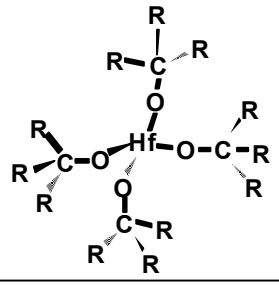
Metal Alkylamide	$Hf[N(CH_3)_2]_4$ $Hf[N(C_2H_5)2]_4$ $Hf[N(CH_3)(C_2H_5)]_4$	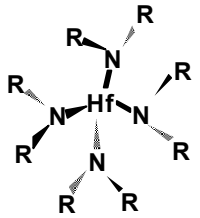
Metal Nitrates	$Hf(NO_3)_4$	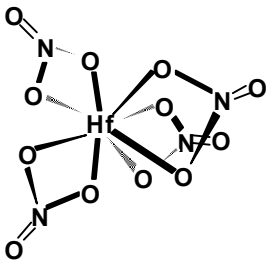
Metal b-diketonates	$Hf(O_2C_5H_7)_4$ $Hf(O_2C_{11}H_{19})_4$	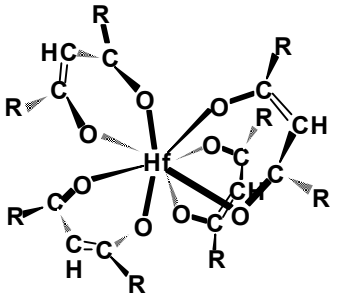
Metal Hydroxylamide	$Hf(ONR_2)_4$	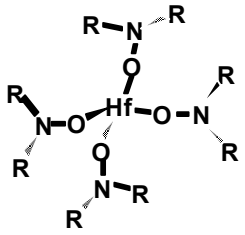

Figure 2.1. Hafnium metalorganic precursors and their structures.

Chapter 3. Hf-Si Oxynitride Film Deposition.

3.1 Remote Plasma Enhanced Chemical Vapor Deposition, RPECVD

Hf-Si oxynitride were deposited by a remote plasma enhanced-metal organic chemical vapor deposition (RPE-MOCVD) process onto Si substrates. The RPE-MOCVD process, used in this research, modifies an existing RPE-CVD process that has been used for the formation of silicon dioxide, silicon nitride, and oxynitride by adding a MO precursor.[1, 2]

The RPECVD system is different from conventional or direct plasma processing. It provides a way to selectively activate gases by isolating the plasma to a certain region in order to avoid damage on the substrate surface due to plasma contact. The excited gases are injected through a quartz plasma tube and the others, source gases, through a shower head ring (Figure 3.1. Reactor schematic). Film deposition occurs outside the glow region, and the source gases are prevented from back streaming into the plasma region by a combination of pressure difference and gas flow.[1]

A schematic of the reactor and the Hf source gas delivery system,[3] are illustrated in Figure 3.1 and 3.2, respectively. The base pressure of the RPE-MOCVD reactor was approximately $5x10^{-7}$ Torr.

The Si-substrates were pretreated in a H_2O/HF (100:1) solution to remove the superficial native oxide and make a clean, hydrogen terminated, Si surface. In the reactor, the Si-substrate was located on the heater stage and heated to temperature (300°C) by three halogen lamps. This temperature (300°C) is enough to desorb organics remaining on the substrate surface after wet cleaning and prevent thermal oxidation by ambient oxygen. The heater temperature was controlled by a k-type thermocouple (TC) attached to the heater stage which was correlated to

the sample temperature using a 3 inch Si wafer (SensArray Corp.) with a k-type TC embedded in the center.

He, O_2, N_2, and N_2O gases were excited by the RF power 30 W at 13.56 MHz. The respective Si and Hf source gases, 2% SiH_4 in He and Hf(IV) t-butoxide, were delivered directly into the substrate region of the remote plasma reactor in Figure. 3.1 through two different shower-head injectors. The flow ratio of all the gases was adjusted to control the composition of the films. Independent of source gas flow rates, the reactor pressure was maintained at 300 mTorr during film deposition.

Films were annealed ex-situ in an inert Ar ambient atmosphere utilizing an AG minipulse 310 rapid thermal annealing (RTA) apparatus. A cantilever-type TC (SensArray Corp.) in contact with a Si coated graphite susceptor (AG and Associates) was used to control the RTA temperature. Sample annealing temperature was calibrated using Si-substrates fitted with k-type TCs embedded in the center of the polished side. The Si-substrates were placed on the susceptor and the substrate temperature was monitored during the annealing process.

3.2 Metal Organic Source Delivery

The metal organic Hf precursor was supplied from a stainless-steel bubbler (AirProducts; BK1200SSZ),[4] and synthesized by Strem Chemicals with 99.99% purity. The bubbler temperature was controlled at 20℃ using a heat bath (Neslab; RTE 211) filled with silicone oil. Transportation and evaporation of the metal organic precursor was controlled by a closed loop controller monitoring an absolute Baratron and operating a needle valve (MKS; controller, MKS250; Baratron, 631A12TBEH; power supply, 260PS-3B; needle valve, 148JA13CR1M).

The boiling point of the Hf precursor is 90℃ at 760 Torr.[5] Therefore, the gas lines were kept at approximately 100℃ and He was flowed constantly through the gas line to prevent metal organic precursor condensation in the lines. Typically, the pressure was varied in the bubbler between 30 and 90 Torr, where an increase in bubbler pressure results in a decrease of Hf source gas injection.

3.3 Auger Electron Spectroscopy

AES was performed with a Physical Electronics 11-010 5kV electron gun control, 10-155 cylindrical mirror analyzer (CMA), 32-150 digital analyzer control, 137 PC interface board assembly, 96A V/f preamplifier, 32-100 electron multiplier power supply, and the software interface program AES_CGA. To prevent electron beam induced damage on the surface, we have used a minimal beam technique. It means that the current of the beam is kept low and the detector multiplier voltage high.[6] The beam is focused before each use to get the maximum number of counts. For consistent results, the multiplier voltage is kept at 4.0 on the 32-100 power supply dial corresponding to 1,444 volts. The accelerating voltage is set at 2.0 keV and the main elastic peak is aligned to 2.0 keV. The filament current is kept between 900 and 1000 kilo counts per second allowing for repeatable results over a long period of time for AES scans run at 3.0 keV.

3.4 XPS and FTIR

Off-line XPS measurements were performed using a Riber LAS-3000 spectrometer with non-monochromatic Mg Kα radiation (1253.6 eV) and a pass energy of 20 eV. The spectral

resolution was approximately 1 eV. The system base pressure for XPS measurements was approximately $3x10^{-10}$ Torr. Data were corrected for charging effects using the C1s peak at 284.6 eV from adventitious carbon contamination on the film surface.[7] The repeatability of measuring peak spectral positions was found to be < 0.2 eV.

IR absorption measurements, in the mid-IR (4000 ~ 400 cm-1) and far-IR (700 ~ 50 cm-1) regions of the electromagnetic spectrum, were performed with a Nicolet Magna-FTIR 750 spectrometer. N_2 gas purged the spectrometer continuously to minimize absorption from IR active components present in the atmosphere, e.g., H_2O and CO_2. The spectrometer utilizes a He/Ne laser for optical bench alignment prior to all data collection. The mid-IR measurements utilized a DTGS detector (with a KBr window) and a KBr beam splitter; the far-IR measurements a DTGS detector (with a polyethylene window) and a Si-substrate beam splitter. A bare reference Si-substrate, from the same wafer used in the deposition process, was used for substrate subtraction. The reference samples were treated with 100:1 HF, as described in section 3.1, prior to IR measurements. Film thickness was greater than approximately 1500 Å thick to ensure good IR absorption sensitivity.

3.5 Film Composition by AES

Prior to depositing Hf-Si oxynitride film, the pseudo-binary alloys Si oxynitride $[(Si_3N_4)_X(SiO_2)_{1-X}]$ and Hf silicate $[(HfO_2)_X(SiO_2)_{1-X}]$ are deposited and analyzed using AES to control the film composition. The term pseudo-binary (or ternary) alloys means that alloys are one phase and their local atomic structures are the same as those of end members.

3.5.1 Silicon oxynitride

Si oxynitride [$(Si_3N_4)_X(SiO_2)_{1-X}$] films are deposited on Si (100) substrate. The Si source gas, 2% SiH_4 in He 10 sccm is flowed through shower head rings in reactor. The combination of 1% N_2O in N_2 and N_2 gases and He(dilution gas) are flowed through a quartz tube for nitridation as well as oxidation since oxygen incorporates significantly easier to the films than nitrogen. The other process conditions were fixed at 300℃ substrate temperature, 300 mTorr reactor pressure, and 30W of 13.56 MHz RF plasma power.

On-line derivative AES spectra of Si oxynitride films with varying composition are shown in Figure 3.3. The sum of N_2 and N_2O (1% N_2O in N_2) is held constant at 200 sccm, and He is 50 sccm. As N_2O flow increases, O-KLL feature (510 eV)[8] gradually increase and N-KLL (380 eV)[8] feature decreases concomitantly. The position of the Si-LVV line shifts from 82 eV to 78 eV, (83 eV for Si_3N_4 and 76 eV for SiO_2)[8] This indicates that the film is Si oxynitride, the pseudobinary alloy of Si_3N_4 and SiO_2.

The film compositions were determined from the comparison of the relative intensities in the differential AES spectra. Si, O, and N concentrations were derived from the Si-LVV, O-KLL, and N-KLL intensities, using the relationship given by $C_X = (I_X / S_X) / (\Sigma I_i / S_i)$,[7] where C_X is the concentration of species x in atomic percent, I_X is its intensity in the AES spectrum defined as the peak-to-background amplitude, and S_X is its sensitivity factor.

The composition of Si oxynitride film was represented in terms of the pseudobinary alloy $(Si_3N_4)_X(SiO_2)_{1-X}$. The composition parameter, *x*, in the pseudobinary alloy was calculated from atomic percent of the constituent atoms. $R = (I_N/S_N) / (I_O/S_O)$ is obtained from the relative intensities of the O–KLL and N–KLL AES features, and the composition parameter, x, is

obtained from the relationship x = R / (2 + R).[9] The composition parameter, x, is shown in Figure 3.4 as a function of N_2O flow rate with different amount of He dilution. The composition of oxynitride pseudobinary alloy was well controlled by adjusting the flow ratio of 1% N_2O in N_2 and N_2 gases with wide composition range. He dilution effect was also studied. It is important to note that the concentration of Si_3N_4 decreases while the partial pressure of N_2 increases. This counter-intuitive result is due to the deactivation of N_2 in plasma. Metastable nitrogen from the glow discharge survive longer with large amount of inert gas flow and small flows of N_2 than in pure N_2. The quenching rate constant of metastable nitrogen by pure N_2 is at least two orders of magnitude larger than that by Ar and He.[10] The decrease of Si_3N_4 concentration in film is due to the de-excitation of nitrogen in high N_2 partial pressure since Si_3N_4 is formed by the reaction of SiH_4 and metastable nitrogen on surface. The de-excitation of metastable nitrogen was analyzed by optical emission spectroscopy with varying amount He diluent gas flow.[11] Figure 3.5 shows the He dilution effect. 1% N_2O in N_2 and He gas mixture were used for oxynitride film deposition. The increase of He dilution results in the decrease of N-KLL feature which means that the decrease of Si_3N_4 concentration in film (Figure 3.5 (a)). When the amount of N_2 flow is lower than that of inert gas flow, the dilution effect is obvious and the Si_3N_4 concentration can be easily controlled by adjusting the inert gas flow (Figure 3.5 (b)).

3.5.2 Hf silicate

Hf silicate $[(HfO_2)_X(SiO_2)_{1-X}]$ films are deposited on Si (100) substrate. The Si source gas, 2% SiH_4 in He 0 ~ 10 sccm is flowed through one of the shower head rings in the reactor. Hf source gas is $Hf(O^tBu)_4$ delivered by 15 sccm He carrier gas and the flow rate is controlled by a

closed loop controller monitoring an absolute Baratron and operating a needle valve (Figure 3.2). Oxygen was used for oxidation gas. The other process conditions were the same as with the Si oxynitride deposition process.

Pseudo-binary $(HfO_2)_X(SiO_2)_{1-X}$ alloy composition, x, was determined by on-line AES. The AES data were calibrated by Rutherford backscattering spectrometry (RBS) which was previously done by Hong.[12] Figure 3.6 shows the AES derivative spectra of $(HfO_2)_X(SiO_2)_{1-X}$ alloys with their end members. Decrease of x in $(HfO_2)_X(SiO_2)_{1-X}$ is characterized by the gradual decrease of the Hf-NVV peak and the concomitant increase of the Si-LVV peak. Hf-NVV and O-KLL peaks were used to check the composition. Their peak-to-peak ratios of derivative AES spectrum were used to check the composition. The composition, x, in the $(HfO_2)_X(SiO_2)_{1-X}$ alloy shows a linear relationship with peak-to-peak ratios of Hf-NVV and O-KLL features. (Figure 3.7)

3.5.3. Hf-Si oxynitride

In this research, Hf-Si oxynitride alloys are also deposited by using a remote plasma enhanced-metal organic chemical vapor deposition (RPE-MOCVD) process. Many research groups have studied Hf-Si oxynitride films using various deposition techniques such as thermal nitridation,[4, 13-17] plasma nitridation,[18-22] oxidation,[23, 24] and reactive sputtering,[25-27] etc. However, these methods have a problem forming make undesirable bonding in the Hf-Si oxynitride alloys, and this will be discussed later.

Hf-Si oxynitride alloys were deposited by a remote plasma-enhanced chemical vapor deposition (RPECVD) system using the combination of the process conditions for Si oxynitride and Hf-silicate alloys.

The N-KLL, O-KLL, and Hf-NVV intensities measured by on-line AES spectra shown in Figure 3.8 (a) were used to calculate the composition parameters, x, y and z in Hf-Si oxynitride alloys $[(Si_3N_4)_x(SiO_2)_y(HfO_2)_z$ $(x+y+z=1)]$.[9, 12] The compositions of each of the Hf-Si oxynitride alloys are shown in Figure 3.8(b) of the ternary composition diagram.

Figure 3.9 shows the trend of the composition of Hf-Si oxynitride alloys with different amount of He dilution gas. The increase of He dilution results in the decrease of Si_3N_4 incorporation in Hf-Si oxynitride alloys. This agrees well with the result of RPECVD process for silicon oxynitride alloys using N_2 / N_2O gas mixture. Within the fixed He dilution level, the composition of Si_3N_4 increases with increasing N_2 / (N_2 + N_2O) ratio, and the changes of the ratio between SiO_2 and HfO_2 were relatively small. The composition of Hf-Si oxynitride alloys can be tuned by controlling the N_2 / (N_2 + N_2O) ratio, Hf source flow rate, and the amount of He dilution.

3.6. References

1. Yasuda, T.; Ma, Y.; Habermehl, S.; Lucovsky, G., *Journal of Vacuum Science & Technology B* **1992,** 10, 1844-1851.

2. Lee, D. R.; Lucovsky, G., *Journal of Vacuum Science & Technology a-Vacuum Surfaces and Films* **1995,** 13, 1671-1675.

3. Hersee, S. D.; Ballingall, J. M., *Journal of Vacuum Science & Technology a-Vacuum Surfaces and Films* **1990,** 8, 800-804.

4. Akbar, M. S.; Gopalan, S.; Cho, H. J.; Onishi, K.; Choi, R.; Nieh, R.; Kang, C. S.; Kim, Y. H.; Han, J.; Krishnan, S.; Lee, J. C., *Applied Physics Letters* **2003,** 82, 1757-1759.

5. http://www.strem.com/code/datasheets/725800.pdf.

6. Ma, Y.; Yasuda, T.; Lucovsky, G., *Journal of Vacuum Science & Technology B* **1993,** 11, 1533-1540.

7. Briggs, D.; Seah, M. P., *PRACTICAL SURFACE ANALYSIS by Auger and X-ray Photoelectron Spectroscopy* John Wiley & Sons Ltd.: Chichester, 1984.

8. *Handbook of Auger Electron Spectroscopy*. Physical Electronics, Inc: Eden Prairie, 1995.

9. Hattangady, S. V.; Niimi, H.; Lucovsky, G., *Journal of Vacuum Science & Technology a-Vacuum Surfaces and Films* **1996,** 14, 3017-3023.

10. Lin, C. L.; Kaufman, F., *Journal of Chemical Physics* **1971,** 55, 3760-3770.

11. Tsu, D. V.; Parsons, G. N.; Lucovsky, G., *Journal of Vacuum Science & Technology a-Vacuum Surfaces and Films* **1988,** 6, 1849-1854.

12. Hong, J. G. Thesis. North Carolina State University, Raleigh, 2003.

13. Cho, H. J.; Lee, H. L.; Park, H. B.; Jeon, T. S.; Park, S. G.; Jin, B. J.; Kang, S. B.; Shin, Y. G.; Chung, U. I.; Moon, J. T., *Japanese Journal of Applied Physics Part 1-Regular Papers Brief Communications & Review Papers* **2005,** 44, 2230-2234.

14. Cho, M. H.; Chung, K. B.; Ko, D. H., *Applied Physics Letters* **2006,** 89, -.

15. Chung, K. B.; Whang, C. N.; Cho, M. H.; Yim, C. J.; Ko, D. H., *Applied Physics Letters* **2006,** 88, -.

16. Ganem, J. J.; Trimaille, I.; Vickridge, I. C.; Gusev, E. P., *Nuclear Instruments & Methods in Physics Research Section B-Beam Interactions with Materials and Atoms* **2006,** 249, 517-522.

17. Ikarashi, N.; Watanabe, K.; Masuzaki, K.; Nakagawa, T.; Miyamura, M., *Journal of Applied Physics* **2006,** 100, -.

18. Inumiya, S.; Miura, T.; Shirai, K.; Matsuki, T.; Torii, K.; Nara, Y., *Japanese Journal of Applied Physics Part 1-Regular Papers Brief Communications & Review Papers* **2006,** 45, 2898-2902.

19. Oshima, M.; Takahashi, H.; Okabayashi, J.; Toyoda, S.; Kumigashira, H.; Inoue, M.; Mizutani, M.; Yugami, J., *Journal of Applied Physics* **2006,** 100, -.

20. Quevedo-Lopez, M. A.; Chambers, J. J.; Visokay, M. R.; Shanware, A.; Colombo, L., *Applied Physics Letters* **2005,** 87, -.

21. Sayan, S.; Nguyen, N. V.; Ehrstein, J.; Chambers, J. J.; Visokay, M. R.; Quevedo-Lopez, M. A.; Colombo, L.; Yoder, D.; Levin, I.; Fischer, D. A.; Paunescu, M.; Celik, O.; Garfunkel, E., *Applied Physics Letters* **2005,** 87, -.

22. Toyoda, S.; Okabayashi, J.; Takahashi, H.; Oshima, M.; Lee, D. I.; Sun, S.; Sun, S.; Pianetta, P. A.; Ando, T.; Fukuda, S., *Applied Physics Letters* **2005,** 87, -.

23. Pant, G.; Punchaipetch, P.; Kim, M. J.; Wallace, R. M.; Gnade, B. E., *Thin Solid Films* **2004,** 460, 242-246.

24. Yamaguchi, M.; Sakoda, T.; Minakata, H.; Xiao, S. Q.; Morisaki, Y.; Ikeda, K.; Mishima, Y., *Ieee Transactions on Electron Devices* **2006,** 53, 923-925.

25. Kamimuta, Y.; Koike, M.; Ino, T.; Suzuki, M.; Koyama, M.; Tsunashima, Y.; Nishiyama, A., *Japanese Journal of Applied Physics Part 1-Regular Papers Short Notes & Review Papers* **2005,** 44, 1301-1305.

26. Koike, M.; Ino, T.; Kamimuta, Y.; Koyama, M.; Kamata, Y.; Suzuki, M.; Mitani, Y.; Nishiyama, A., *Physical Review B* **2006,** 73, -.

27. Quevedo-Lopez, M. A.; El-Bouanani, M.; Kim, M. J.; Gnade, B. E.; Wallace, R. M.; Visokay, M. R.; LiFatou, A.; Chambers, J. J.; Colombo, L., *Applied Physics Letters* **2003,** 83, 1679-1679.

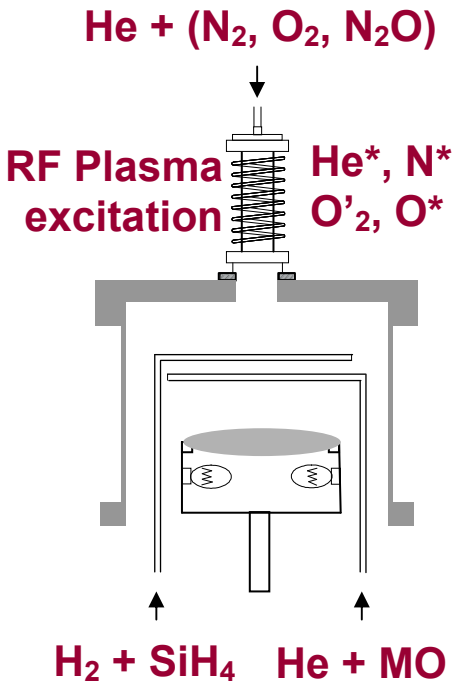

Figure 3.1. Schematic of Remote Plasma Enhanced MOCVD Reactor.

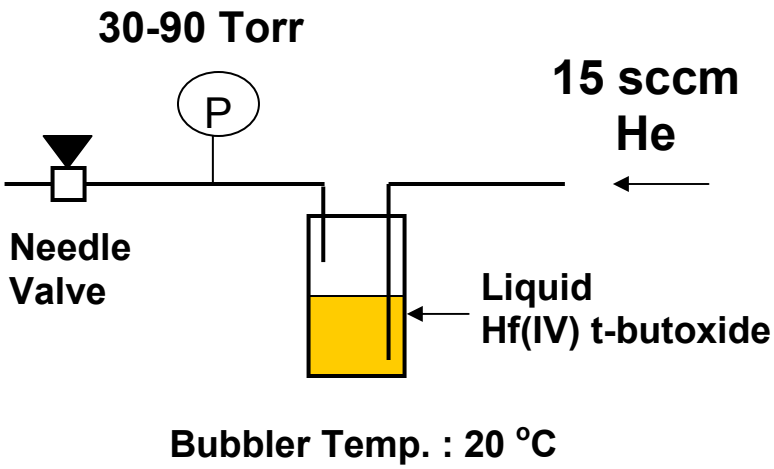

Figure 3.2. Schematic of the Hf source gas delivery system. He carrier gas at 15 sccm is flowed through the bubbler and the flow is controlled by using feedback from a pressure transducer.

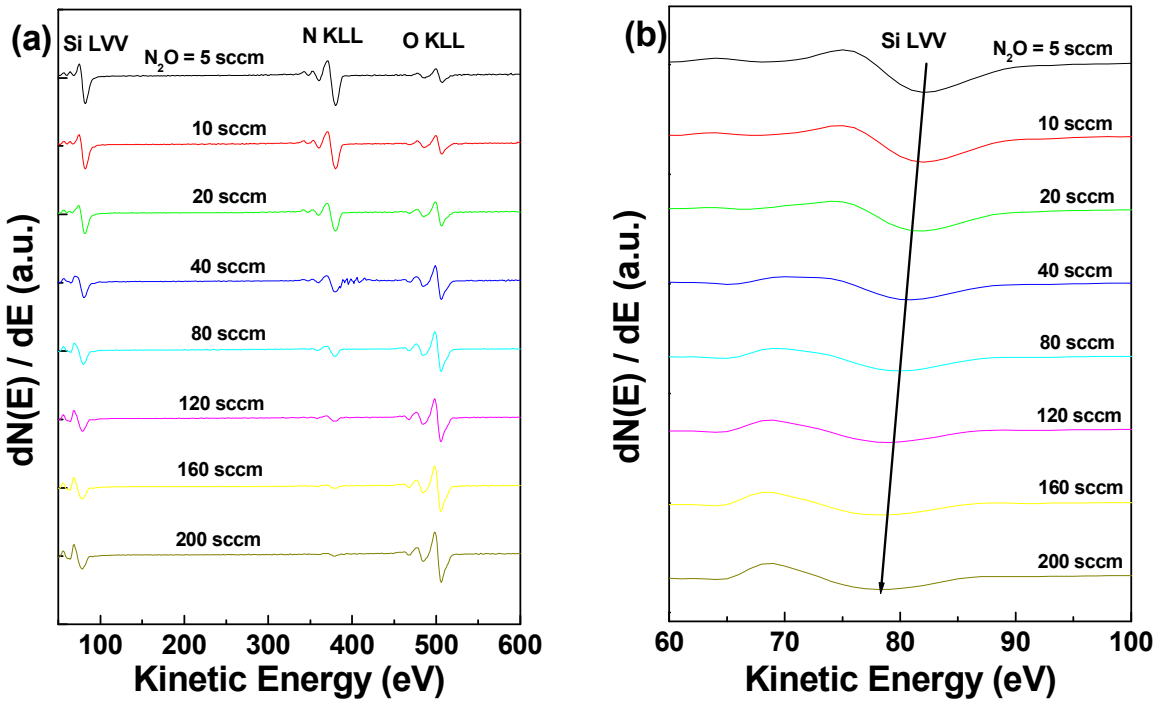

Figure 3.3. On-line AES derivative spectra from Si oxynitride films with varying N_2O flow rate, the (N_2 + N_2O) flow rate was fixed at 200 sccm and He 50 sccm,

(a) Si-LVV, N-KLL, and O-KLL features.

(b) nitride and oxide characteristics of Si-LVV with respect to the N_2O flow rate.

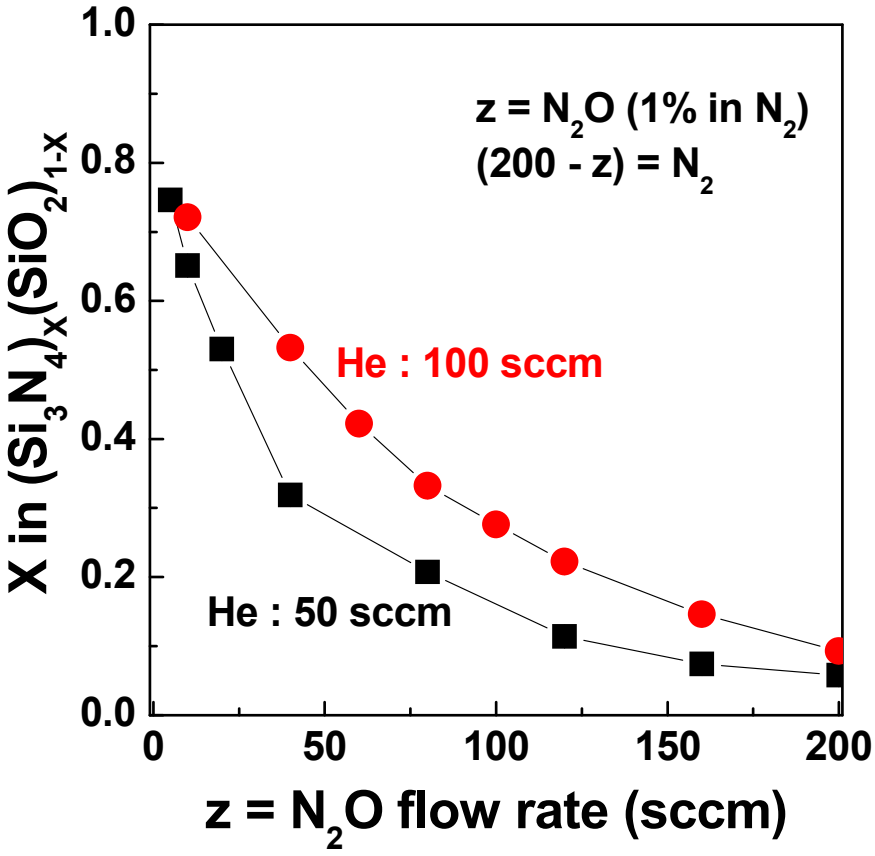

Figure 3.4. Composition of oxynitride films as a function of N_2O in N_2 flow and He dilution.

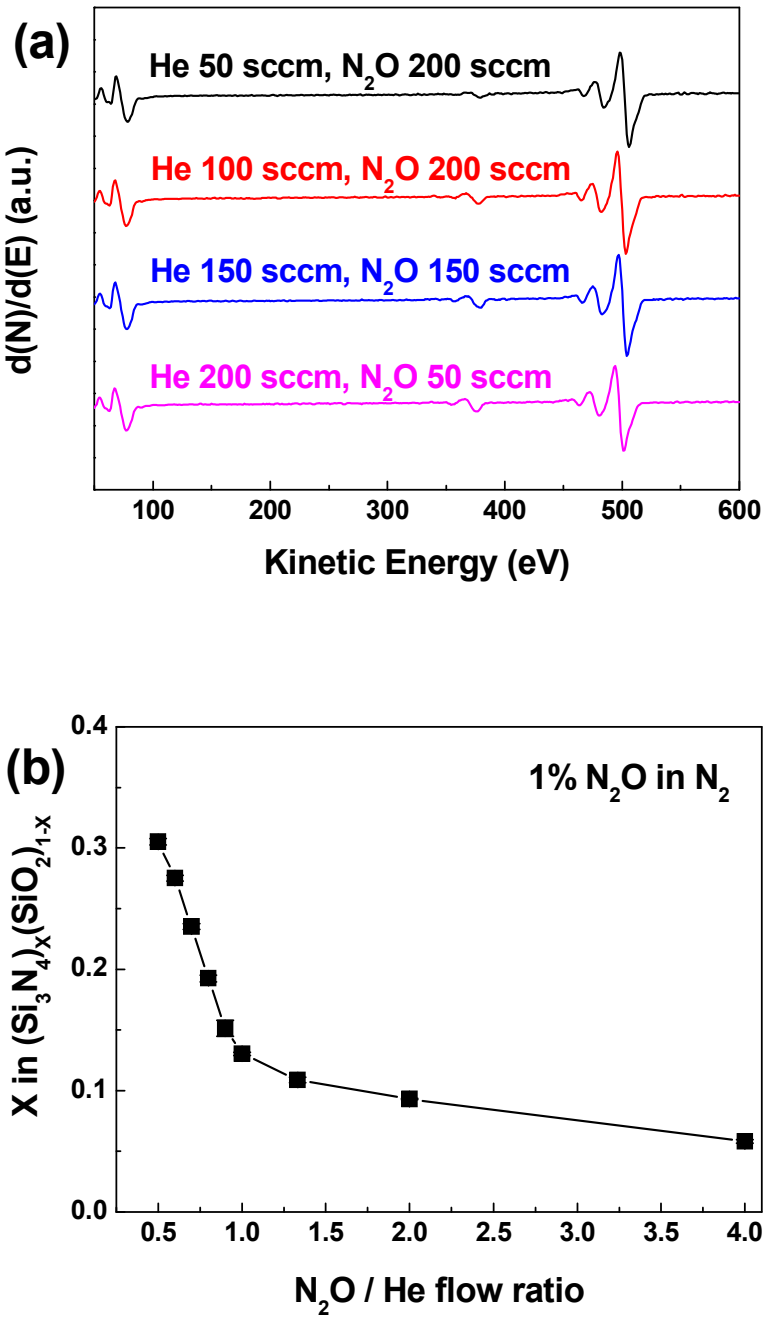

Figure 3.5. The effect of He dilution gas,

(a) On-line AES derivative spectra from silicon oxynitride films with varying N_2O/He flow ratio.

(b) the composition of silicon oxynitride alloys with varying N_2O/He flow ratio.

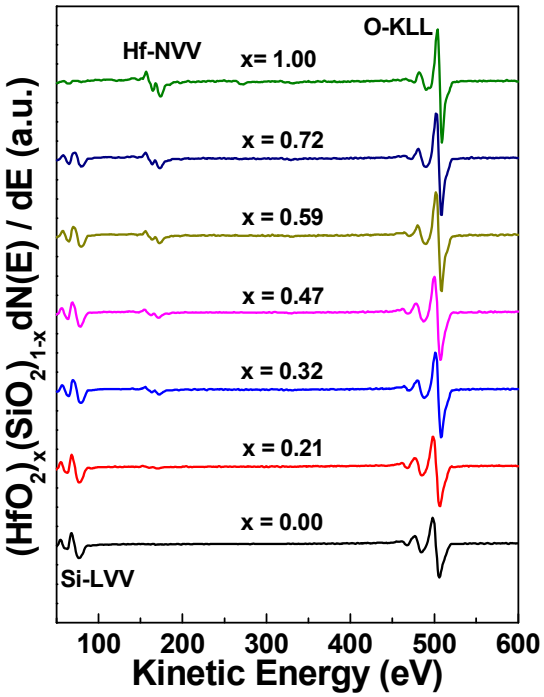

Figure 3.6. On-line AES derivative spectra for the $(HfO_2)_X(SiO_2)_{1-X}$ alloys with the range of from HfO_2 to SiO_2.

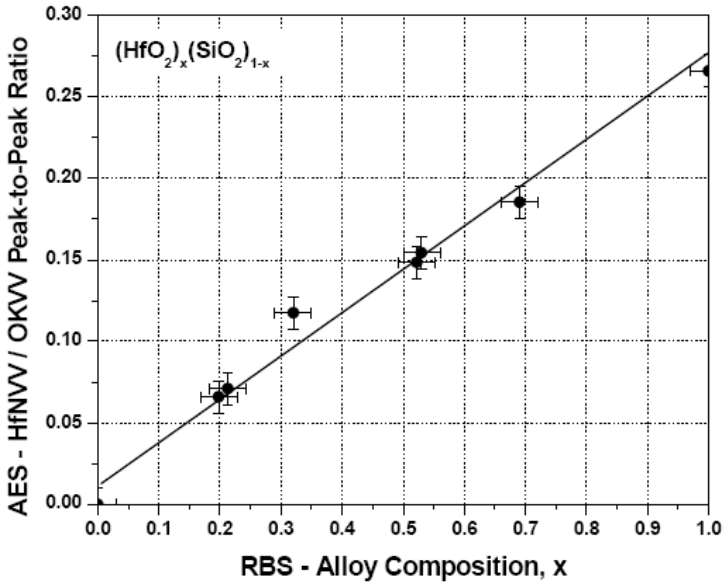

Figure 3.7. RBS-AES calibration for $(HfO_2)_x(SiO_2)_{1-x}$ composition.[104]

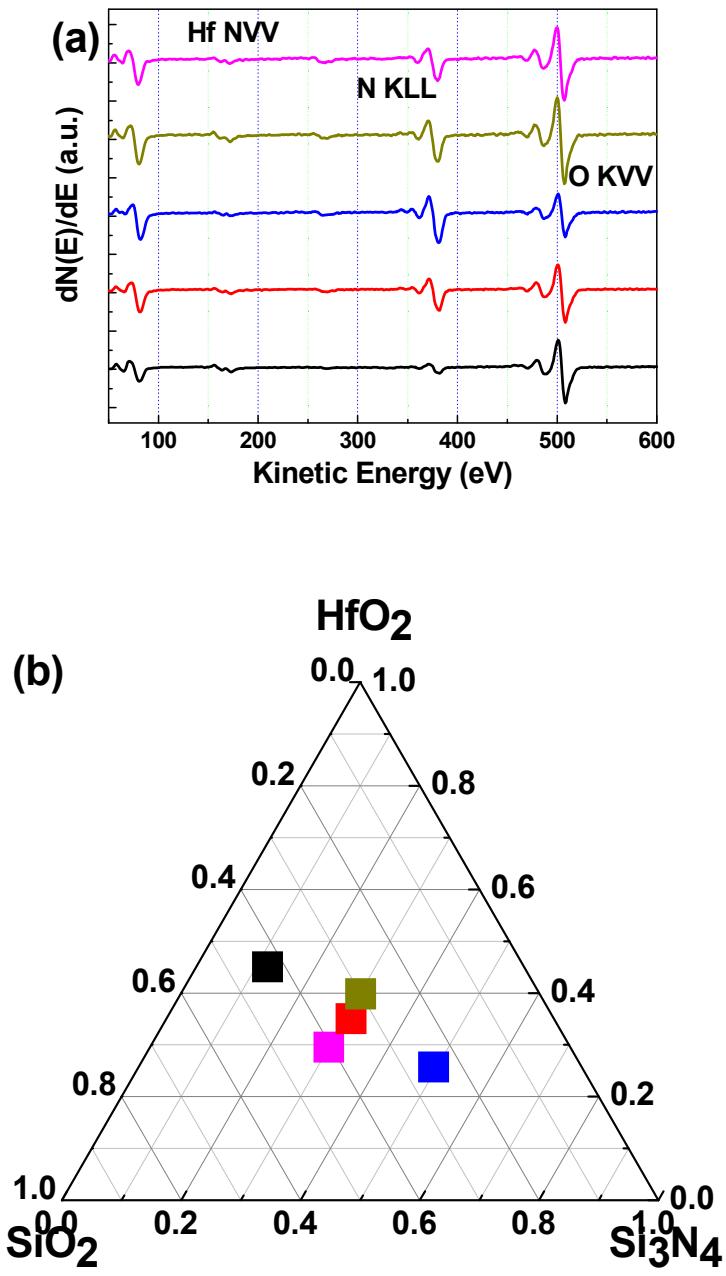

Figure 3.8. (a) On-line AES derivative spectra for Hf-Si oxynitride alloys. (b) Ternary composition diagram of Hf-Si oxynitride alloys. The composition was calculated from N-KLL, O-KLL, and Hf-NVV intensities measured by on-line AES spectra.

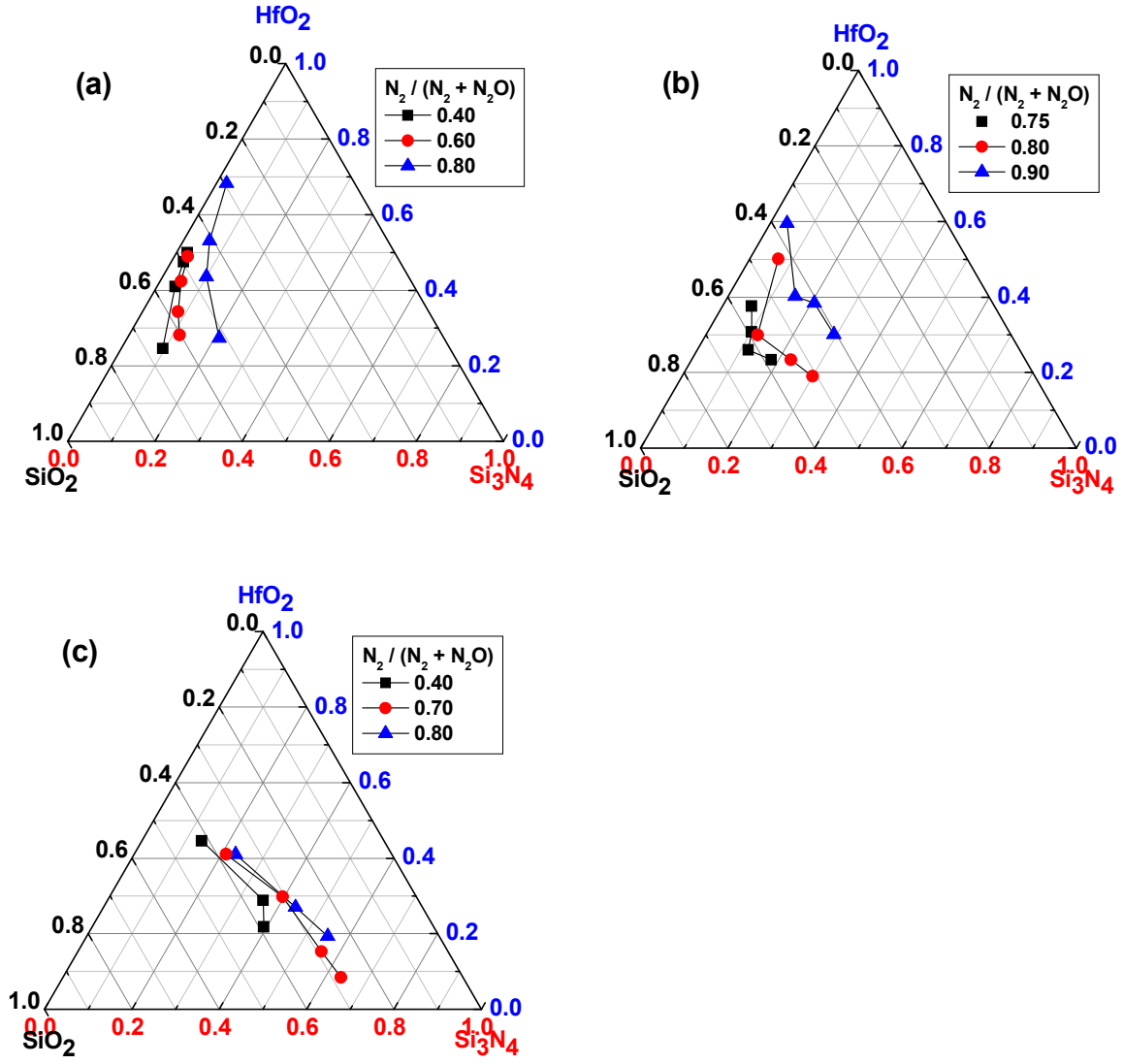

Figure 3.9. Ternary composition diagrams of Hf-Si oxynitride alloys with the amount of He dilution. (a) He 50 sccm. (b) He 100 sccm. (c) He 200 sccm.

Chapter 4. Spectroscopic Investigation of Chemical phase separation in Hf silicate and Hf-Si oxynitride alloys using FTIR and XPS.

4.1. Introduction

Recently, transition metal (TM) silicates were identified as attractive candidates since they have high dielectric constants to reduce the leakage current and are thermodynamically stable in contact with Si substrate. Although the dielectric constants of TM silicate films are smaller than those of metal oxides, silicate films are thermally more stable on the Si substrate.

However, the significant limitation for the integration of TM silicate alloys such as $(ZrO_2)_x(SiO_2)_{1-x}$ and $(HfO_2)_x(SiO_2)_{1-x}$ as gate dielectrics into advanced Si devices is a chemical phase separation of these pseudo-binary alloys into SiO_2 and transition metal oxides, $Zr(Hf)O_2$ for Zr(Hf) silicate alloys.[1, 2] This problem caused not only the leakage current increase through the grain boundary and roughness of the film surface, but also further degradation of the gate capacitance required for device scaling.[3] Chemical phase separation and crystallization often occurred when Zr(Hf) silicates were annealed in the same regime of temperatures required for integration processing of devices with deposited dielectrics.[4, 5]

It has recently been reported that the N incorporation into the Hf-silicate also suppress crystallization.[6, 7] The incorporation of N is also useful to prevent interfacial reaction between dielectric films and the Si substrate and boron penetration from the boron doped polysilicon gate electrodes layer.[8]

This chapter presents the results of an investigation by FTIR and XPS on the pseudo-binary Hf silicate and the pseudo-ternary Hf-Si oxynitride alloys deposited on Si-substrates by

RPE-MOCVD. The effects of the alloy composition and post-deposition annealing temperatures on the local bonding structures of the alloys are studied. The information about chemical phase separation in the alloys is supported by FTIR and XPS analysis.

4.2. FTIR Analysis

When the IR beam transmits through the sample, the spectrum includes the information of the sample as well as the background. To eliminate these contributions, the sample single beam spectrum must be ratioed against the background spectrum. This produces a transmittance spectrum by the following equation:

$$T = I / I_0 \qquad \text{(Eqn.4.1)}$$

where T is transmittance, I is the intensity measured with a sample in the beam (from the sample single beam spectrum), and I_0 is the intensity measured with no sample in the beam (from the background spectrum). The absorbance spectrum can be calculated from the transmittance spectrum using the Beer's law:[1]

$$A = - \ln T \qquad \text{(Eqn.4.2)}$$

where A is absorbance. Then for the film/substrate system in Figure 4.1, Eqn. 4.3 becomes:

$$A = A_f + A_s = \alpha x = \ln(I_0 / I) \qquad \text{(Eqn.4.3)}$$

where x is the sample thickness, α is the absorption coefficient, A_f and A_s are the absorbance's of the film and substrate, respectively. The absorption spectrum of the film can be obtained by subtracting the reference spectrum of the substrate from the absorption spectrum of the film/substrate system (Figure 4.2).

4.2.1. Experiments

IR absorption measurements, in the mid-IR (4000 ~ 400 cm^{-1}) and far-IR (700 ~ 50 cm^{-1}) regions of the electromagnetic spectrum, were performed with a Nicolet Magna-FTIR 750 spectrometer. N_2 gas purged the spectrometer continuously to minimize absorption from IR active components present in the atmosphere, e.g., H_2O and CO_2. The spectrometer utilizes a He/Ne laser for optical bench alignment prior to all data collection. The mid-IR measurements utilized a DTGS detector (with a KBr window) and a KBr beam splitter; the far-IR measurements a DTGS detector (with a polyethylene window) and a Si-substrate beam splitter. Films were deposited on high resistivity (15 ~ 50 Ω) Si-substrates to minimize absorption by free charge carriers. Double side polished wafers were used as a substrate to maximize IR transmission and minimize multiple internal reflections. A bare Si-substrate, from the same wafer used in the deposition process, was used for substrate subtraction. The reference samples were treated in a H_2O/HF (100:1) solution, as described in section 3.1, prior to IR measurements. Film thickness was greater than approximately 1500 Å thick for good IR absorption sensitivity.

4.2.2. Results : FTIR Analysis

IR absorption spectra of as deposited alloys were shown in Figure 4.3. Three main peaks (stretching 1076 cm^{-1}, bending 814 cm^{-1}, and rocking mode 455 cm^{-1})[2, 3] of a-SiO_2 are observed in Figure 4.3(a). The main peak of Si_3N_4 stretching is around 890 cm^{-1}. The main peak of Si oxynitride is located between SiO_2 stretching and Si_3N_4 stretching around 920 cm^{-1}. There is a continuous change from a SiO_2-like to Si_3N_4-like feature. The single feature of Si oxynitride confirms that the material is a homogeneous alloy of SiO_2 and Si_3N_4. Hf silicate alloys with 10 ~

30 % HfO_2 concentration have the spectra features related to the characteristic of SiO_2 (Figure 4.3(b)). As HfO_2 concentration increases, the intensity of the three main peaks of SiO_2 decrease and a shoulder around 970 cm^{-1} on the low wavenumber side of the stretching peak is observed. This indicates that Si-O-Si bonding decreases and Si-O-Hf bonding increases with increasing HfO_2 concentration. As deposited Hf-Si oxynitride alloys show single features with various compositions. The main stretching peak moves to Si_3N_4-like feature with increasing N incorporation (Figure 4.3(c)).

Thermal stability of Hf silicate alloys was investigated. Films were annealed ex-situ in an inert Ar ambient atmosphere for 1 min at 900, 1000, and 1100℃, respectively. IR absorption spectra of $(HfO_2)_X(SiO_2)_{1-X}$ alloys with x = 0.10, 0.20, and 0.30 are shown in Figure 4.4. Small changes in IR absorption are observed following anneals indicating no significant changes in structure. The stretching peaks shift to the higher wavenumber side due to relaxation of the SiO_2 network after anneal. The amount of peak shifting increases with increasing HfO_2 concentration by 11 cm^{-1} for x = 0.10, 23 cm^{-1} for x = 0.2, and 27 cm^{-1} for x = 0.3, respectively. For 0.30 HfO_2 alloy, the changes in spectra are more obvious in Figure 4.4(d). As anneal temperature increases, the stretching peak intensity increases and the intensity around 970 cm^{-1} associated Si–O–Hf bonding decreases. This indicates that Si-O-Hf bonding arrangements transform to Si–O–Si bonds (characteristic of SiO_2) and Hf-O-Hf bonding (characteristic of the HfO_2), i.e. chemical phase separation into SiO_2 and HfO_2.

IR absorption spectra of Hf-Si oxynitride alloys, $[(Si_3N_4)_x(SiO_2)_{0.5\cdot(1-x)}(HfO_2)_{0.5\cdot(1-x)}]$, were shown in Figure 4.5. The ratio of SiO_2 : HfO_2 was fixed at 1:1, and x, the Si_3N_4 concentration changed from 0.07 to 0.49. As anneal temperature increases, the stretching peak shifts to the

higher wavenumber side and the intensities of the stretching and rocking mode peaks increase for the alloys with low Si_3N_4 concentration. The amount of changes in IR spectra reduces when Si_3N_4 concentration increases from 0.07 to 0.17. However, the IR absorption spectra of the alloys with Si_3N_4 concentration of x = 0.33 and 0.49 shows no change with anneal.

4.3. XPS Analysis

X-ray photoelectron spectroscopy (XPS), is also known as electron spectroscopy for chemical analysis (ESCA). Electrons can be emitted from any orbital with photoemission occurring for X-ray energies exceeding the binding energy. XPS is a surface-sensitive method because the emitted photoelectrons originate from the upper 0.5-5 nm of the sample, like Auger electrons. The major use of XPS is for identification of compounds using energy shifts due to changes in the chemical structure of the sample atoms. For example, an oxide exhibits a different spectrum than a pure element.[4, 5]

4.3.1. Experiments

Films approximately 100–150 Å thick were deposited at 300°C on high conductivity (0.02–0.05 Ω-cm) p-type Si(100) substrates. This range of film thickness was chosen to exclude any contribution to XPS core-level binding energy and Auger electron kinetic energy from the Si-substrate interface region. Substrates were initially treated in a H_2O/HF (100:1) solution, as described in section 3.1. Prior to Hf silicate and Hf-Si oxynitride alloys deposition, an a-SiO_2 layer approximately 50 Å thick was plasma-deposited on the Si-substrate to provide a chemical buffer layer between the alloys and the Si-substrate. The chemical buffer layer was used in order

to suppress Hf source gas reactions with the Si substrate during film deposition and prevent reactions between the alloys and the Si-substrate during post-deposition annealing. XPS measurements of Si2p, Hf4f, N1s and O1s core-levels were made offline using a Riber LAS-3000 spectrometer with non-monochromatic Mg Kα radiation (1253.6 eV) and pass energy of 20 eV. The spectral resolution was approximately 1 eV. The system base pressure for XPS measurements was approximately $3x10^{-10}$ Torr. Data were corrected for charging effects using the C-1s peak at 284.6 eV from adventitious carbon contamination on the film surface. The error range of measuring peak spectral positions was found to be < 0.2 eV.

4.3.2. Results : XPS Analysis

XPS core-level Si2p and Hf4f spectra of $(HfO_2)_X(SiO_2)_{1-X}$ (x = 0.2 and 0.4) and $(Si_3N_4)_x(SiO_2)_{0.5\cdot(1-x)}(HfO_2)_{0.5\cdot(1-x)}$ (x = 0.13, 0.33, and 0.50) annealed at 900 ℃ and 1100℃ are shown in Figures 4.6 and 4.7. The Si2p features show no significant asymmetries or multiple features after anneal in all alloys. The Si2p and Hf4f chemical shift of as-deposited $(HfO_2)_X(SiO_2)_{1-X}$ alloys to the lower energy side was observed as x increases. This corresponds to previous work.[6, 7] The increase of Si-N bonding character of $(Si_3N_4)_x(SiO_2)_{0.5\cdot(1-x)}(HfO_2)_{0.5\cdot(1-x)}$ alloys with increasing x was observed as x increases. The details of XPS chemical shifts will be discussed in the next section.

Changes in Hf4f features of $(HfO_2)_X(SiO_2)_{1-X}$ and $(Si_3N_4)_x(SiO_2)_{0.5\cdot(1-x)}(HfO_2)_{0.5\cdot(1-x)}$ with x = 0.13 are shown in Figure 4.7. $Hf4f_{7/2}$ and $4f_{5/2}$ are distinguished more obviously with annealing temperature and HfO_2 concentration. This implies some change in phase of the alloys.[8] However, $(Si_3N_4)_x(SiO_2)_{0.5\cdot(1-x)}(HfO_2)_{0.5\cdot(1-x)}$ (x =0.33, and 0.50) show no change in Hf4f features.

There is no evidence of Hf-Si bonding in $(HfO_2)_X(SiO_2)_{1-X}$ and $(Si_3N_4)_x(SiO_2)_{0.5\cdot(1-x)}(HfO_2)_{0.5\cdot(1-x)}$ alloys.

XPS core-level N1s spectra of $(Si_3N_4)_x(SiO_2)_{0.5\cdot(1-x)}(HfO_2)_{0.5\cdot(1-x)}$ (x = 0.13, 0.33, and 0.50) annealed at 900 ℃ and 1100℃ are shown in Figure 4.8. The N1s features maintain a single feature after anneal in all alloys. There is no evidence of Hf-N or O-N bonding.

XPS core-level O1s spectra of $(HfO_2)_X(SiO_2)_{1-X}$ alloys with x = 0.20 and 0.40 annealed at 900°C and 1100 °C for 60s, and the associated derivative spectra, are shown in Figure 4.9(a) and (b), respectively. The O1s spectra in Figure 4.9 were fit using a two component Gaussian model. Asymmetries and two features of the O1s spectra were observed with increasing annealing temperatures and HfO_2 concentration. These are more obvious with the associated derivative spectra.

XPS core-level O1s spectra of $(Si_3N_4)_x(SiO_2)_{0.5\cdot(1-x)}(HfO_2)_{0.5\cdot(1-x)}$ alloys with x = 0.13, 0.33 and 0.50 annealed at 900°C and 1100 °C for 60s, and the associated derivative spectra, are shown in Figure 4.10 (a), (b), and (c), respectively. $(Si_3N_4)_x(SiO_2)_{0.5\cdot(1-x)}(HfO_2)_{0.5\cdot(1-x)}$ alloys with x = 0.13 shows similar trend with annealing temperatures with Hf silicate alloys. However, no additional feature evolution is observed in $(Si_3N_4)_x(SiO_2)_{0.5\cdot(1-x)}(HfO_2)_{0.5\cdot(1-x)}$ alloys with x = 0.33 and 0.50 with annealing temperatures.

4.4. Discussion

4.4.1. The Pseudo-binary (or ternary) alloys

$(HfO_2)_X(SiO_2)_{1-X}$ and $(Si_3N_4)_x(SiO_2)_{0.5\cdot(1-x)}(HfO_2)_{0.5\cdot(1-x)}$ alloys were deposited as pseudo-binary (and ternary) alloys. As deposited alloys show single feature in FTIR spectra (Figure 4.4

and 4.5). There is no evidence of metallic Hf-Si, Hf-N, Hf-Hf, or Si-Si bonding in XPS core-level spectra (Figure 4.6, 4.7, and 4.8). It is considered that the alloys are single phase materials and the local bonding structures in the alloys are the same as those of the end-member compounds. The pseudo-binary alloys such as $(HfO_2)_X(SiO_2)_{1-X}$ and $(ZrO_2)_X(SiO_2)_{1-X}$ have been studied to combine the desirable properties from two different oxides while eliminating the undesirable properties of each individual material.[9] The pseudo-binary Hf silicate alloys can be easily fabricated in comparison with Hf-Si oxynitride deposition. However, N incorporation into the Hf silicate alloys is rather complex. Various deposition techniques such as thermal nitridation,[10-15] plasma nitridation,[16-20] oxidation,[21, 22] and reactive sputtering[23-26] have been used for the deposition of Hf-Si oxynitride alloys. However, these methods have problems of forming undesirable Hf-N bonding[10, 16, 21, 24, 25, 27-29] or non-uniform N incorporation[30-33] in the Hf-Si oxynitride alloys. There is also risk of film crystallization during annealing at high temperatures or substrate damage from the use of plasma. Since the existence of Hf-N bonding can degrade the electrical properties such as leakage current[27, 34, 35] and band gap narrowing,[19, 24, 36] it is important to fabricate Hf-Si oxynitride alloys without Hf-N bond. However, direct growth of Hf-Si oxynitride using RPE-MOCVD in this report has the advantages of: i) no need of extra process for N incorporation, ii) free from Hf-N metallic bond, iii) deposition at low temperature, and iv) easy tuning of film composition.

4.4.2. XPS Chemical Shifts: Charge-Potential Model

The measured XPS binding energy of an x-ray photoelectron from an atom A, $E_{B(A)}$, is related to its measured kinetic energy, EK(A), in the following way:

$$E_B(A) = h\nu - E_K(A) - \phi_s \qquad \text{Eqn.4.4}$$

where $h\nu$ is the incident x-ray photon energy, and ϕ_s is the spectrometer work function.[4]

Core-electron binding energy measured by XPS is not equivalent to the electron orbital energy, since final-state (or relaxation) effects must be taken into account. For an isolated atom, the measured XPS core-level electron binding energy is shifted, by the measurement itself, from the pre-measurement (initial) state value of the system. These shifts are labeled as relaxations, and reflect the adjustments of the final state effects. So core level binding energies can be expressed as a reflection of both their initial state value and relaxation features induced by the measurement itself as follows:

$$E_B(A) = \left| E(A) \right| - E_{fs}(A) \qquad \text{Eqn.4.5}$$

where E(A) is the electron orbital energy of A element and $E_{fs}(A)$ represents its atomic final-state (or relaxation) effects. The photoelectron in an N-electron system is ejected without further energy loss in the sample, and the remnant N-1 electron system goes into the lowest-energy final state (the relaxed state). This relaxation process always acts to reduce the binding energy, so $E_{fs}(A)$ are positive.[37] The atomic relaxation can be separated into three parts, for orbitals with quantum number n', representing inner-shell (n' < n), intra-shell (or intra-atomic, n' = n), and outer-shell (extra-atomic, n' > n) relaxation. Inner- and intra- terms are small and may be ignored. Since the relaxation part depends on the characteristics of the non-A species that surround the A atom, the final-state effects can be regarded as extra-atomic relaxation.[37, 38]

In order to interpret the chemical shift in core-level electron binding energy between an atom in a molecule and the same atom in a reference system, K. Siegbahn developed the charge

potential model which illustrates the physical background of the chemical shift effect.[39] The charge potential model of Ref. 11 has been generalized to describe the chemical shift of an atom A in two different bonding environments,[5] and for estimating the chemical shift in core-level electron binding energy, $\Delta E_B(A)$, between a free atom A, and atom A in an oxide the charge-potential model becomes:

$$\Delta E_B(A) = k_A \delta_A + V_A + E_{fs}(A) \qquad \text{Eqn.4.6}$$

The first term on the right, $k_A\delta_A$, represents charge transfer as a result of chemical bonding in the oxide, where δ_A is the net partial charge on atom A and k_A is a positive constant which represents changes in core-level electron binding energy as a result of changes in the valence shell of atom A in forming the oxide. The energy V_A ($V_A = -\Sigma_{B\neq A}\delta_B / r_{A-B}$) represents the interatomic effective potential between atom A and the other ionic cores in the oxide, and can be obtained by using the Madelung constant.[6, 40] The term $E_{fs}(A)$ represents changes in final-state effects between the free atom and the atom in the oxide that arise from the charge rearrangement or relaxation. For an atom A in two different oxides,[6] Eqn.4.6 becomes

$$\Delta E_B(A) = k_A \Delta\delta_A + \Delta V_A + \Delta E_{fs}(A) \qquad \text{Eqn.4.7}$$

and Δ reflects the composition change in compounds. For pseudo-binary $(HfO_2)_X(SiO_2)_{1-X}$ alloys, the terms on the right of Eqn.4.7 represent changes in Hf, Si and O core-level binding energies as a result of (i) charge transfer, $k_A\Delta\delta_A$, (ii) changes in the coulomb interaction energy, ΔV_A, and (iii) changes in final-state effects, $\Delta E_{fs}(A)$, as a function of alloy composition, x. The term ΔV_A is also proportional to δ_A so that ($k_A\Delta\delta_A + \Delta V_A$) can be modified to $k'_A\Delta\delta_A$,[40] and the final-state (or relaxation) effects are able to be ignored in some cases.[38] According to the research by T.L. Barr et.al., the measured binding energy shifts are directly related to differences in initial state

chemistry. There are no significant contribution of final-state effect changes in the network forming oxides like zeolites and silicates.[38] Then, Eqn.4.7 becomes

$$\Delta E_B(A) = k_A \Delta \delta_A \qquad \text{Eqn.4.8}$$

Note that chemical shifts, $\Delta E_B(A)$, with alloy composition, according to Eqn.4.8, are linearly proportional to changes in partial charge, $\Delta \delta_A$.

4.4.3. Chemical Phase Separation

The pseudo-binary alloys and the pseudo-ternary alloys with low Si_3N_4 concentration (x = 0.07 and 0.17) show changes in FTIR absorption spectra after anneal at 900 ~ 1100℃ 60s, in Ar. As anneal temperature increases, the intensity around 970 cm^{-1} associated Si-O-Hf bonding decreases. This indicates that Si-O-Hf bonding arrangements transform to Si-O-Si bonds (characteristic of SiO_2) and Hf-O-Hf bonding (characteristic of the HfO_2), i.e. chemical phase separation into SiO_2 and HfO_2. The increase in the intensity of the stretching peak relative to the high wavenumber shoulder, are indicative of chemical phase separation in these alloys as well. However, the pseudo-ternary $(Si_3N_4)_x(SiO_2)_{0.5\cdot(1-x)}(HfO_2)_{0.5\cdot(1-x)}$ alloys with high Si_3N_4 concentration (x = 0.33 and 0.49) show no change in FTIR spectra even after 1100℃ anneal. These alloys maintain their amorphous phase without chemical phase separation.

After 900℃ and 1100℃ 60s anneal in Ar, the two features in the XPS O1s spectra and associated first derivative spectra of pseudo-binary $(HfO_2)_X(SiO_2)_{1-X}$ alloy with x = 0.2 and 0.4 are observed (Figure 4.9). The two distinguished O1s core-levels are originated from O-atoms characteristic of (i) the HfO_2 phase, and (ii) the SiO_2 phase. This indicates chemical phase separation in the alloys. The pseudo-ternary $(Si_3N_4)_x(SiO_2)_{0.5\cdot(1-x)}(HfO_2)_{0.5\cdot(1-x)}$ alloy with x = 0.13

shows two features in the XPS O1s spectra with same anneal conditions. However, there is no evidence of multiple features in the pseudo-ternary $(Si_3N_4)_x(SiO_2)_{0.5\cdot(1-x)}(HfO_2)_{0.5\cdot(1-x)}$ alloy with x = 0.33 and 0.50. This indicates that chemical phase separation is suppressed. The results of XPS O1s spectra of the pseudo-binary $(HfO_2)_X(SiO_2)_{1-X}$ alloys and the pseudo-ternary $(Si_3N_4)_x(SiO_2)_{0.5\cdot(1-x)}(HfO_2)_{0.5\cdot(1-x)}$ alloys correspond to the results of FTIR spectra.

The role of nitrogen incorporation in suppressing chemical phase separation of the Hf-Si oxynitride alloys can be explained as follows. The structure of Si_3N_4 is more stress rigid than that of SiO_2. This means that the atomic migration of Hf and/or Si atoms needs more activation energies to overcome the connected bonding in Si_3N_4 rich ($x > \sim 0.33$) phase in Hf-Si oxynitride alloys. Figure 4.11 displays the schematic representation of local bonding arrangement of separation Hf-Si oxynitride alloys with the composition of 33~40% of Si_3N_4, 30~33% of SiO_2 and HfO_2.

Si-N_3 back-bones encapsulate Hf^{4+} ions and two Si-O^{1-} terminations and hinder chemical phase separation into SiO_2 and HfO_2. The lower Si_3N_4 content alloys display chemical phase separation into SiO_2 and HfO_2 because the Si_3N_4 content is not sufficient to isolate the Hf^{4+} ions. This is supported by results of FTIR and XPS analyses.

4.5. References

1. Maria, J. P.; Wicaksana, D.; Kingon, A. I.; Busch, B.; Schulte, H.; Garfunkel, E.; Gustafsson, T., *Journal of Applied Physics* **2001,** 90, 3476-3482.

2. Rayner, G. B.; Kang, D.; Lucovsky, G., *Journal of Vacuum Science & Technology B* **2003,** 21, 1783-1791.

3. Neumayer, D. A.; Cartier, E., *Journal of Applied Physics* **2001,** 90, 1801-1808.

4. Rayner, G. B.; Kang, D.; Hinkle, C. L.; Hong, J. G.; Lucovsky, G., *Microelectronic Engineering* **2004,** 72, 304-309.

5. Maria, J. P.; Wickaksana, D.; Parrette, J.; Kingon, A. I., *Journal of Materials Research* **2002,** 17, 1571-1579.

6. Visokay, M. R.; Chambers, J. J.; Rotondaro, A. L. P.; Shanware, A.; Colombo, L., *Applied Physics Letters* **2002,** 80, 3183-3185.

7. Bastos, K. P.; Driemeier, C.; Pezzi, R. P.; Soares, G. V.; Miotti, L.; Morais, J.; Baumvol, I. J. R.; Wallace, R. M., *Materials Science and Engineering B-Solid State Materials for Advanced Technology* **2004,** 112, 134-138.

8. Quevedo-Lopez, M. A.; El-Bouanani, M.; Kim, M. J.; Gnade, B. E.; Wallace, R. M.; Visokay, M. R.; LiFatou, A.; Chambers, J. J.; Colombo, L., *Applied Physics Letters* **2003,** 82, 4669-4671.

9. Smith, B. C., *Fundamentals of Fourier Transform Infrared Spectroscopy*. CRC Press: Boca Raton, 1996.

10. Bell, R. J.; Dean, P., *Discussions of the Faraday Society* **1971,** 1970, 55-&.

11. Galeener, F. L.; Leadbetter, A. J.; Stringfellow, M. W., *Physical Review B* **1983,** 27, 1052-1078.

12. Watts, J. F. W., J, *An introduction to surface analysis by XPS and AES*. J. Wiley: Chichester 2003.

13. Briggs, D. S., M.P., *Practical surface analysis : by auger and x-ray photo-electron spectroscopy* Wiley: Chichester, 1983.

14. Guittet, M. J.; Crocombette, J. P.; Gautier-Soyer, M., *Physical Review B* **2001,** 63, art. no.-125117.

15. Rayner, G. B.; Kang, D.; Zhang, Y.; Lucovsky, G., *Journal of Vacuum Science & Technology B* **2002,** 20, 1748-1758.

16. Cho, M. H.; Chung, K. B.; Whang, C. N.; Lee, D. W.; Ko, D. H., *Applied Physics Letters* **2005,** 87, Art No. 242906.

17. Wilk, G. D.; Wallace, R. M.; Anthony, J. M., *Journal of Applied Physics* **2001,** 89, 5243-5275.

18. Akbar, M. S.; Gopalan, S.; Cho, H. J.; Onishi, K.; Choi, R.; Nieh, R.; Kang, C. S.; Kim, Y. H.; Han, J.; Krishnan, S.; Lee, J. C., *Applied Physics Letters* **2003,** 82, 1757-1759.

19. Cho, H. J.; Lee, H. L.; Park, H. B.; Jeon, T. S.; Park, S. G.; Jin, B. J.; Kang, S. B.; Shin, Y. G.; Chung, U. I.; Moon, J. T., *Japanese Journal of Applied Physics Part 1-Regular Papers Brief Communications & Review Papers* **2005,** 44, 2230-2234.

20. Cho, M. H.; Chung, K. B.; Ko, D. H., *Applied Physics Letters* **2006,** 89, Art. No. 142908

21. Chung, K. B.; Whang, C. N.; Cho, M. H.; Yim, C. J.; Ko, D. H., *Applied Physics Letters* **2006,** 88, Art. No. 081903

22. Ganem, J. J.; Trimaille, I.; Vickridge, I. C.; Gusev, E. P., *Nuclear Instruments & Methods in Physics Research Section B-Beam Interactions with Materials and Atoms* **2006,** 249, 517-522.

23. Ikarashi, N.; Watanabe, K.; Masuzaki, K.; Nakagawa, T.; Miyamura, M., *Journal of Applied Physics* **2006,** 100, Art No. 063507.

24. Inumiya, S.; Miura, T.; Shirai, K.; Matsuki, T.; Torii, K.; Nara, Y., *Japanese Journal of Applied Physics Part 1-Regular Papers Brief Communications & Review Papers* **2006,** 45, 2898-2902.

25. Oshima, M.; Takahashi, H.; Okabayashi, J.; Toyoda, S.; Kumigashira, H.; Inoue, M.; Mizutani, M.; Yugami, J., *Journal of Applied Physics* **2006,** 100, Art No. 033709.

26. Quevedo-Lopez, M. A.; Chambers, J. J.; Visokay, M. R.; Shanware, A.; Colombo, L., *Applied Physics Letters* **2005,** 87, Art No. 012902.

27. Sayan, S.; Nguyen, N. V.; Ehrstein, J.; Chambers, J. J.; Visokay, M. R.; Quevedo-Lopez, M. A.; Colombo, L.; Yoder, D.; Levin, I.; Fischer, D. A.; Paunescu, M.; Celik, O.; Garfunkel, E., *Applied Physics Letters* **2005,** 87, Art. No. 212905

28. Toyoda, S.; Okabayashi, J.; Takahashi, H.; Oshima, M.; Lee, D. I.; Sun, S.; Sun, S.; Pianetta, P. A.; Ando, T.; Fukuda, S., *Applied Physics Letters* **2005,** 87, Art No 182908

29. Pant, G.; Punchaipetch, P.; Kim, M. J.; Wallace, R. M.; Gnade, B. E., *Thin Solid Films* **2004,** 460, 242-246.

30. Yamaguchi, M.; Sakoda, T.; Minakata, H.; Xiao, S. Q.; Morisaki, Y.; Ikeda, K.; Mishima, Y., *Ieee Transactions on Electron Devices* **2006,** 53, 923-925.

31. Kamimuta, Y.; Koike, M.; Ino, T.; Suzuki, M.; Koyama, M.; Tsunashima, Y.; Nishiyama, A., *Japanese Journal of Applied Physics Part 1-Regular Papers Short Notes & Review Papers* **2005,** 44, 1301-1305.

32. Koike, M.; Ino, T.; Kamimuta, Y.; Koyama, M.; Kamata, Y.; Suzuki, M.; Mitani, Y.; Nishiyama, A., *Physical Review B* **2006,** 73, Art No 125123.

33. Koyama, M. S., H; Koike, M; Ino, T; Suzuki, M; Iijima, R; Kamimuta, Y; Takashima, A; Hongo C; and Nishiyama, A: In *IEDM Tech. Dig.*, 2003; 2003; p 931.

34. Koyama, M.; Kamimuta, Y.; Koike, M.; Ino, T.; Nishiyama, A., *Japanese Journal of Applied Physics Part 1-Regular Papers Brief Communications & Review Papers* **2005,** 44, 2311-2315.

35. Uedono, A.; Ikeuchi, K.; Otsuka, T.; Shiraishi, K.; Yamabe, K.; Miyazaki, S.; Umezawa, N.; Hamid, A.; Chikyow, T.; Muramatsu, T. O. M.; Suzuki, R.; Inumiya, S.; Kamiyama, S.; Akasaka, Y.; Nara, Y.; Yamada, K., *Journal of Applied Physics* **2006,** 99, Art No. 054507.

36. Raveh, A.; Brewer, J.; Irene, E. A., *Journal of Vacuum Science & Technology A* **2001,** 19, 17-24.

37. Yamamoto, T.; Miyamoto, T.; Karen, A., *Applied Surface Science* **2004,** 231-2, 561-564.

38. Suzuki, M.; Takashima, A.; Koyama, M.; Iijima, R.; Ino, T.; Takenaka, M., *Nuclear Instruments & Methods in Physics Research Section B-Beam Interactions with Materials and Atoms* **2004,** 219-20, 851-855.

39. Wang, X. G.; Liu, J.; Zhu, F.; Yamada, N.; Kwong, D. L., *Ieee Transactions on Electron Devices* **2004,** 51, 1798-1804.

40. Koyama, M.; Kamimuta, Y.; Koike, M.; Suzuki, M.; Nishiyama, A., *Japanese Journal of Applied Physics Part 1-Regular Papers Short Notes & Review Papers* **2004,** 43, 1788-1794.

41. Kang, C. S. C., H.; Onishi, K.; Choi, R; Kim, Y. H.; Nieh, R.; Han, J.; Krishnan, S.; Shahriar, A.; Lee, J. C.; In *Tech. Dig. Int. Electron Devices Meet. 2002*, p 865.

42. Barrett, N. T.; Renault, O.; Besson, P.; Le Tiec, Y.; Martin, F., *Applied Physics Letters* **2006,** 88, Art No. 162906.

43. Shirley, D. A., *Journal of Vacuum Science & Technology* **1975,** 12, 280-285.

44. Barr, T. L.; Hoppe, E.; Dugall, T.; Shah, P.; Seal, S., *Journal of Electron Spectroscopy and Related Phenomena* **1999,** 99, 95-103.

45. Siegbahn, K., *ESCA applied to free molecules*. North-Holland Pub. Co: Amsterdam, 1969.

46. Siegbahn, K., *Philosophical Transactions of the Royal Society of London Series a-Mathematical and Physical Sciences* **1970,** 268, 33-57.

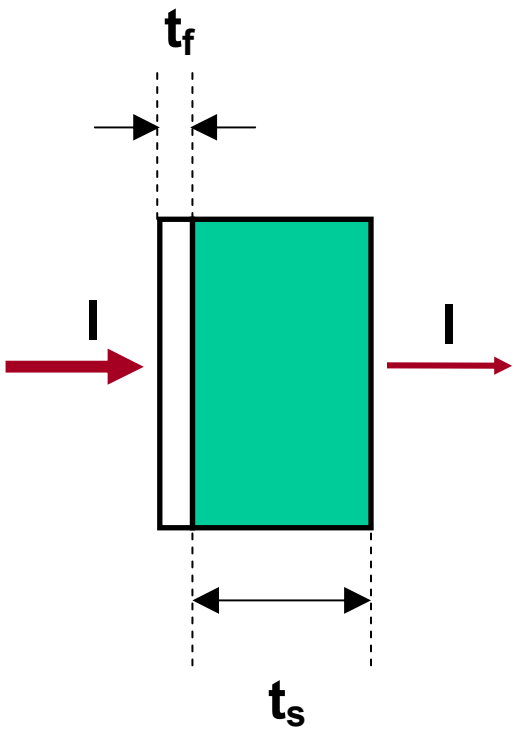

Figure 4.1. IR transmission through a film/substrate system. The transmitted intensity, I, is approximated by Beer's law, $I = I_o exp[-(A_f + A_s)]$, where I_o is the incident beam intensity. A_f and A_s are the absorbance's of the film and substrate, respectively.

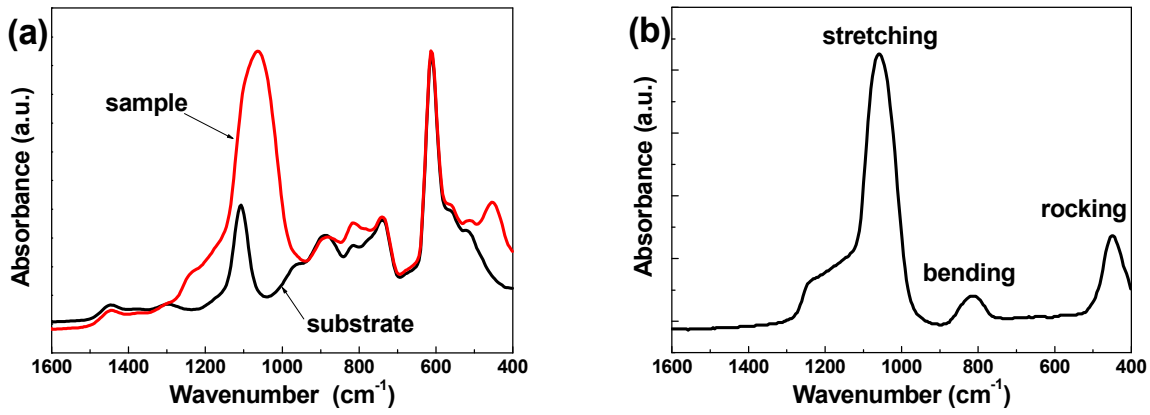

Figure 4.2. FTIR spectra of plasma deposited SiO_2 film, (a) sample and Si substrate and (b) SiO_2 film only.

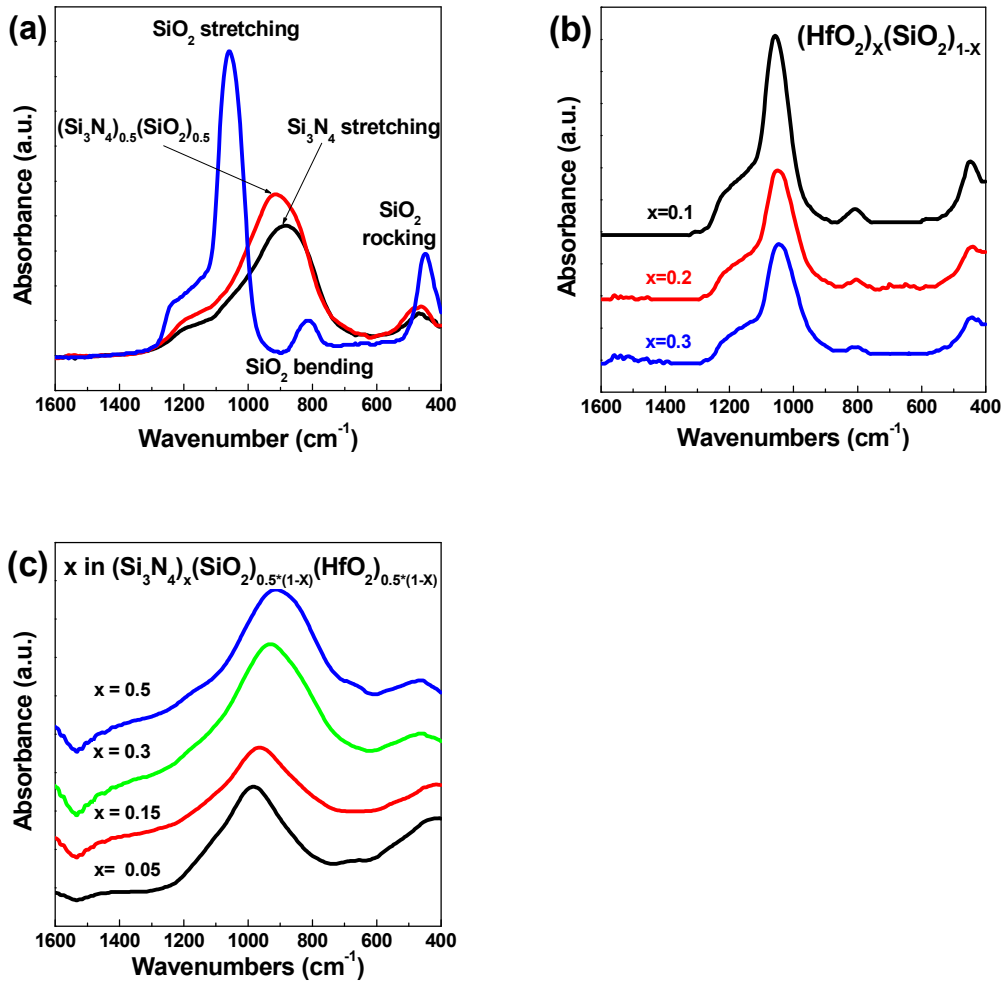

Figure 4.3. FTIR spectra of as deposited alloys (a) Si_3N_4, SiO_2, and SiON. (b) Hf silicate. (c) Hf-Si oxynitride.

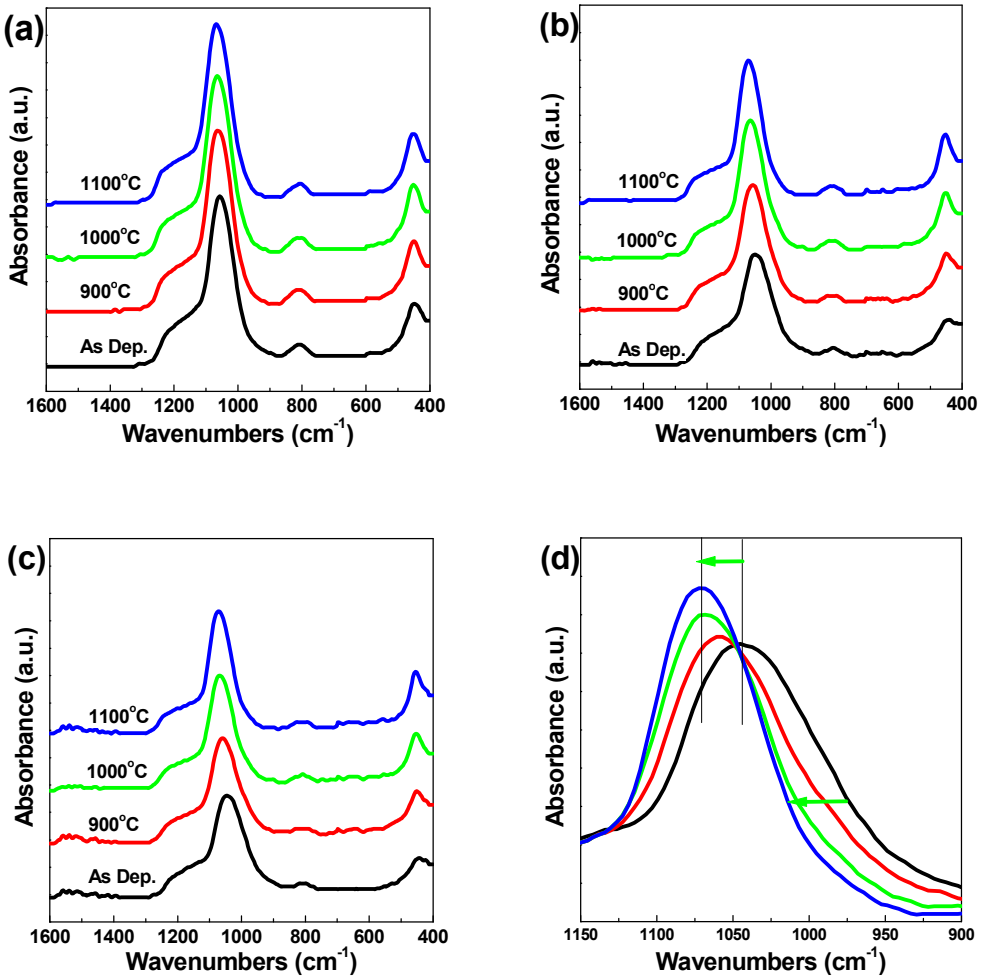

Figure 4.4. FTIR spectra of $(HfO_2)_X(SiO_2)_{1-X}$ alloys with respect to anneal temperatures (a) x = 0.1. (b) x = 0.2. (c) x = 0.3. (d) x = 0.3 in detail.

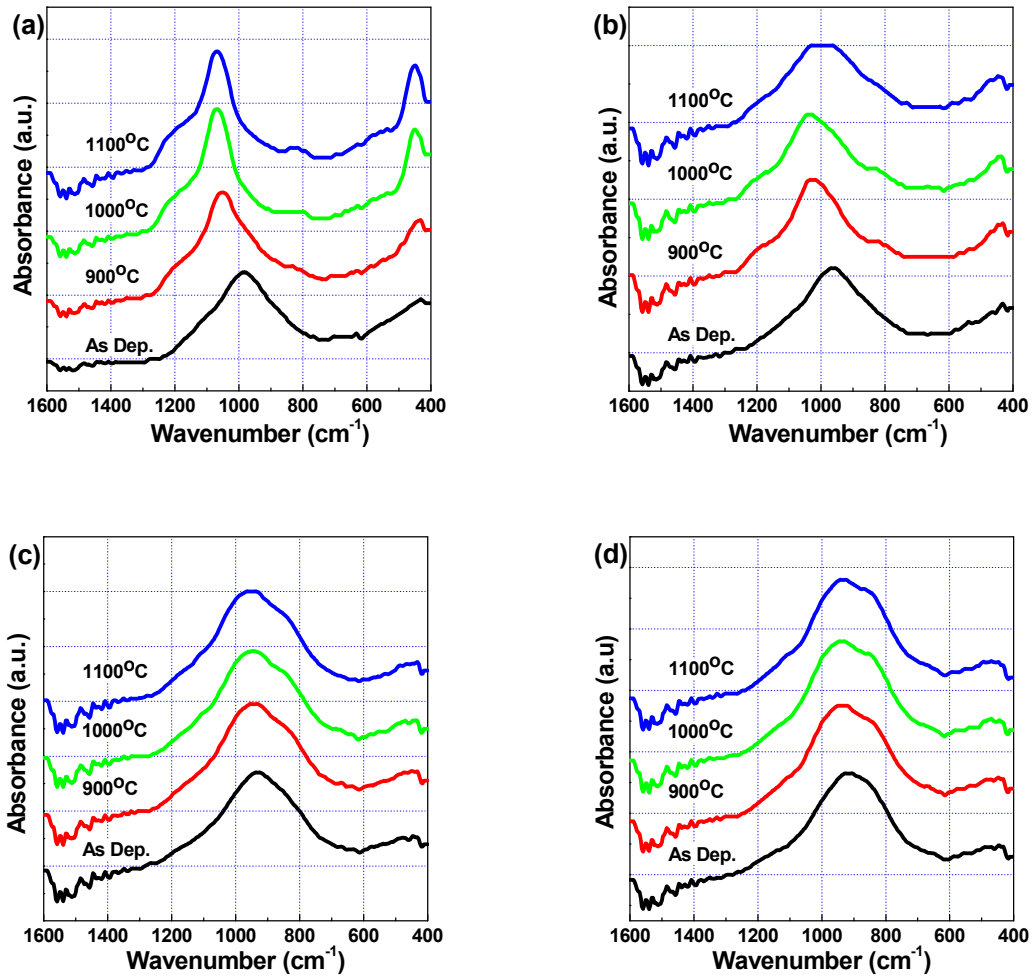

Figure 4.5. FTIR spectra of $(Si_3N_4)_X(SiO_2)_{0.5\cdot(1-X)}(HfO_2)_{0.5\cdot(1-X)}$ alloys with respect to anneal temperatures. (a) x = 0.07. (b) x = 0.17. (c) x = 0.33. (d) x = 0.49.

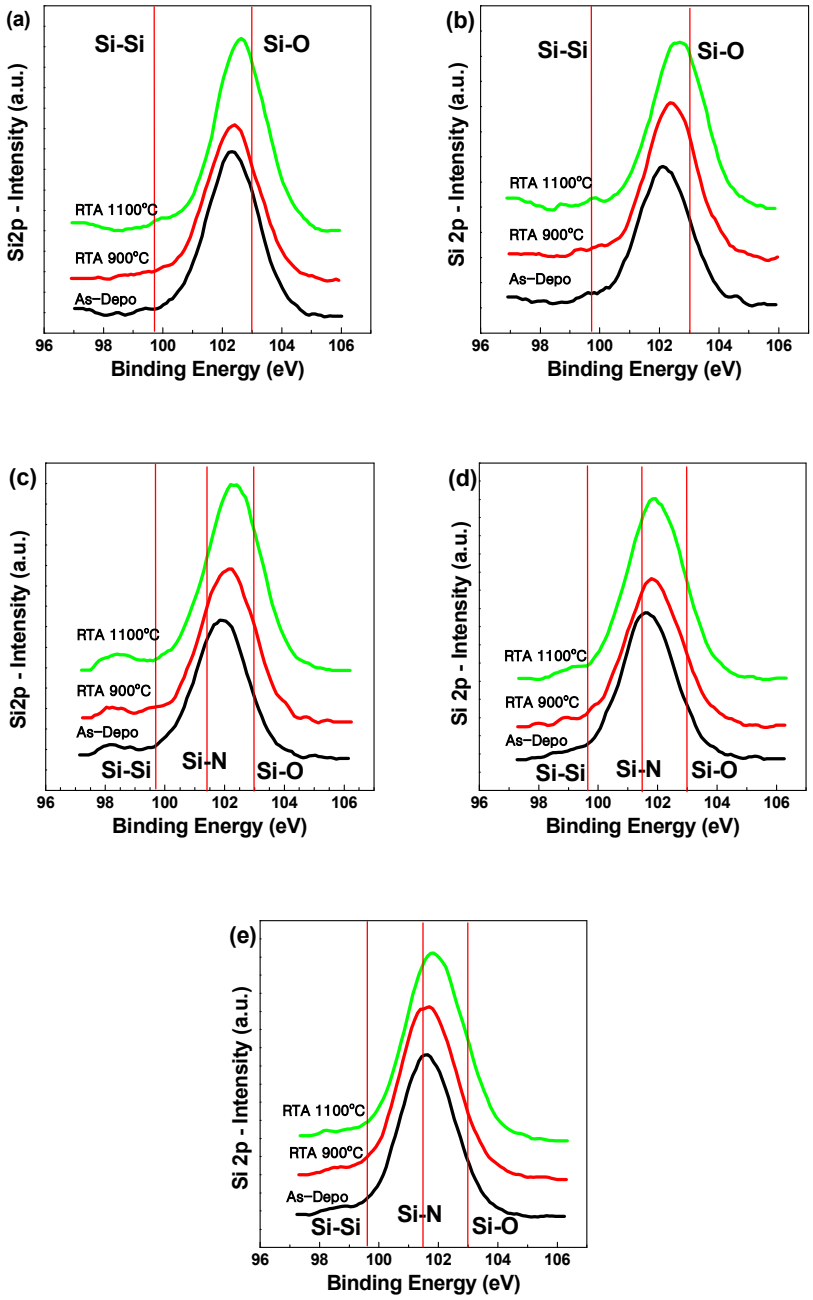

Figure 4.6. XPS core-level Si 2p spectra with respect to anneal temperature of $(HfO_2)_X(SiO_2)_{1-X}$ (a) x = 0.2. (b) x = 0.4. $(Si_3N_4)_X(SiO_2)_{0.5\cdot(1-X)}(HfO_2)_{0.5\cdot(1-X)}$ (c) x = 0.13. (d) x = 0.33. (e) x = 0.50.

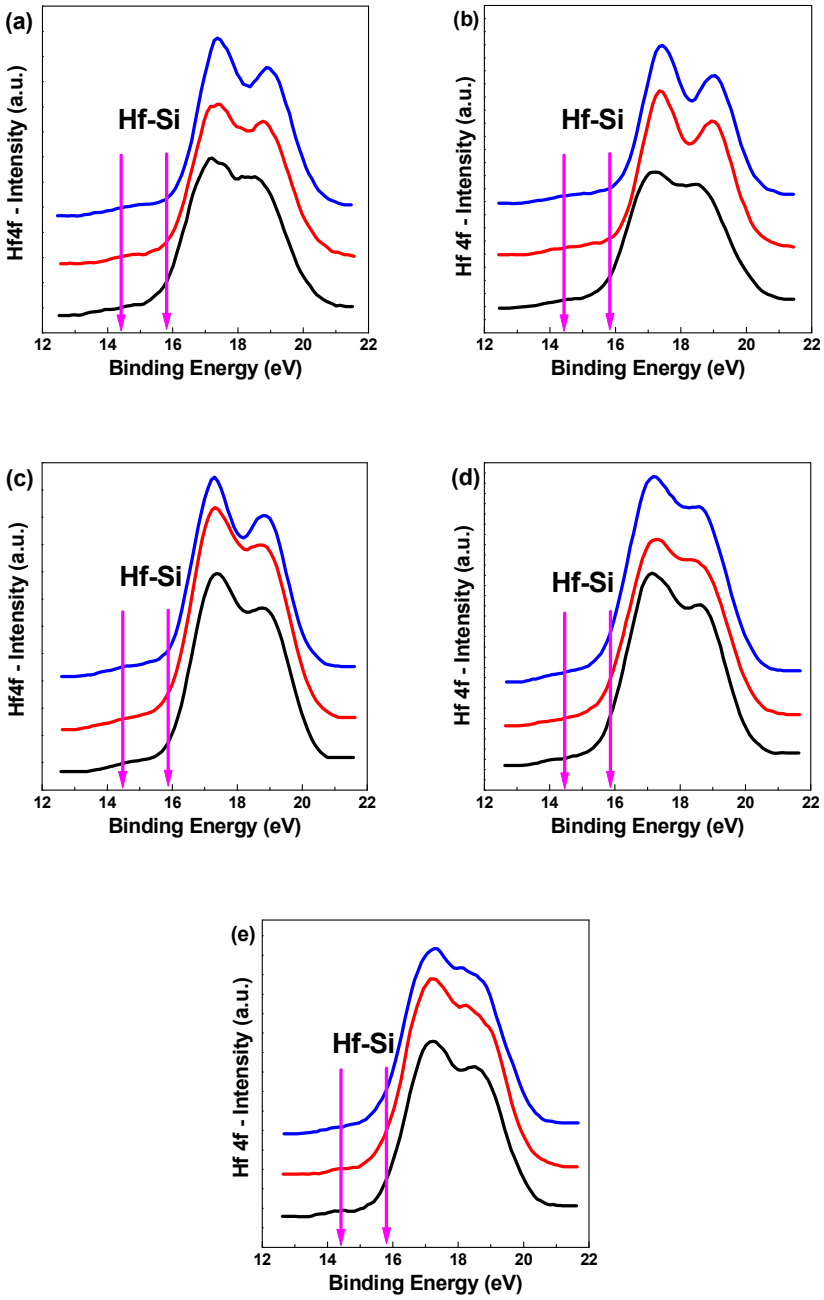

Figure 4.7. XPS core-level Hf 4f spectra with respect to anneal temperature of $(HfO_2)_X(SiO_2)_{1-X}$ (a) x = 0.2. (b) x = 0.4. $(Si_3N_4)_X(SiO_2)_{0.5\cdot(1-X)}(HfO_2)_{0.5\cdot(1-X)}$ (c) x = 0.13. (d) x = 0.33. (e) x = 0.50.

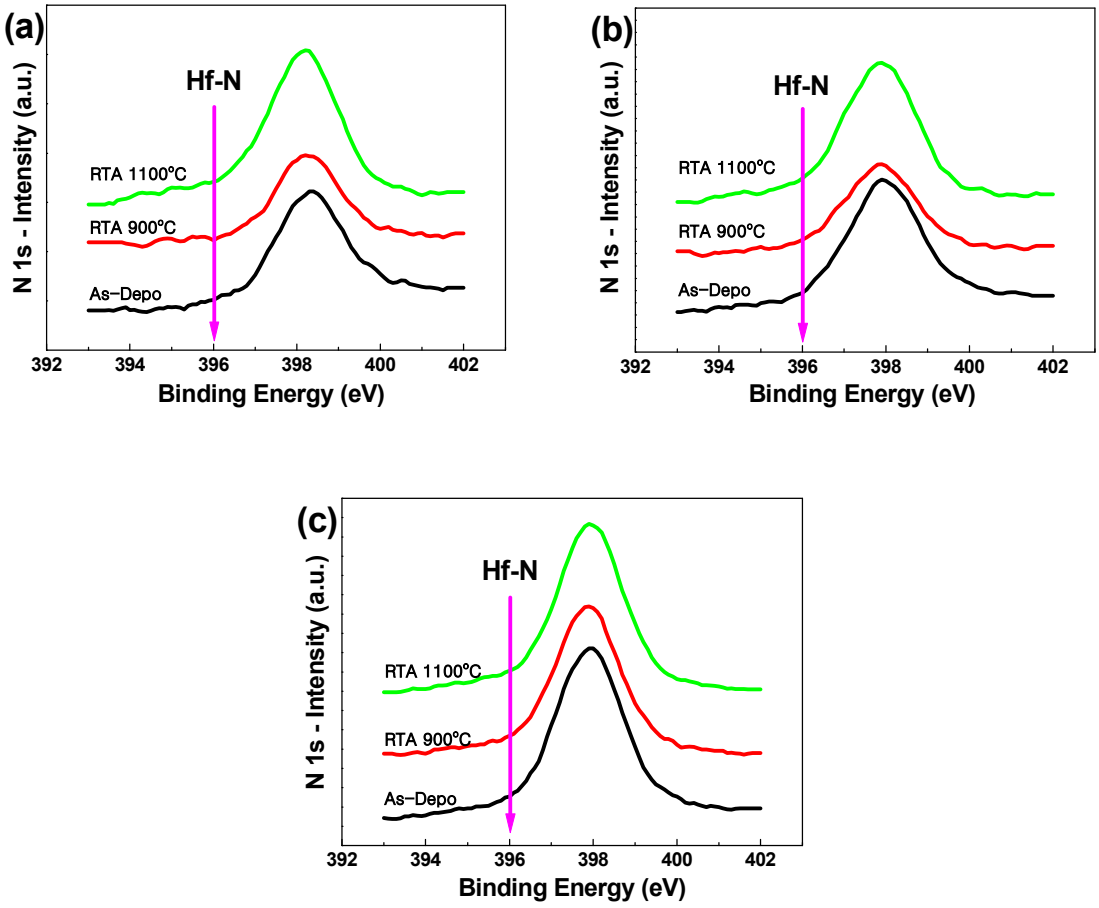

Figure 4.8. XPS core-level N 1s spectra with respect to anneal temperature of $(Si_3N_4)_X(SiO_2)_{0.5\cdot(1-X)}(HfO2)_{0.5\cdot(1-X)}$ (a) x = 0.13. (b) x = 0.33. (c) x = 0.50.

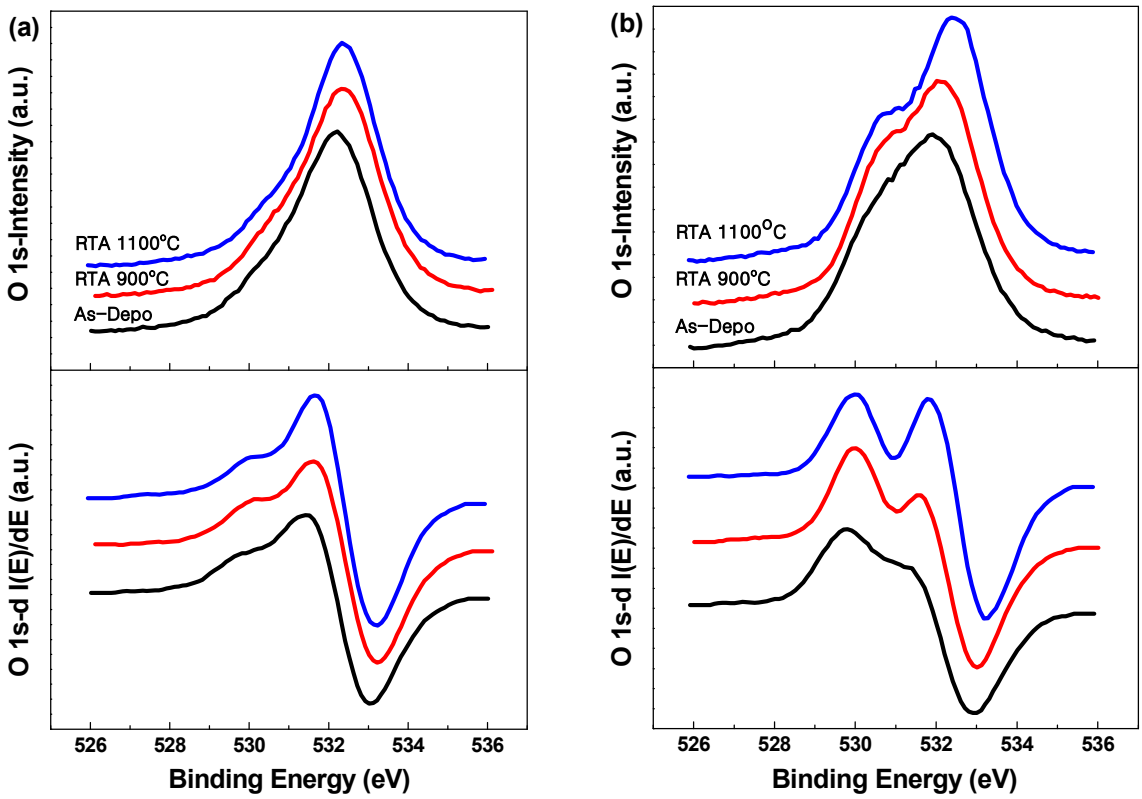

Figure 4.9. XPS core-level O 1s spectra and its corresponding first derivative spectra with respect to anneal temperature of $(HfO_2)_X(SiO_2)_{1-X}$ (a) x =0.2. (b) x = 0.4.

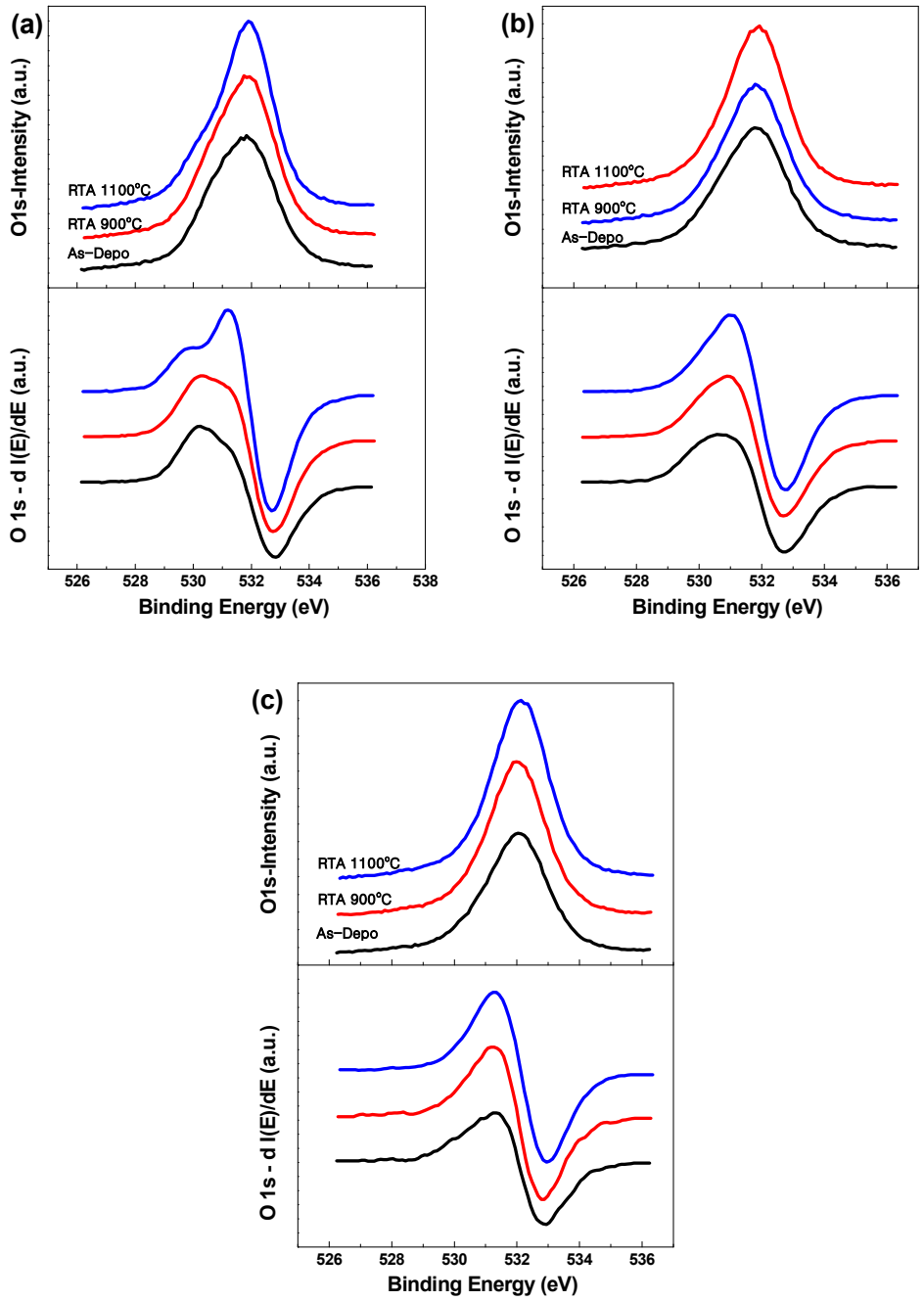

Figure 4.10. XPS core-level O 1s spectra and its corresponding first derivative spectra with respect to anneal temperature of $(Si_3N_4)_X(SiO_2)_{0.5\cdot(1-X)}(HfO_2)_{0.5\cdot(1-X)}$,

(a) x = 0.13. (b) x = 0.33. (c) x = 0.50.

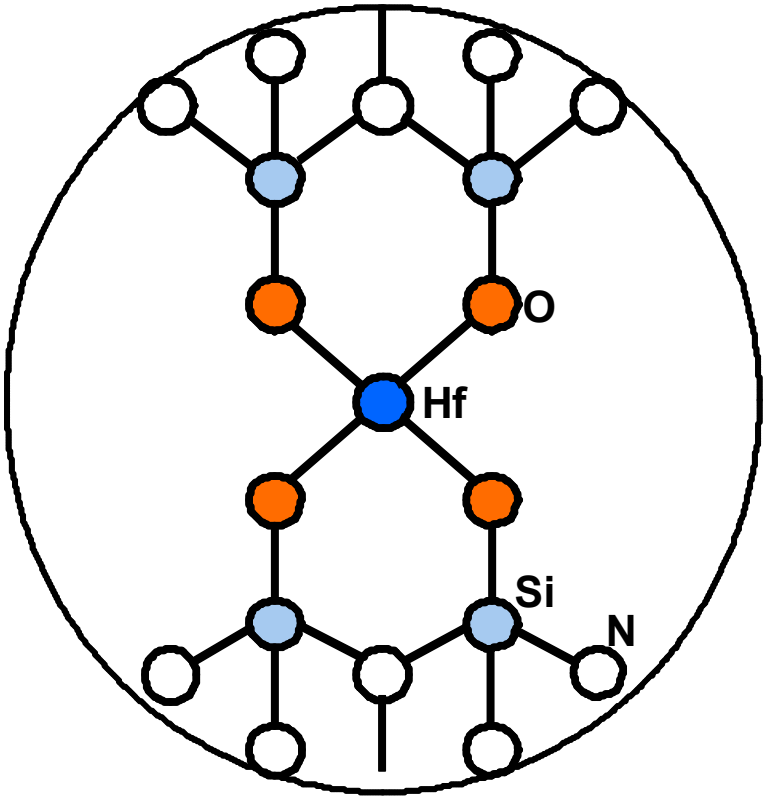

Figure 4.11. Schematic representation of local bonding arrangement of Hf-Si oxynitride alloys with the composition of 33~40% of Si_3N_4, 30~33% of SiO_2 and HfO_2.

Chapter 5. Low Temperature Atomic Layer Deposition.

5.1. Brief History of ALD

Atomic layer deposition (ALD) has recently received much attention as a promising deposition technique for advanced thin-film structures. ALD was developed and introduced as atomic layer epitaxy (ALE) in the late 1970s by Suntola and co-workers. They demonstrated processes based on element reactants: the Zn/S process to grow ZnS, the Sn/O_2 process to grow SnO_2, and the Ga/P process to grow GaP for display devices.[1-3] In the mid 1980s, the applicability extended to III-V compound semiconductors.[4, 5] Since the mid 1990s, the silicon-based microelectronics industry has focused on ALD technology. This interest is a direct consequence of the efforts to find a suitable process for the aggressively shrinked device dimensions and the high-aspect ratios in integrated circuits. ALD is currently considered as a promising deposition method for fabricating conformal, uniformly thin films with precise thickness and composition control over large scales. At the same time, film thickness shrinking makes the major disadvantage of ALD, the low deposition rate, less significant.

5.2. Characteristics of ALD

ALD is a special modification of CVD, in which the film growth takes place in a cyclic manner. Typical growth cycle in ALD consists of four steps: i) introduction of the precursor, ii) purge with inert gas or evacuation of the reaction chamber, iii) introduction of the reactant, and iv) further purge or evacuation. The film thickness can be accurately controlled by the number of cycles the process is repeated. During ALD, precursor molecules adsorb or react with surface

groups and saturate the substrate, i.e. form a (sub) monolayer of the precursor on the substrate. Excess precursor molecules and volatile byproducts are removed by a purge gas (e.g., Ar). Then the reactant gas is subsequently exposed onto the substrate, where it reacts with the adsorbed (sub) monolayer of the precursor to form a layer of the film. Due to the self-limiting reaction character, ALD is a surface-controlled process, where process parameters such as the flow amount of the reactants and temperature have little or no influence. Because of the surface control, ALD-grown films are extremely conformal and uniform in thickness.

There is a clear difference in the trends of the growth rate as a function of growth temperature and the amount of precursor dose between ALD and CVD. Figure 5.1 shows typical trends of growth rate as a function of growth temperature for the ALD process.[6] The growth rate increases with increasing growth temperature at low growth temperature region. In this region, the precursor adsorption or reaction between precursor and surface species is thermally activated. Thus, the saturation of adsorption or reaction is kinetically limited with low thermal energy, which results undesirable long reaction time. When the precursor molecules condense on the substrate, the growth trend may show opposite behavior. When the growth temperatures are high enough to provide thermal activation energy for the chemical reactions, the growth trends show a plateau or inflection region with respect to the growth temperature. This temperature range is often called the ‘‘ALD process window’’, in which self-limiting ALD behavior exists.[7] At higher growth temperature above this temperature range, the growth rate may be increased again with growth temperature by thermal decomposition of reactants or decreased by desorption of desired products or reactants.

In the ALD process window, the growth rate shows saturation behavior with increasing precursor flux (Figure 5.2). From the saturation curve which is the growth rate determined as a function of precursor exposure (Langmuir, 1 L = 10^{-6} Torr·s) per cycle, the precursor exposure can be optimized. Within this proper growth condition, the growth rate is not affected by the turbulence of process parameters. This self-limiting character of ALD can be verified using in-situ monitoring the extent of surface reaction using quadrupole mass spectrometry (QMS)[8-10] or quartz crystal microbalance (QCM).[8, 11-13]

Though the self-limiting growth condition is achieved, only a fraction of monolayer, (i.e. submonolayer) is deposited per each cycle. This non-ideal growth rate behavior is due to steric hindrance of the ligands in precursor molecules[14-16] and the number of reactive surface sites.[17-19] The ligands of adsorbed precursor molecules shield part of the reactive surface sites from newly introduce precursors. The number of available reactive bonding sites on the surface is less than required for achieving a full coverage by precursor adsorption. Although there remains space which is not shielded by the ligands on the surface, no reactive bonding sites are available. In both case, there is no room for further gas-solid surface reaction.

5.3. The needs of metal ALD

Since ALD provides excellent step coverage on aggressive topographic structures, ALD has expanded rapidly its application area in microelectronics. The self-limiting character of ALD can produce nearly 100% conformal metal film in very high aspect ratio structures (e.g. metal interconnection through via hole). In contrast, it is very difficult to fabricate conformal film with PVD technique due to its intrinsic anisotropic atomic flux. Although CVD shows better

conformality than PVD, a good conformality of CVD can be achieved only at low growth temperature of surface reaction limited region with very low growth rate. In addition, the low reaction rate can cause contamination by nonreacted precursors or by-products. Since ALD is inherently a self-limited deposition process by the alternate exposure of two or more precursors separated by purge steps, thickness and composition can be controlled with the submonolayer level.

Another benefit of ALD is the generally lower growth temperature compared to the parallel CVD reaction. Since the ALD process occurs exclusively through surface reactions, the growth rate of ALD is very low compared to other conventional deposition techniques. This low growth rate is regarded as the limitation of ALD for mass production. However, this problem is not significant because the device scale down continues and the need for a deposition technique with excellent step coverage at low growth temperatures has increased. Due to aggressive scale down, the process temperature limitation has become more severe. High process temperature can lead cross contamination by diffusion of dopant in silicon to metal interconnection layer and damage on temperature-sensitive materials such as low-k inter layer dielectric (ILD) materials.

5.4. Applications of ALD Metals

5.4.1. Interconnection Technology

Cu interconnects are widely used since its higher electromigration (EM) resistance as well as lower resistivity compared to Al wiring. However, Cu has higher diffusivity and easily diffuses through dielectrics, thus, Cu interconnect technology requires a thin stable diffusion barrier with high conformality. Additionally, a diffusion barrier layer can act as an adhesion

layer. There are some requirements for diffusion barrier / adhesion layer application such as low solubility in Cu, low deposition temperature, and adhesion on low-k or SiO_2, etc. Transition metals, (e.g. Ta, Ti, W, Cr, and Co, etc.) metal nitrides, (e.g. TiN, TaN, and W_2N, etc.) and ternary nitrides, (e.g. $TiSi_xN_y$, $TaSi_xN_y$, $TiAl_xN_y$, WSi_xN_y, WC_xN_y, and WB_xN_y, etc.) have been widely studied for this application. However, metals and metal nitrides can easily crystallize even moderate temperature during post process integration steps (e.g. forming gas anneal). Since grain boundaries play an important role as diffusion path for Cu, the amorphous phase ternary nitrides are expected to be a good solution.

5.4.2. Gate Electrode

Continued gate length scaling in CMOS, the conventional polysilicon gate electrode cannot meet the electrical properties for circuit operation due to its depletion effect which accounts for 4~5 Å of equivalent oxide thickness in inversion and low conductivity which cause signal delay. Metal gate electrode is free from the depletion effect. In addition, the boron penetration from the poly-Si PMOS gate and the high temperature activation process step, required for the poly-Si gate, is removed.

Metal with work function near the silicon band edge (within 0.2 eV from the conduction band of Si for NMOS and valence band of Si for PMOS) have been widely studied. For NMOS applications, low work function metal ternary nitrides such as TiSiN and TiAlN are being studied. For PMOS applications, high work function metal, noble metals, such as Pt, Ru, Ir, Rh are being investigated.

5.4.3. Magnetic nanostructure

Patterned magnetic nanostructures are have recently been the subject of numerous studies because of their possible implementation into future ultrahigh density (>100 Gbit/in^2) data storage devices.[20-22] Variety of fabrication techniques such as electrochemical deposition,[23, 24] pulsed electro-deposition,[25] precursor injection and subsequent reduction,[26] and wetting with polymer solution containing a metal-organic precursor,[27] etc. However, these methods have limitations of precise thickness control and a fine tuning of magnetic properties.

Ni and Co nanotubes were fabricated in alumina membranes using ALD by Dr. Nielsch's research group.[28] They used nickelocene [$Ni(C_5H_5)_2$] and cobaltocene [$Co(C_5H_5)_2$] as precursors and H_2O and O_3 as reactants. The Ni and Co films were produced by the ALD process including oxidation and subsequent reduction and the combination of oxidation during the ALD process and reduction after ALD process. The growth temperature for the ALD process was 330℃ and Post deposition anneal for reduction was done at 400℃ under 5% H_2 in Ar atmosphere for 5h.

5.4.4. Catalysis

The deposition of noble metal particles and films by ALD has recently gained interest in the fields of catalysis. The application to catalysis requires the ability to control the amount of metal and achieve high dispersion, while the ability to produce conformal and uniform films is the major requirement for microelectronics. Palladium catalysts were prepared from $Pd(thd)_2$ precursor.[29] Ruthenium and platinum catalysts prepared from $Ru(thd)_3$ and $Pt(CpMe)Me_3$ precursors.[30, 31] Since noble metal has a less tendency to be oxidized, Pt,[8, 32-34] Ru,[35-38] Pd,[39-41] Ir,[42, 43] and Rh[44, 45] can be grown by ALD not only with hydrogen but also with oxygen. Since it

is important to control the number of active sites on the surface for the optimized catalytic activity, surface treatment on catalyst support has been studied.[43, 46]

5.4.5. Nanotubes

Inorganic micro/nano-tubes with precisely defined nanoscale walls have attracted significant attention due to their large potential for applications in electronics, optics, sensors, filtration, data storage, and so on. A variety of different technologies have been studied to produce such tubes from various materials. Electrospinning has become a promising technology for the fabrication of the nanoscale fiber with uniform diameter and good morphology. ALD of Al_2O_3 on electrospun polymer fibers as a direct pathway to inorganic microtubes with well defined nanoscale walls was developed.[47] To the best of our knowledge no reports have been published on nanotubes of pure metal, which can be of interest for the technologies including, but not limited to, photonics, medicine, nanoelectronics, nanosensors, or nanofiltration.

5.5. Low temperature metal ALD

Low growth temperatures have many benefits in the applications of metals. Metal thin films can be grown with smooth morphology at lower deposition temperatures because the crystal growth is hindered or retarded.[35] Smooth bottom electrodes have been shown to provide lower leakage currents in the memory capacitors.[48, 49] Likewise, metal diffusion layer with lower degree of crystallization or amorphous phase possibly reduce the grain-boundary diffusion of copper through the metal diffusion barrier, as is the case with transition metal nitride barriers.19 In addition, lower deposition temperature may retard the barrier oxidation[48] during the metal

deposition. In interconnect metallization, low deposition temperature is required to avoid damage on temperature-sensitive materials such as low-k inter layer dielectric (ILD) materials.[50, 51]

Furthermore, for the applications mentioned in section 5.4.5, the low temperature process has become more important. The low temperature ALD can be achieved with energy enhanced methods such as plasma[37, 40, 52-55] or UV laser[56] assisted processes. However, thermal ALD processes fulfill best the requirement of self-limiting surface reactions on complex three-dimensional substrates. In energy enhanced processes, the energy is transferred with directionality and there may be shielded region. This leads problems with conformality and uniformity. The surface reaction chemistry of precursor with respect to temperature will be an important area of further study.

5.6. References

1. Suntola, T., Antson, J.: US Patent 4,058,430. 1977.

2. Suntola, T.; Hyvarinen, J., *Annual Review of Materials Science* **1985,** 15, 177-195.

3. Suntola, T., *Thin Solid Films* **1992,** 216, 84-89.

4. *Atomic layer epitaxy / edited by T. Suntola and M. Simpson.* Chapman and Hall: Blackie, 1990.

5. Bedair, S. M., *Journal of Vacuum Science & Technology B* **1994,** 12, 179-185.

6. Ritala, M. L., M, *Handbook of thin film materials / edited by Hari Singh Nalwa.* Academic Press: San Diego, 2002.

7. Suntola, T., *Applied Surface Science* **1996,** 101, 391-398.

8. Aaltonen, T.; Rahtu, A.; Ritala, M.; Leskela, M., *Electrochemical and Solid State Letters* **2003,** 6, C130-C133.

9. Niinisto, J.; Rahtu, A.; Putkonen, M.; Ritala, M.; Leskela, M.; Niinisto, L., *Langmuir* **2005,** 21, 7321-7325.

10. Henn-Lecordier, L.; Lei, W.; Anderle, M.; Rubloff, G. W., *Journal of Vacuum Science & Technology B* **2007,** 25, 130-139.

11. Matero, R. A.; Rahtu, A.; Ritala, M., *Langmuir* **2005,** 21, 3498-3502.

12. Rocklein, M. N.; George, S. M., *Analytical Chemistry* **2003,** 75, 4975-4982.

13. Elam, J. W.; Schuisky, M.; Ferguson, J. D.; George, S. M., *Thin Solid Films* **2003,** 436, 145-156.

14. Ylilammi, M., *Thin Solid Films* **1996,** 279, 124-130.

15. Lim, J. W.; Park, H. S.; Kang, S. W., *Journal of the Electrochemical Society* **2001,** 148, C403-C408.

16. Rautiainen, A.; Lindblad, M.; Backman, L. B.; Puurunen, R. L., *Physical Chemistry Chemical Physics* **2002,** 4, 2466-2472.

17. Haukka, S.; Lakomaa, E. L.; Suntola, T., *Thin Solid Films* **1993,** 225, 280-283.

18. Gobbert, M. K.; Prasad, V.; Cale, T. S., *Journal of Vacuum Science & Technology B* **2002,** 20, 1031-1043.

19. Kytokivi, A.; Lakomaa, E. L.; Root, A.; Osterholm, H.; Jacobs, J. P.; Brongersma, H. H., *Langmuir* **1997,** 13, 2717-2725.

20. Ross, C., *Annual Review of Materials Research* **2001,** 31, 203-235.

21. Chou, S. Y., *Proceedings of the Ieee* **1997,** 85, 652-671.

22. Kong, L. S.; Zhuang, L.; Chou, S. Y., *Ieee Transactions on Magnetics* **1997,** 33, 3019-3021.

23. Xue, S. H.; Cao, C. B.; Zhu, H. S., *Journal of Materials Science* **2006,** 41, 5598-5601.

24. Bao, J. C.; Tie, C. Y.; Xu, Z.; Zhou, Q. F.; Shen, D.; Ma, Q., *Advanced Materials* **2001,** 13, 1631-+.

25. Davis, D. M.; Moldovan, M.; Young, D. P.; Henk, M.; Xie, X. G.; Podlaha, E. J., *Electrochemical and Solid State Letters* **2006,** 9, C153-C155.

26. Su, H. L.; Ji, G. B.; Tang, S. L.; Li, Z.; Gu, B. X.; Du, Y. W., *Nanotechnology* **2005,** 16, 429-432.

27. Nielsch, K.; Castano, F. J.; Ross, C. A.; Krishnan, R., *Journal of Applied Physics* **2005,** 98, -.

28. Daub, M.; Knez, M.; Goesele, U.; Nielsch, K., *Journal of Applied Physics* **2007,** 101, -.

29. Molenbroek, A. M.; Haukka, S.; Clausen, B. S., *Journal of Physical Chemistry B* **1998,** 102, 10680-10689.

30. Lashdaf, M.; Hatanpaa, T.; Krause, A. O. I.; Lahtinen, J.; Lindblad, M.; Tiitta, M., *Applied Catalysis a-General* **2003,** 241, 51-63.

31. Lashdaf, M.; Lahtinen, J.; Lindblad, M.; Venalainen, T.; Krause, A. O. I., *Applied Catalysis a-General* **2004,** 276, 129-137.

32. Utriainen, M.; Kroger-Laukkanen, M.; Johansson, L. S.; Niinisto, L., *Applied Surface Science* **2000,** 157, 151-158.

33. Aaltonen, T.; Ritala, M.; Sajavaara, T.; Keinonen, J.; Leskela, M., *Chemistry of Materials* **2003,** 15, 1924-1928.

34. Zhu, Y.; Dunn, K. A.; Kaloyeros, A. E., *Journal of Materials Research* **2007,** 22, 1292-1298.

35. Aaltonen, T.; Alen, P.; Ritala, M.; Leskela, M., *Chemical Vapor Deposition* **2003,** 9, 45-49.

36. Kwon, O. K.; Kim, J. H.; Park, H. S.; Kang, S. W., *Journal of the Electrochemical Society* **2004,** 151, G109-G112.

37. Kwon, O. K.; Kwon, S. H.; Park, H. S.; Kang, S. W., *Electrochemical and Solid State Letters* **2004,** 7, C46-C48.

38. Park, K. J.; Terry, D. B.; Stewart, S. M.; Parsons, G. N., *Langmuir* **2007,** 23, 6106-6112.

39. Senkevich, J. J.; Tang, F.; Rogers, D.; Drotar, J. T.; Jezewski, C.; Lanford, W. A.; Wang, G. C.; Lu, T. M., *Chemical Vapor Deposition* **2003,** 9, 258-264.

40. Ten Eyck, G. A.; Senkevich, J. J.; Tang, F.; Liu, D. L.; Pimanpang, S.; Karaback, T.; Wang, G. C.; Lu, T. M.; Jezewski, C.; Lanford, W. A., *Chemical Vapor Deposition* **2005,** 11, 60-66.

41. Elam, J. W.; Zinovev, A.; Han, C. Y.; Wang, H. H.; Welp, U.; Hryn, J. N.; Pellin, M. J., *Thin Solid Films* **2006,** 515, 1664-1673.

42. Aaltonen, T.; Ritala, M.; Sammelselg, V.; Leskela, M., *Journal of the Electrochemical Society* **2004,** 151, G489-G492.

43. Silvennoinen, R. J.; Jylha, O. J. T.; Lindblad, M.; Sainio, J. P.; Puurunen, R. L.; Krause, A. O. I., *Applied Surface Science* **2007,** 253, 4103-4111.

44. Aaltonen, T.; Ritala, M.; Leskela, M., *Electrochemical and Solid State Letters* **2005,** 8, C99-C101.

45. Park, K. J.; Parsons, G. N., *Applied Physics Letters* **2006,** 89, -.

46. Kytokivi, A.; Jacobs, J. P.; Hakuli, A.; Merilainen, J.; Brongersma, H. H., *Journal of Catalysis* **1996,** 162, 190-197.

47. Peng, Q.; Sun, X. Y.; Spagnola, J. C.; Hyde, G. K.; Spontak, R. J.; Parsons, G. N., *Nano Letters* **2007,** 7, 719-722.

48. Hwang, C. S., *Materials Science and Engineering B-Solid State Materials for Advanced Technology* **1998,** 56, 178-190.

49. Yoon, D. S.; Roh, J. S., *Semiconductor Science and Technology* **2002,** 17, 1048-1057.

50. Kim, H.; Cabral, C.; Lavoie, C.; Rossnagel, S. M., *Journal of Vacuum Science & Technology B* **2002,** 20, 1321-1326.

51. Elers, K. E.; Saanila, V.; Soininen, P. J.; Li, W. M.; Kostamo, J. T.; Haukka, S.; Juhanoja, J.; Besling, W. F. A., *Chemical Vapor Deposition* **2002,** 8, 149-153.

52. Lee, K.; Kim, K.; Jeon, H.; Lee, Y.; Kim, J.; Yeom, S., *Journal of the Korean Physical Society* **2007,** 50, 1141-1146.

53. Lee, C. W.; Kim, Y. T., *Journal of Vacuum Science & Technology B* **2006,** 24, 1432-1435.

54. Jezewski, C.; Lanford, W. A.; Wiegand, C. J.; Singh, J. P.; Wang, P. I.; Senkevich, J. J.; Lu, T. M., *Journal of the Electrochemical Society* **2005,** 152, C60-C64.

55. Rossnagel, S. M.; Sherman, A.; Turner, F., *Journal of Vacuum Science & Technology B* **2000,** 18, 2016-2020.

56. Finstad, C. C.; Muscat, A. J., *Ultra Clean Processing of Silicon Surfaces Vii* **2005,** 103-104, 7-10.

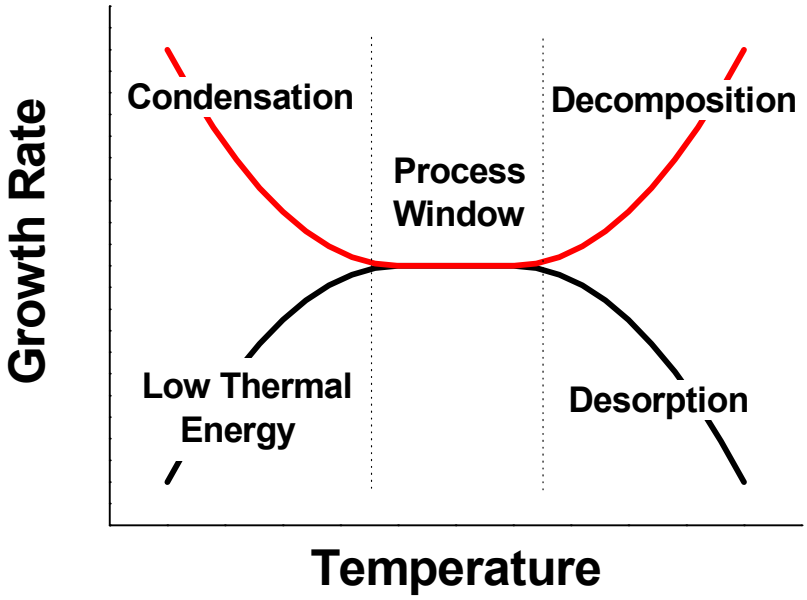

Figure 5.1. Typical trends of growth rate as a function of growth temperature for the ALD process.

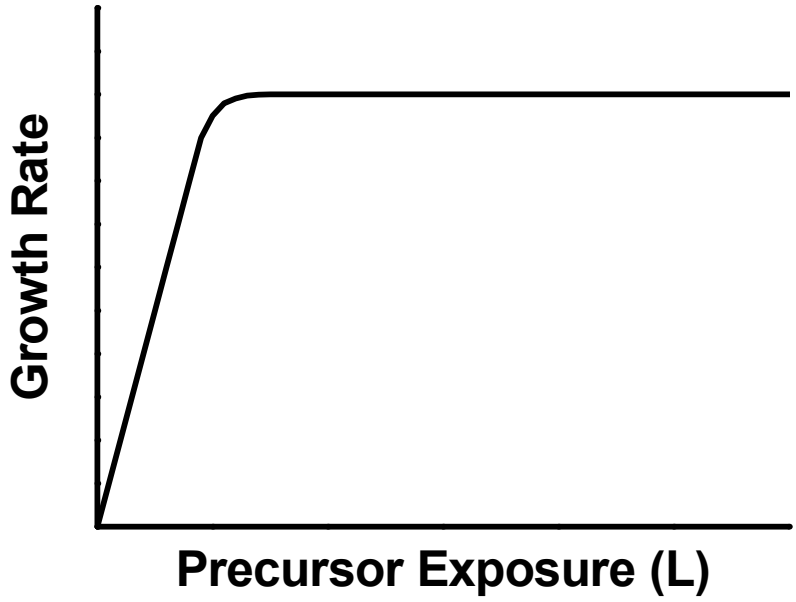

Figure 5.2. Growth rate as a function of the amount of precursor exposure with surface saturation.

This is a reprint of a manuscript submitted in Chemical Vapor Deposition,

Chapter 6. In-situ analysis of low temperature cobalt film formation using $Co_2(CO)_8$ and $Co(C_5H_5)(CO)_2$ in atomic layer deposition process sequencing.

Sang Jeong Oh[1] and Gregory N. Parsons[1,2]*

[1]Department of Material Science and Engineering

[2]Department of Chemical and Biomolecular Engineering

North Carolina State University

Raleigh, NC 27695

6.1. Abstract

Atomic layer deposition can produce highly conformal films over a variety of complex and thermally sensitive structures at low substrate temperatures. However, atomic layer deposition processes for metal films at less than 150°C are not widely available. Cobalt thin film deposition using atomic layer deposition process sequencing was studied between 30 and 130°C using $Co_2(CO)_8$ and H_2 gases using on-line quadrupole mass spectrometry and Auger electron spectroscopy. Similar experiments using cobalt cyclopentadienyl dicarbonyl and H_2 reactants were also performed between 140 and 350°C. For the dicobalt octacarbonyl precursor, mass spectroscopy and growth rate analysis showed precursor dissociation with non-self-limiting adsorption leading to continuous film growth at temperatures as low as 60°C, whereas the cyclopentadienyl dicarbonyl precursor showed evidence for CO cleavage and volatile Co(cyclopentadienyl) resulting in no film growth until ~300°C. The continuous film growth with the $Co_2(CO)_8$ is related to the zero-valent metal center, where no reduction step is required to

produce a reactive surface for adsorption. Evidence for Fisher-Tropsch catalytic production of CH_4 is observed by mass spectroscopy during the initial cycles of Co film growth.

6.2. Introduction

Cobalt is of interest as a catalyst in Fisher-Tropsch synthesis,[1] the Pauson–Khand reaction[2] and for carbon nanotube growth.[3] Cobalt's high magnetic permittivity also makes it valuable for data storage applications.[4] Because of its good thermal stability and low electrical resistivity cobalt silicide is considered an alternative to $TiSi_2$ for gate electrodes,[5,6] interconnects,[7] and contact materials[8] in electronic device applications. Cobalt thin films are widely deposited by thermal evaporation,[9] physical vapor deposition (PVD),[6] chemical vapor deposition (CVD),[5, 10-12] and atomic layer deposition (ALD).[13-16] Plasma enhanced atomic layer deposition has been of particular interest for cobalt deposition to achieve low concentrations of oxygen and carbon impurities.[14-16] Atomic layer deposition utilizes a binary sequence of self-limiting surface reactions to achieve monolayer-level control of film thickness and uniformity. The ALD process is also attractive for some applications because it typically proceeds at moderate substrate temperature to limit the rate of precursor decomposition.[17]

The applicability of ALD to low temperature film deposition and coating is beginning to open new interesting applications for ALD, including coating of temperature sensitive polymers, and templating of biological materials.[18-21] Most temperature sensitive substrate materials require processing to proceed at less than 150°C, and for some materials, maintaining the substrate near room temperature is preferred.[20, 21] To date, several metal oxides, including Al_2O_3, TiO_2 and ZnO have been formed by ALD at 150°C and below,[19, 22-24] but there are limited results reporting

elemental metallic films by thermal ALD at low substrate temperatures.[25, 26] While plasma processes have clear advantages for low temperature processing, thermal processes may be preferred for coating large surface area substrates with highly complex surface topologies.[24] Films deposited at low temperatures can have stoichiometry and impurity contents that deviate substantially from ideal composition, but for some applications for example, where coating conformality and mechanical behavior are important, some impurity content could be tolerable. Moreover, some properties can improve at low temperature. For example, the gas barrier properties of some amorphous films deposited at low temperature may be better than polycrystalline films with high grain boundary density formed at higher temperatures.[27]

In this report, we explore the thermal ALD process sequence for formation of cobalt-containing thin films at low temperatures. Reaction products are probed using in-situ quadrupole mass spectrometry and film surface composition is examined using on-line Auger electron spectroscopy. For these experiments, dicobalt octacarbonyl ($Co_2(CO)_8$) and cyclopentadienyl cobalt dicarbonyl ($Co(C_5H_5)(CO)_2$) were used as metal sources, with hydrogen as a reactant. These cobalt sources were chosen because of their ready availability and because of the known low temperature reactivity of cobalt carbonyl compounds.[28, 29]

6.3. Experiments

Thin film deposition was carried out in a cold-wall reaction chamber system where the reactor chamber was connected through a load-lock to an ultra-high vacuum analysis chamber equipped with Auger electron spectroscopy (AES). The reactor system has been described in detail previously.[30] For studies described here, a quadrupole mass spectrometry (QMS) sampling

system was implemented to analyze the reaction by-products exhausted from the reactor chamber, using a 100 amu Leybold Inficon Transpector™ (model : TC100). The sampling manifold and pumping system for the QMS was designed to extract product gases from a region close to the deposition zone in order to reduce sensor response time, while maintaining the pressure in the low 10^{-5} Torr range in the QMS by differential pumping. In this system, the sample temperature is controlled using a resistive block heater, and gas flows into the top of the reactor and down over the sample stage. The sample temperature can be routinely controlled to within ± 5°C.

Chemically-formed SiO_2 on silicon, and hydrogen-terminated silicon (Si-H) were used as substrates for the experiments. For both substrates, silicon surfaces were oxidized by wet chemical treatment (BakerClean® JTB-100), followed by buffered HF acid dip, deionized water rinse, and N_2 dry. For the Si-H surface, after the chemical oxidation step, the silicon was dipped into a 1% HF acid for 30 s, followed by deionized water flush and N_2 flow dry. For the chemical oxide surface, the substrates were further treated with SC1 solution for 10 minutes, resulting in ~5-10Å thick chemical oxide**.** The AES spectra of both starting substrate surfaces, shown in Figure 6.1, show evidence for adventitious carbon contamination, and some oxidation of the HF-last silicon substrate.

The $Co_2(CO)_8$ or $Co(C_5H_5)(CO)_2$ precursors were fed from a stainless steel vessel at 25°C using a controlled flow of Ar carrier gas using an ALD-type flow sequence. Hydrogen was used as the reactant gas, and Ar was used as the purge gas between precursor and reactant doses. The flow rates of Ar and H_2 were fixed at 10 standard cubic centimeters per minute. For the deposition process, the substrates were transferred into the reactor then heated to the set-point temperature for 30 minutes to reach thermal equilibrium. The pressure was stabilized by Ar

carrier gas flow, then the binary cycles of precursor exposure and reactant flow were initiated. Throughout the cycling process, the pressure was typically maintained at 100 mTorr by a throttle valve in the reactor exhaust line. The precursor exposure time in each ALD cycle was fixed between ~3 and 20 seconds, and the reactant and purge times were generally fixed at 10 and 20 s, respectively. After deposition, films thicker than ~200Å were measured using a Tencor Alpha-Step 500 surface profilometer.

6.4. Results and Discussion

The results of thickness measurements for films deposited on silicon using $Co_2(CO)_8$ precursor and H_2 reactant at temperatures between 100 and 130°C for various numbers of deposition cycles are shown in Figure 6.2(a). The exposure times for the $Co_2(CO)_8$, Ar, H_2, and Ar deposition sequence were 3, 20, 10, and 20s respectively. Films grew on both Si-H and SiO_2 substrates without incubation time in this temperature region. Using these fixed cycle times, growth thickness per cycle was determined as a function of substrate temperature between 60 and 130°C, and results are shown in Figure 6.2(b). The data indicate that the growth per cycle is relatively constant between 80 and 110°C, then increases at higher temperatures, suggesting an ALD process window in the 80-110°C range. While previous reports of CVD using this precursor suggest growth proceeds at temperatures less than 100°C,[31, 32] thermal ALD in this range has not previously been investigated, and we hypothesized that some self-limiting surface adsorption for this precursor may be possible near the decomposition temperature, enabling low temperature thermal ALD to proceed. However, results in Figure 6.2(c) show that at fixed temperature in the 60-100°C range, the growth thickness per cycle increases linearly with the

precursor exposure time, consistent with non-self-limiting CVD behavior. The data point at 30°C was estimated from Auger Electron Spectroscopy results discussed below, indicating near zero growth at this temperature using this precursor. The films deposited between 60 and 130°C generally appeared shiny and smooth by visual inspection. After extended air exposure, AES data showed surface oxidation, and the films remained shiny and smooth. The root mean square roughness obtained from scanning force microscopy of a typical 500 Å thick film deposited at 100°C was 5.2 Å.

To further investigate the low temperature deposition reaction mechanism, the reaction by-products generated during the film growth cycles were monitored by differentially pumped quadrupole mass spectrometry. The two main reaction by-products from the film deposition using $Co_2(CO)_8$ were CO (m/z = 28) and H_2O (m/z = 18), with some contribution from CH_4 (m/z = 16) and C_2H_6 (m/z = 30). Figure 6.3 shows typical QMS signals from the reaction by-products CO, H_2O, CH_4, and C_2H_6 obtained during a complete growth cycle at 100°C on logarithmic and normalized linear scales. The QMS electronic system response time is approximately 1 second, resulting in some signal offset on the time axis. During the precursor and H_2 exposure steps, the Ar signal intensity is observed to decrease. This occurs because the Ar flow rate is fixed, but the pressure in the reactor is also held constant, resulting in a decrease in Ar partial pressure during reactant introduction steps. During the $Co_2(CO)_8$ exposure step, signals related to CO, CH_4, and C_2H_6 were detected, but the intensity of the hydrocarbons are more than a factor of 10 weaker than that of CO. Dissociation of CO_2 in the mass spectrometer is expected to produce signals at m/z of 44 and 28 with an intensity ratio of ~ 0.1:1. The typical signal intensities at m/z of 44 and 28 are in a ratio of 1:10, consistent with direct pyrolysis of $Co_2(CO)_8$ producing CO on the

heated substrate surface.[28] During the H_2 exposure step, H_2O and a small amount of CH_4 were detected. The appearance of these products can be ascribed to the catalytic cleaving of CO on cobalt producing hydrocarbons and water by Fisher-Tropsch hydrogenation. The hydrocarbons produced during the $Co_2(CO)_8$ exposure are likely due to reaction of CO with CH_x or H-Co species remaining on the growth surface after the previous H_2 exposure step. The data shown in Figure 6.4 was collected soon after growth initiation during film nucleation (cycle number 4). It is interesting to note that similar data collected in cycle ~20 showed significantly less hydrocarbon and water production, suggesting that the Co surface became less catalytically active as it coalesced into thin film form.

If the precursor adsorption is self-limiting, one would expect the CO signal in the QMS to saturate then begin to decrease as exposure proceeds. The data in Figure 6.3 shows that at 100°C and 3 seconds exposure, the CO signal did not saturate but increased continuously during the precursor exposure time. Figure 6.4(a) shows the CO signal intensity at various precursor exposure times at 100°C, and Figure 6.4(b) shows the CO intensity as a function of temperature with 20 seconds exposure. Results show that the CO intensity continued to increase with longer exposure times and at higher temperatures, consistent with continuous CVD growth over the temperature range studied as described above. Since the growth at 30°C is nearly negligible, the CO signal observed during the precursor dose step at 30°C is ascribed to direct precursor dissociation in the mass spectrometer ionization zone.

From the QMS analysis, the low temperature film deposition involves the following sequential steps:

$$Co_2(CO)_8\ pulse:\ Co_2(CO)_8 + Co(CH_x)^* \rightarrow Co(CO)_y^* + CO + CH_4 + C_2H_6 \quad (1)$$

$$H_2\ pulse:\ H_2 + Co(CO)_y^* \rightarrow Co(CH_x)^* + H_2O + CH_4 \quad (2)$$

where the asterisks refer to surface-adsorbed species, and the stoichiometric coefficients are omitted for clarity. The main reaction by-products are CO for the precursor pulse and H_2O for the H_2 pulse, with only a small amount of hydrocarbons produced. While many ALD precursors show a transition from ALD to CVD as the substrate temperature is increased, the lack of a stable thermal ALD window with $Co_2(CO)_8$ is likely due to the fact that the metal center is not formally charged, so that precursor adsorption can readily proceed without the need for exposure to a reducing agent.

Auger electron spectroscopy analysis was used to characterize the film growth as a function of deposition temperature, and the resulting spectra are shown in Figure 6.5. For each sample, data was collected following the H_2 reactant exposure step, after direct sample transfer from the reactor system to the AES chamber without air exposure. Except for the film deposited at 30°C (after 100 deposition cycles with 20 sec precursor exposure time per cycle), the data was collected after 100 ~ 300 deposition cycles using 3 seconds of precursor exposure per cycle. Some carbon and oxygen are observed on all samples, but the intensity of the C and O peaks are not strongly temperature dependent below 130°C. Based on the AES signal intensity, the film deposited at 100°C shows 65 ~ 70% cobalt, 25 ~ 30% carbon, and 5 ~ 10% oxygen. The excess carbon is due to some CO dissociation at the growth temperature, and the films are referred to here as CoC_x. Compared to growth above 60°C, longer precursor exposure times were required

to observe deposition at 30°C in the AES spectrum. For the film deposited at 30°C, the relative intensity of the Co MNN signal at ~55eV and Si LMM feature at ~92 eV indicate that the film thickness is ~8-12Å, corresponding to a nearly negligible growth rate at 30°C. Note that for the thicker Co films deposited at higher temperatures, the feature near 98 eV, similar to the Si LMM peak position, is also due to the Co MNN Auger signal.

The resistivity of the deposited CoC_x films is shown in Figure 6.6 as a function of deposition temperature. The resistivity data ranged between 13 ~ 22 μΩ·cm, with lower resistivity generally at higher temperature. These values are higher than the ~ 6 μΩ·cm bulk resistivity of cobalt, consistent with film impurities. Cobalt films deposited by Plasma ALD at 300°C showed lower impurity concentrations, and resistivity was ~10-20 μΩ·cm for conditions within the ALD process window.[14] Similar resistivity values were also reported for Plasma ALD Co from $Co(C_5H_5)_2$ at 300°C,[14] as well as 11 μΩ·cm of CVD Co from $Co_2(CO)_8$ at 200°C,[10] and 15 μΩ·cm of CVD Co from cobalt nitrosyl tricarbonyl ($Co(CO)_3(NO)$) at 390°C.[11]

To observe the effect of precursor structure on low temperature Co deposition, we explored cyclopentadienyl cobalt dicarbonyl ($Co(C_5H_5)(CO)_2$) as an alternative to $Co_2(CO)_8$. Compared to the zero-valent Co with the octacarbonyl ligands, the Co in the cyclopentadienyl-based precursor is in a +1 oxidation state, requiring a reduction step to produce elemental films. Like $Co_2(CO)_8$, this precursor has been widely studied,[5, 12] and we examine here the growth behavior at low substrate temperatures. Figure 6.7 shows the quadrupole mass spectroscopy results obtained when $Co(C_5H_5)(CO)_2$ is cycled with hydrogen at a substrate temperature of 140°C in an ALD gas exposure sequence. In this case, the signal at m/z = 39 was monitored to detect the presence of gas-phase cyclopentadienyl through its $C_3H_3^+$ dissociative ionization

product.[33] As with the $Co_2(CO)_8$ precursor, the mass spectra show that for $Co(C_5H_5)(CO)_2$ decomposition, CO was the primary gas-phase product during the precursor pulse, and H_2O was produced during the H_2 reactant dose. Methane is also produced, primarily during the precursor exposure period. No signal related to C_5H_{5+n} (n=1,3,5, · ·) (m/z = 66 ~ 70) was detected near m/z =65 (C_5H_{5+n}) or m/z=39 (C_3H_3) was observed. During the cyclopentadienyl cobalt dicarbonyl precursor exposure period, the CO signal is observed to rapidly increase, then slowly decrease (in Figure 6.8). This trend is different from that shown in Figure 6.3 for CO production during the dicobalt octacarbonyl precursor exposure step, and could suggest that the $Co(C_5H_5)(CO)_2$ is undergoing a self-limiting adsorption and decomposition step as desired for atomic layer deposition. However, after proceeding with through 300 precursor/reactant exposure cycles at 140°C, Auger analysis indicated no observable Co film. This result is ascribed to cyclopentadienyl cobalt dicarbonyl dissociation through cleavage of the CO ligand, resulting in volatile cyclopentadienyl cobalt ($Co(C_5H_5)$). Increasing the substrate temperature to 300-350°C resulted in observable Co deposition as shown in the AES data in Figure 6.9. As temperature is increased, the Si-LVV feature decreases and the Co-LMM and C-KLL features gradually increase, but at these temperatures, the H_2 exposure is not sufficient to remove the carbon and the cyclopentadienyl ligands from the surface. These results are consistent with the well known weak bonding character of carbonyl ligands with transition metals, compared to more strongly bound metal/cyclopentadienyl or metal/nitrosyl ligands.[34, 35] The weakly bound carbonyl ligands in the $Co_2(CO)_8$ precursor enable the deposition at very low temperature, however make it difficult to achieve self-limiting growth for thermal ALD. Also, while the cyclopentadienyl ligands reactive with hydrogen to form volatile hydrocarbons, they are generally stable up to near

350°C. During deposition at 350°C, the QMS results showed an increase in hydrocarbon production with no strong evidence for mass signal at m/z = 39 (C_3H_3), indicating cyclopentadienyl decomposition.

6.5. Summary and Conclusions

Thermally-driven deposition of Co thin films can proceed at 60°C using dicobalt octacarbonyl. Film deposition rate and in-situ quadrupole mass spectroscopy results demonstrate that film growth proceeds continuously at low temperature, with no indication for self-limiting precursor adsorption behavior. The lack of a viable "ALD process window" is understood in terms of the zero-valent nature of the $Co_2(CO)_8$ precursor, where no reduction step is needed to produce elemental films. Evidence for hydrocarbon and water production through catalytic cleaving of CO on cobalt was observed during the initial film growth cycles, but hydrocarbon synthesis decreased during later growth cycles, consistent with reduced catalytic activity. Experiments also investigated $Co(C_5H_5)(CO)_2$ and H_2 where the metal center is in the +1 state. Mass spectroscopy and AES results indicate that the CO ligands readily cleave from the metal center, leaving a volatile $Co(C_5H_5)$ that is reactive for deposition near ~300°C. Further experimental work is required to identify viable precursors for metal film formation by atomic layer deposition at low substrate temperatures.

Acknowledgement

This work was supported in part by the National Science Foundation under grant CTS-0626256.

6.6. References

1. Khodakov, A. Y.; Chu, W.; Fongarland, P., *Chemical Reviews* **2007,** 107, 1692-1744.

2. Lee, B. Y.; Chung, Y. K.; Jeong, N.; Lee, Y. S.; Hwang, S. H., *Journal of the American Chemical Society* **1994,** 116, 8793-8794.

3. Mao, J. M.; Sun, L. F.; Qian, L. X.; Pan, Z. W.; Chang, B. H.; Zhou, W. Y.; Wang, G.; Xie, S. S., *Applied Physics Letters* **1998,** 72, 3297-3299.

4. Diana, F. S.; Lee, S. H.; Petroff, P. M.; Kramer, E. J., *Nano Letters* **2003,** 3, 891-895.

5. Dormans, G. J. M.; Meekes, G. J. B. M.; Staring, E. G. J., *Journal of Crystal Growth* **1991,** 114, 364-372.

6. Rhee, H. S.; Ahn, B. T., *Journal of the Electrochemical Society* **1999,** 146, 2720-2724.

7. Pan, J.; Woo, C.; Ngo, M. V.; Yang, C. Y.; Besser, P.; King, P.; Bernard, J.; Adem, E.; Tracy, B.; Pellerin, J.; Xiang, Q.; Lin, M. R., *Ieee Transactions on Electron Devices* **2003,** 50, 2456-2460.

8. Lee, J.; Lee, J. G., *Journal of the Korean Physical Society* **2006,** 49, S697-S701.

9. L'Vov, B. V., *Thermochimica Acta* **2001,** 373, 97-124.

10. Gross, M. E.; Kranz, K. S.; Brasen, D.; Luftman, H., *Journal of Vacuum Science & Technology B* **1988,** 6, 1548-1552.

11. Londergan, A. R.; Nuesca, G.; Goldberg, C.; Peterson, G.; Kaloyeros, A. E.; Arkles, B.; Sullivan, J. J., *Journal of the Electrochemical Society* **2001,** 148, C21-C27.

12. Chioncel, M. F.; Haycock, P. W., *Chemical Vapor Deposition* **2005,** 11, 235-243.

13. Lim, B. S.; Rahtu, A.; Gordon, R. G., *Nature Materials* **2003,** 2, 749-754.

14. Lee, H. B. R.; Kim, H., *Electrochemical and Solid State Letters* **2006,** 9, G323-G325.

15. Kim, K.; Lee, K.; Han, S.; Jeong, W.; Jeon, H., *Journal of the Electrochemical Society* **2007,** 154, H177-H181.

16. Kim, K.; Lee, K.; Han, S.; Park, T.; Lee, Y.; Kim, J.; Yeom, S.; Jeon, H., *Japanese Journal of Applied Physics Part 2-Letters & Express Letters* **2007,** 46, L173-L176.

17. Suntola, T., *Applied Surface Science* **1996,** 101, 391-398.

18. Knez, M.; Kadri, A.; Wege, C.; Gosele, U.; Jeske, H.; Nielsch, K., *Nano Letters* **2006,** 6, 1172-1177.

19. Peng, Q.; Sun, X. Y.; Spagnola, J. C.; Hyde, G. K.; Spontak, R. J.; Parsons, G. N., *Nano Letters* **2007,** 7, 719-722.

20. Leskela, M.; Kemell, M.; Kukli, K.; Pore, V.; Santala, E.; Ritala, M.; Lu, J., *Materials Science & Engineering C-Biomimetic and Supramolecular Systems* **2007,** 27, 1504-1508.

21. Knez, M.; Niesch, K.; Niinisto, L., *Advanced Materials* **2007,** 19, 3425-3438.

22. Sang, B. S.; Konagai, M., *Japanese Journal of Applied Physics Part 2-Letters* **1996,** 35, L602-L605.

23. Kemell, M.; Pore, V.; Ritala, M.; Leskela, M.; Linden, M., *Journal of the American Chemical Society* **2005,** 127, 14178-14179.

24. Hyde, G. K.; Park, K. J.; Stewart, S. M.; Hinestroza, J. P.; Parsons, G. N., *Langmuir* **2007,** 23, 9844-9849.

25. Senkevich, J. J.; Tang, F.; Rogers, D.; Drotar, J. T.; Jezewski, C.; Lanford, W. A.; Wang, G. C.; Lu, T. M., *Chemical Vapor Deposition* **2003,** 9, 258-264.

26. Fabreguette, F. H.; Sechrist, Z. A.; Elam, J. W.; George, S. M., *Thin Solid Films* **2005,** 488, 103-110.

27. Kim, H.; Cabral, C.; Lavoie, C.; Rossnagel, S. M., *Journal of Vacuum Science & Technology B* **2002,** 20, 1321-1326.

28. Tannenbaum, R.; Bor, G., *Journal of Organometallic Chemistry* **1999,** 586, 18-22.

29. West, G. A.; Beeson, K. W., *Applied Physics Letters* **1988,** 53, 740-742.

30. Park, K. J.; Terry, D. B.; Stewart, S. M.; Parsons, G. N., *Langmuir* **2007,** 23, 6106-6112.

31. Ye, D. X.; Pimanpang, S.; Jezewski, C.; Tang, F.; Senkevich, J. J.; Wang, G. C.; Lu, T. M., *Thin Solid Films* **2005,** 485, 95-100.

32.Lee, J.; Yang, H. J.; Lee, J. H.; Kim, J. Y.; Nam, W. J.; Shin, H. J.; Ko, Y. K.; Lee, J. G.; Lee, E. G.; Kim, C. S., *Journal of the Electrochemical Society* **2006,** 153, G539-G542.

33. Opitz, J., *International Journal of Mass Spectrometry* **2003,** 225, 115-126.

34. Sztaray, B.; Szepes, L.; Baer, T., *Journal of Physical Chemistry A* **2003,** 107, 9486-9490.

35. Sztaray, B.; Baer, T., *Journal of Physical Chemistry A* **2002,** 106, 8046-8053.

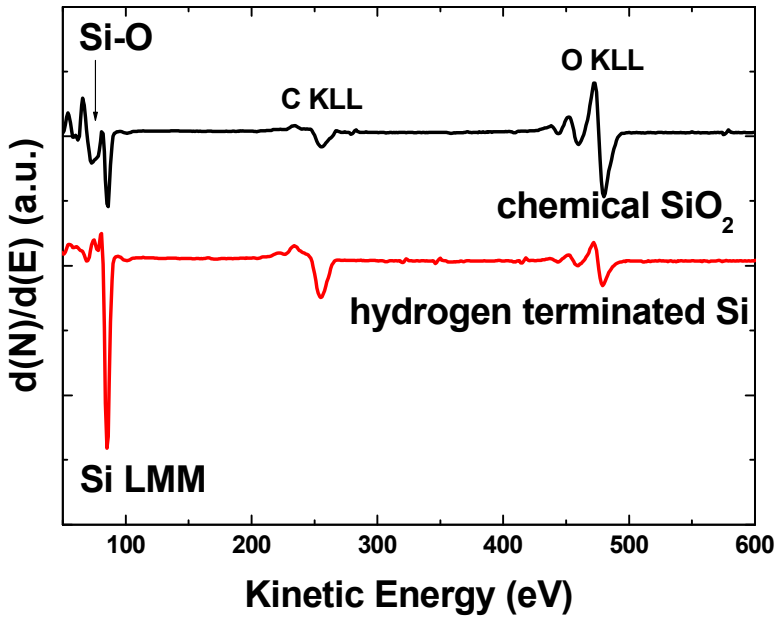

Figure 6.1. AES spectra of substrates used in film deposition studies, including H-terminated silicon (Si-H) and chemically oxidized silicon. Adventitious carbon and some oxidation of the Si-H surface are observed due to ambient exposure after surface preparation.

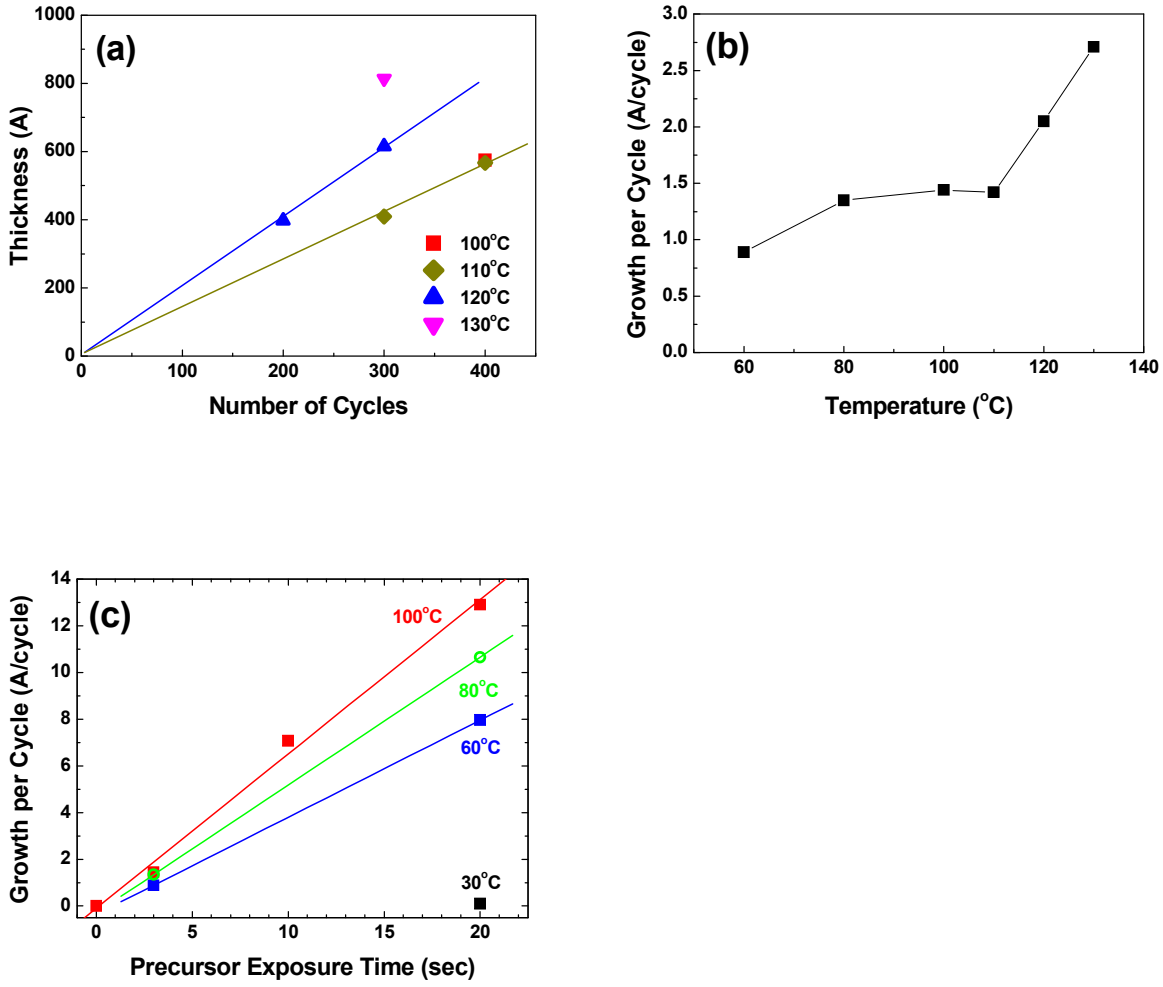

Figure 6.2. Growth thickness per deposition cycle of the cobalt films on silicon deposited using $Co_2(CO)_8$ and H_2. (a) The film thickness increases linearly with the number of precursor/reactant exposure cycles at several deposition temperatures. (b) The growth thickness obtained with 3 seconds precursor exposure per cycle is plotted at various deposition temperatures. The lines are linear fits to the data points shown. (c) The growth per cycle is observed to increase continuously with increasing $Co_2(CO)_8$ precursor exposure time. The point at 30°C was estimated from Auger electron spectroscopy results.

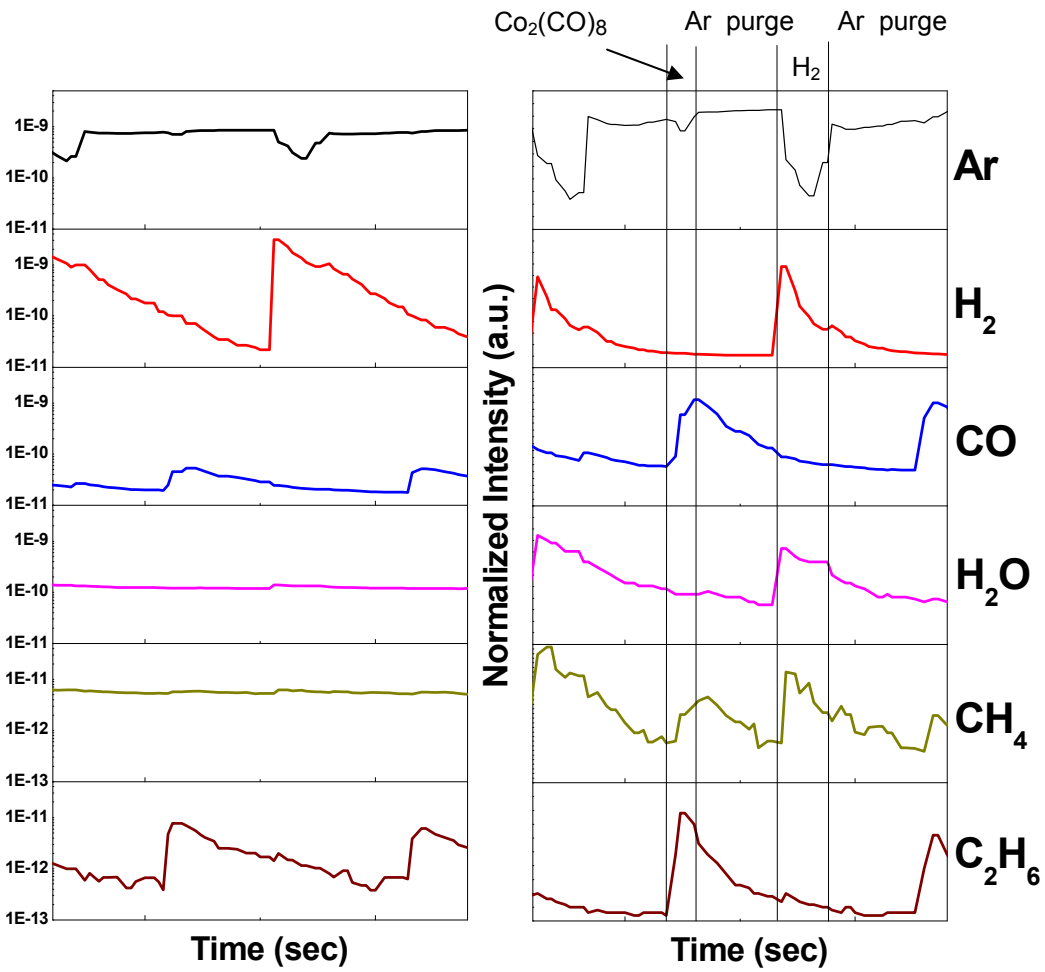

Figure 6.3. Quadrupole mass spectroscopy signals obtained during deposition using $Co_2(CO)_8$ and H_2 at 100°C with a pressure of 100 mTorr. Spectra are shown on a logarithmic scale (left) and a normalized linear scale (right). Signals are shown for Ar (40 amu), H_2 (2 amu), CO (28 amu), H_2O (18 amu), CH_4 (16 amu) and C_2H_6 (30 amu). The approximate times for the gas flow switching are indicated on the linear plot. Some delay in the QMS signal relative to the gas switching is observed due to gas residence time effects.

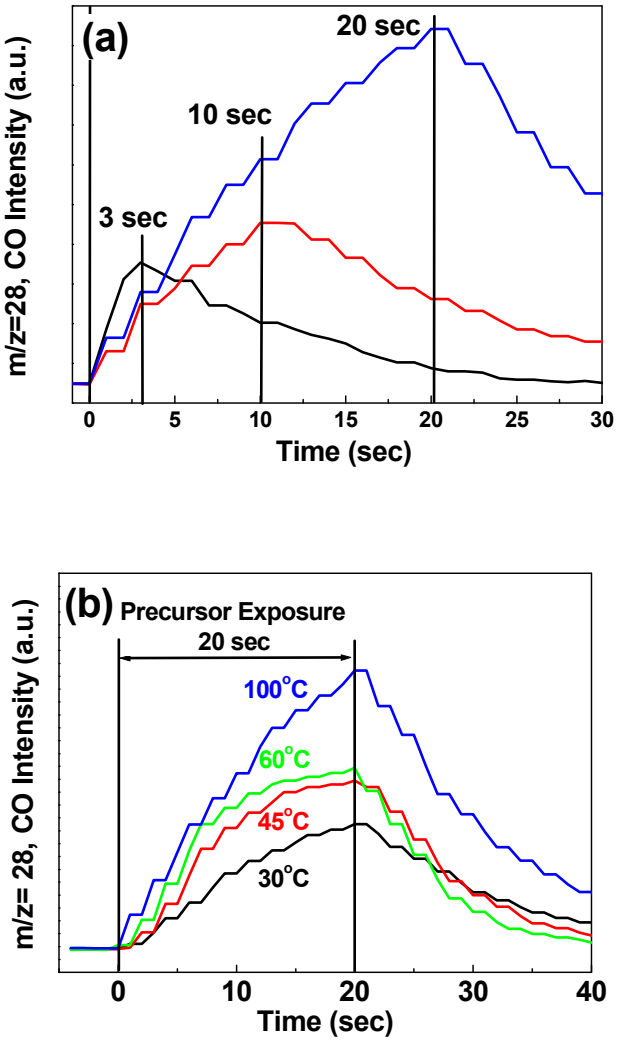

Figure 6.4. QMS signal obtained from CO (m/z = 28) during cobalt deposition using $Co_2(CO)_8$ precursor using: (a) different precursor exposure times at 100°C with a pressure of 100 mTorr; and (b) different deposition temperatures at 20 s precursor exposure time with a pressure of 500 mTorr. The signal at 30°C is ascribed to electron impact dissociation of the precursor in the mass spectrometer. Under all conditions studied, the CO mass signal increased with increasing exposure time.

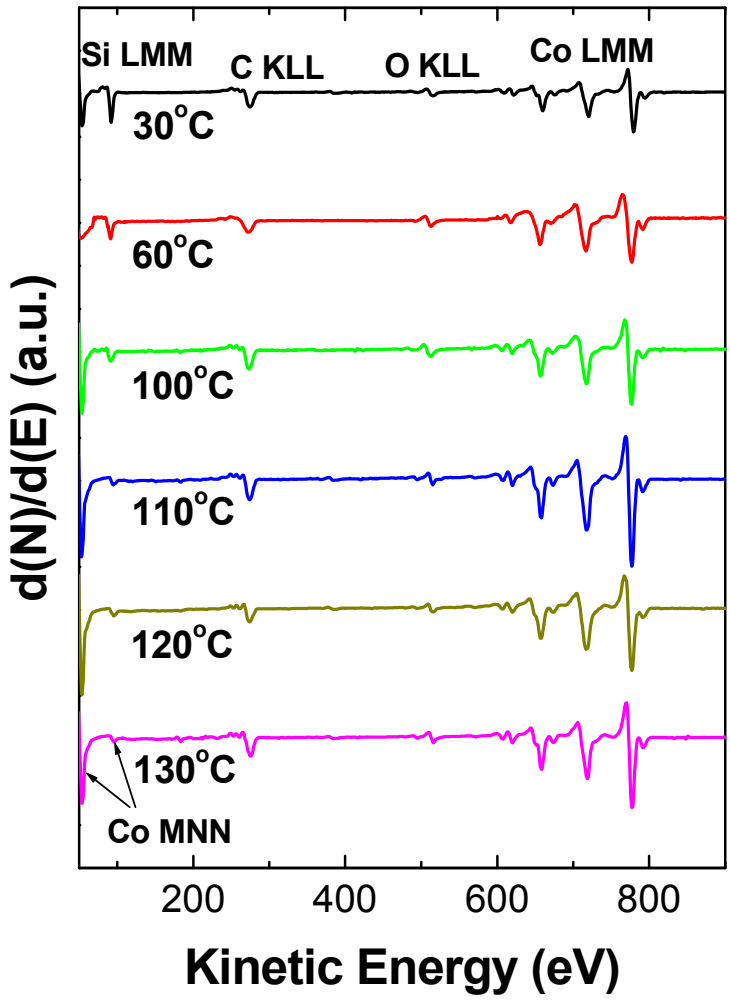

Figure 6.5. AES spectra of deposited film using $Co_2(CO)_8$ precursor at various deposition temperatures on Si-H substrates. The AES analysis was performed by direct sample transfer the high vacuum chamber without ambient exposure. The data was collected after 100 - 300 deposition cycles using 3 s of precursor exposure per cycle, except for the sample deposited at 30°C. For the 30°C sample, the precursor exposure time was 20 seconds per cycle, and data was collected after 100 deposition cycles. The AES results indicate that films deposited at 100-130°C contain 25 ~ 30% carbon, and 5 ~ 10% oxygen.

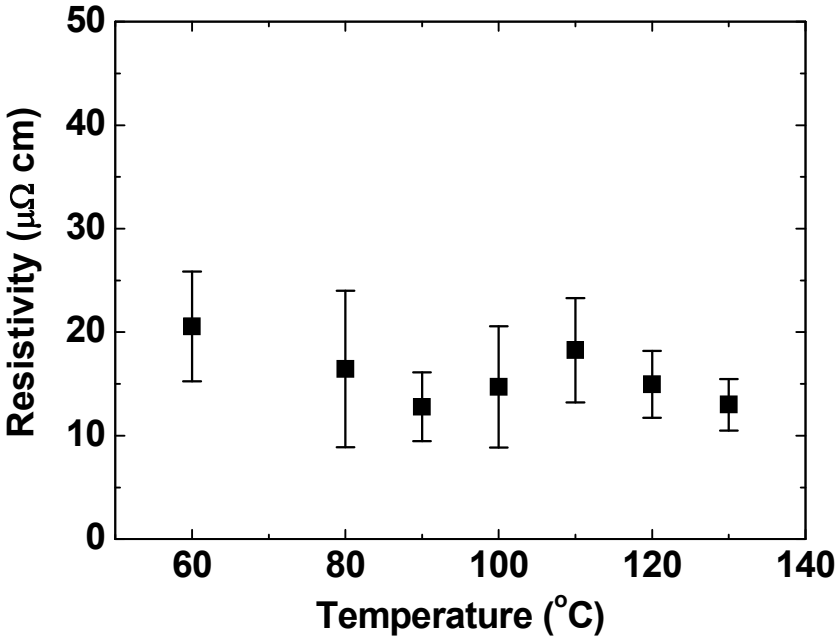

Figure 6.6. Resistivity of deposited films versus deposition temperature using $Co_2(CO)_8$ precursor. The error bars represent one standard deviation from a set of 5 measurements on each sample.

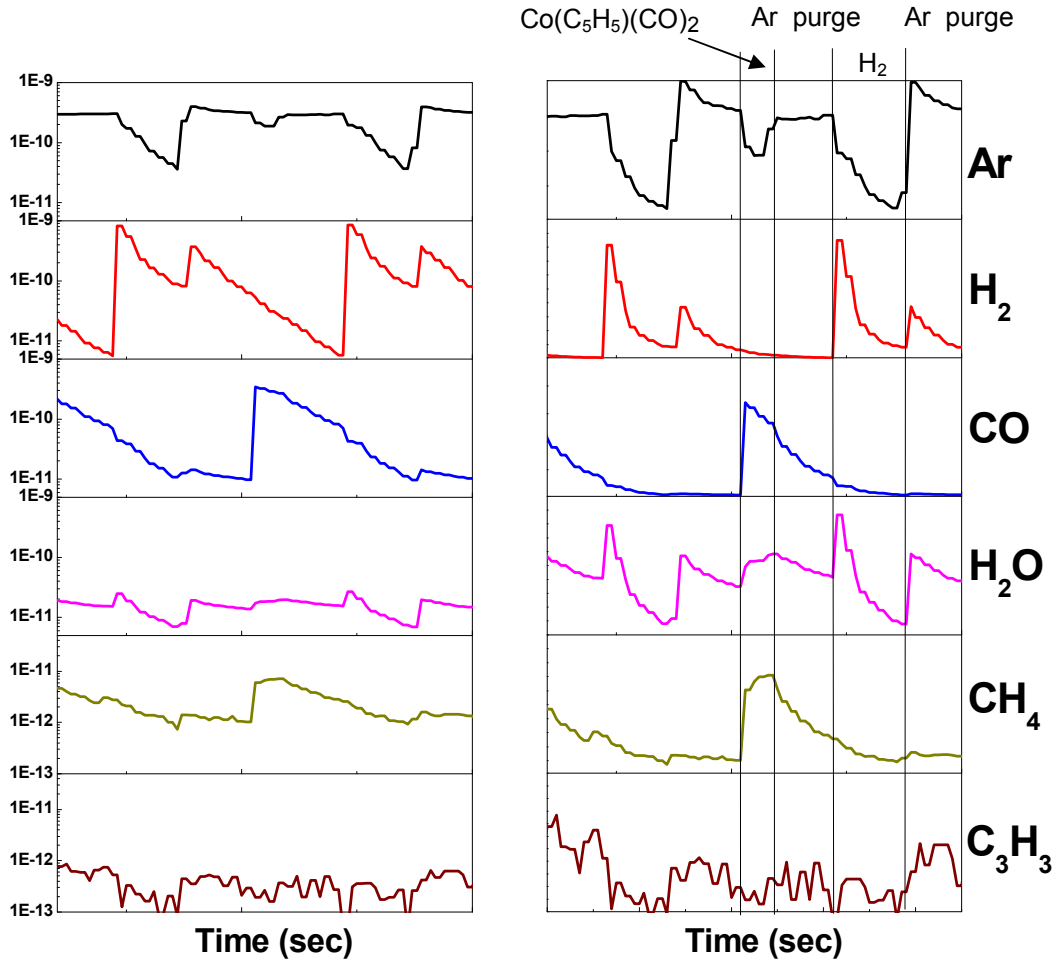

Figure 6.7. Quadrupole mass spectroscopy signals obtained during deposition using $Co(C_5H_5)(CO)_2$ and H_2 at 140°C with a pressure of 100 mTorr. Spectra are shown on a logarithmic scale (left) and a normalized linear scale (right). Signals are shown for Ar (40 amu), H_2 (2 amu), CO (28 amu), H_2O (18 amu), CH_4 (16 amu) and C_3H_3 (39 amu).

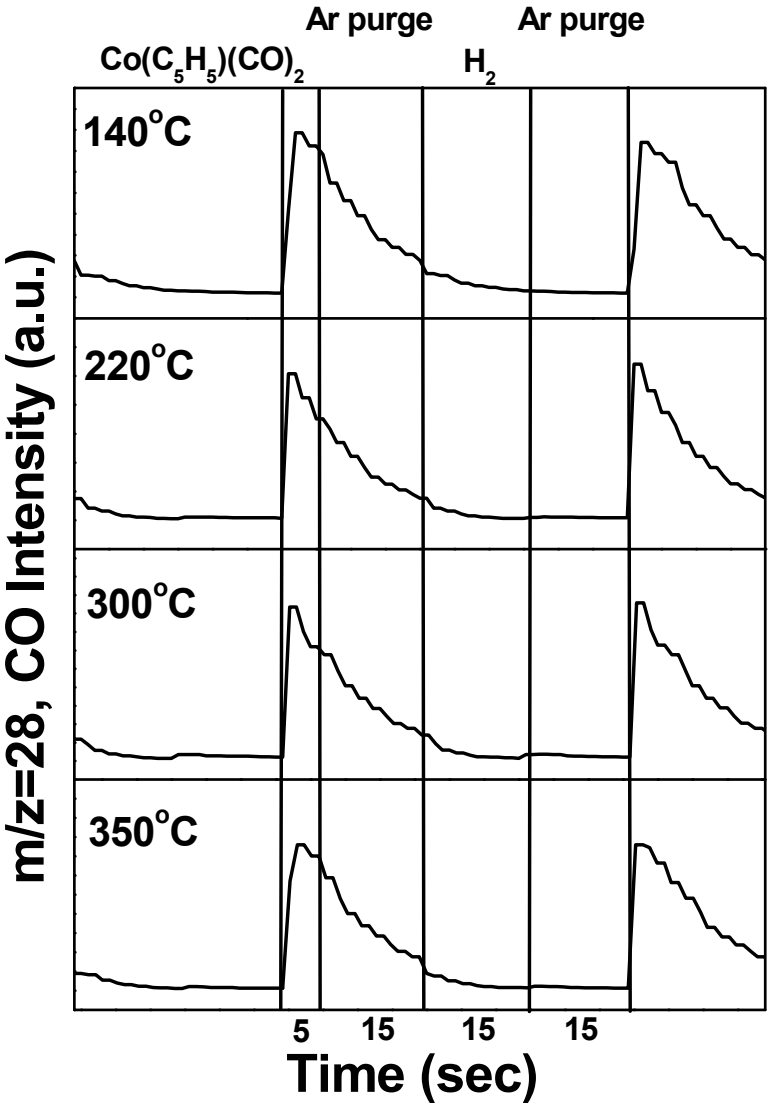

Figure 6.8. QMS signal obtained from CO (m/z = 28) during cobalt deposition using $Co(C_5H_5)(CO)_2$ precursor with different deposition temperatures with a pressure of 100 mTorr. The exposure times for the $Co(C_5H_5)(CO)_2$, Ar, H_2, and Ar deposition sequence were 5, 15, 15, and 15s respectively.

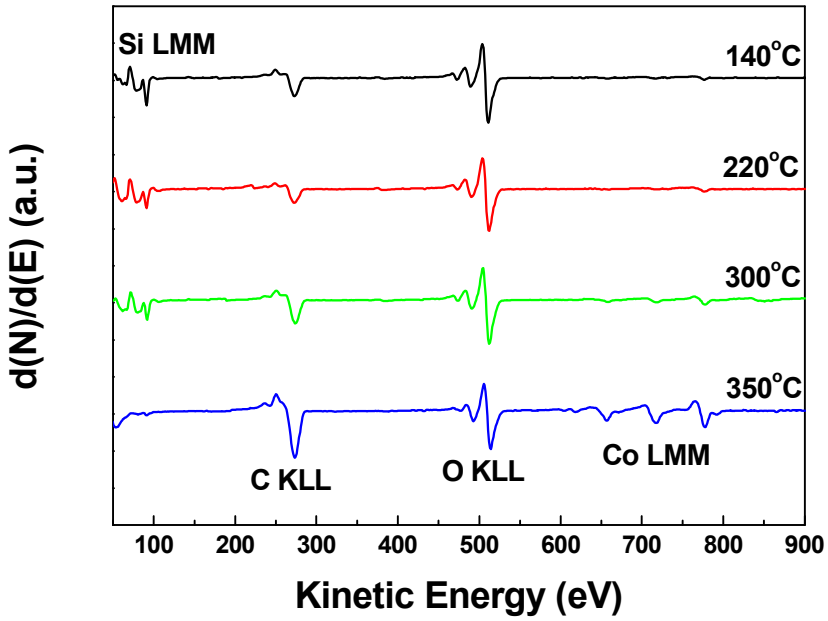

Figure 6.9. AES spectra of Co film using $Co(C_5H_5)(CO)_2$ precursor with respect to deposition temperature on SiO_2 surface : Data was collected after 300 cycles using 5 s of precursor exposure per cycle. The Co LMM AES signal is observed at deposition temperatures of 300 and 350°C.